# Calibration of Aperture Arrays using Self-Holography

by

Cornelis Rossouw Wilke

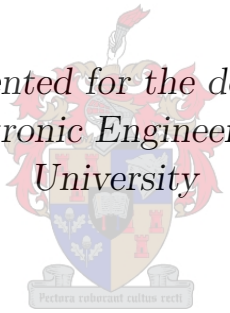


*Dissertation presented for the degree of Doctor of Philosophy in Electronic Engineering at Stellenbosch University*

Supervisors:

Prof. S.J. Wijnholds  Dr J. Gilmore

December 2021

# Declaration

By submitting this thesis electronically, I declare that the entirety of the work contained therein is my own, original work, that I am the sole author thereof (save to the extent explicitly otherwise stated), that reproduction and publication thereof by Stellenbosch University will not infringe any third party rights and that I have not previously in its entirety or in part submitted it for obtaining any qualification.

Signature: .....
C.R. Wilke

Date: December 2021

# Abstract

The calibration methods that are commonly applied to aperture array instruments typically rely on knowledge of the array covariance matrix. This implies an associated compute load and data volume that scale with the square of the number of receive paths, $P$, in the array. This trend might become prohibitive for large arrays or arrays with limited computing resources. Alternative methods are being developed to address this issue.

One of these methods is self-holography (SH) which derives the complex-valued receive path gains from the correlations between the individual receive path signals, and a reference signal obtained with the array itself. As this only involves $P$ correlations, the compute load and data volume scale only linearly with $P$. In its original formulation, the receive path gains are derived directly from the crosscorrelations. Since the reference signal is obtained by the array itself, the crosscorrelations contain an unwanted correlation in the thermal noise of the array. This leads to a bias in the amplitude of the gain estimates while the corresponding phase estimates converge to their true values after sufficient solving iterations. In this dissertation, it was discovered that this bias can be remedied by accurately compensating the thermal noise in the measured crosscorrelations. However, this is not a trivial process and in reality, will be challenging to implement accurately. These limitations lead to a revised formulation in which the receive path gains and noise powers are estimated simultaneously. But thermal noise is not the only factor that dictates the accuracy of SH. Up to this point, it was assumed that the calibration scenario resembles the situation with a single probe in an anechoic chamber, i.e, no other signals other than the reference signal is present. In reality, this assumption will be violated due to the unavoidable presence of interference and the accuracy of the gain estimates will be affected to an extent that is dependent on the actual isolation of the reference signal.

In this dissertation, a detailed analysis was performed on the mathematics underlying the second formulation of SH and an analytical expression for the signal-to-interference ratio (SIR) of the reference signal was extracted. This was followed by a detailed simulation study in which the accuracy of the gain estimates was determined as a function of the SIR for a given calibration scenario and array configuration. As expected, the accuracy of the gain estimates was found to be inversely proportional to the SIR. It was also determined that

the results are independent of the array configuration which confirms that the SIR expression is universal and can be used, together with the simulation results, to calculate the expected accuracy of the gain estimates given any analytical calibration scenario. An analysis was also done on the effectiveness of using null placement to minimize the interference received by the array. It was determined that nulling can be very effective in scenarios where the SIR is low due to one or two strong interferers. This is an especially promising result for the application of SH in commercial applications where small (lower directivity) arrays are typically used in the presence of strong interferers.

The simulation study was followed by a first-ever practical application of SH calibration on data that was recorded by a Low-Frequency Array (LOFAR) low-band antenna (LBA) and high-band antenna (HBA) station. A visual inspection of the before and after imaged data proved that SH calibration was applied successfully. By estimating the level of interference in the recorded data, it was estimated that the SIR for the LBA data had a maximum of around 15 dB when using Cassiopeia A as the calibration source which corresponds to an RMS relative gain error of around 0.04 according to the results from the simulation study. Similarly, when using Cygnus A as a calibration source for the HBA recorded data, a maximum SIR of around 19 dB was calculated which corresponds to an RMS relative gain error of around 0.02. The gain estimates obtained with SH corresponded closely with those obtained with the standard LOFAR calibration pipeline, which further confirmed its successful application.

In the final part of this dissertation, a study was performed to determine the suitability of applying SH to a Mid-Frequency Aperture Array (MFAA) station of the Square Kilometre Array (SKA). A Mid-Frequency Aperture Array Transient and Intensity-Mapping System (MANTIS) station was used as a reference and an appropriate sky model was simulated by carefully combining multiple resources. The SIR was calculated for various potential calibration sources at 10-minute intervals over 24 hours and the results showed that SIR's well above 20 dB can be expected for most of a sidereal day. This confirms that SH will be perfectly suitable to calibrate an MFAA station which is a promising result for the future of the SKA.

# Opsomming

Die kalibrasiemetodes wat gewoonlik op apertuur samestelling instrumente toegepas word, berus gewoonlik op kennis van die samestelling kovariansiematriks. Dit impliseer 'n gepaardgaande rekenlading en datavolume wat skaal met die kwadraat van die aantal ontvangspaaie, $P$, in die samestelling. Hierdie tendens kan onbetaalbaar word vir groot samestellings of samestellings met beperkte rekenaarhulpbronne. Alternatiewe metodes word ontwikkel om hierdie kwessie aan te spreek.

Een van hierdie metodes is self-holografie (SH), wat die komplekswaardige ontvangspadaanwinste verkry uit die korrelasies tussen die individuele ontvangspadseine, en 'n verwysingssein wat met die samestelling self verkry word. Aangesien dit slegs $P$ korrelasies behels, skaal die rekenbelasting en datavolume slegs liner met $P$. In sy oorspronklike formulering word die ontvangspadaanwinste direk verkry uit die kruiskorrelasies. Aangesien die verwysingsein deur die samestelling self verkry word, bevat die kruiskorrelasies 'n ongewenste korrelasie in die termiese geraas van die samestelling. Dit lei tot 'n vooroordeel in die amplitude van die aanwinsberamings, terwyl die ooreenstemmende faseberamings na genoeg oplossings iterasies na hul werklike waardes konvergeer. In hierdie proefskrif is dit ontdek dat hierdie vooroordeel reggestel kan word deur die termiese geraas in die gemete kruiskorrelasies akkuraat te vergoed. Dit is egter nie 'n onbenullige proses nie en sal in werklikheid moeilik wees om akkuraat te implementeer. Hierdie beperkings het gelei tot 'n hersiende formulering waarin die ontvangspadaanwinste en geraasdrywings gelyktydig geskat word. Maar, termiese geraas is nie die enigste faktor wat die akkuraatheid van SH bepaal nie. Tot hiertoe is dit aanvaar dat die kalibrasiescenario die situasie met 'n enkele probe in 'n anekoese kamer voorstel, d.w.s. dat daar geen ander seine as die verwysings sein is nie. In werklikheid sal hierdie aanname geskend word as gevolg van die onvermydelike teenwoordigheid van steuring, en die akkuraatheid van die aanwinsberamings sal benvloed word in 'n mate wat afhang van die werklike isolasie van die verwysingssein.

In hierdie proefskrif is 'n gedetailleerde ontleding van die wiskunde onderliggend aan die tweede formulering van SH uitgevoer, en 'n analitiese uitdrukking vir die sein-tot-interferensieverhouding (SIV) van die verwysingssein is onttrek. Dit is gevolg deur 'n gedetailleerde simulasie-studie waarin die akkuraatheid van die winsberamings bepaal is as 'n funksie van die SIV vir

'n gegewe kalibrasiescenario en samestellingkonfigurasie. Soos verwag, is dit gevind dat die akkuraatheid van die aanwinsberamings omgekeerd eweredig is aan die SIV. Daar is ook vasgestel dat die resultate onafhanklik is van die samestellingkonfigurasie wat bevestig dat die SIV-uitdrukking universeel is en tesame met die simulasie-resultate gebruik kan word om die verwagte akkuraatheid van die winsberamings te bereken gegewe enige analitiese kalibrasiescenario. 'n Analise is ook gedoen oor die effektiwiteit van die gebruik van nulplasing om die steuring wat die samestelling ontvang, te verminder. Daar is vasgestel dat nulplasing baie effektief kan wees in scenario's waar die SIV laag is as gevolg van een of twee sterk steuraars. Dit is 'n baie belowende resultaat vir die toepassing van SH in kommersile toepassings, waar klein samestellings (laer direktiwiteit) gewoonlik gebruik word in die teenwoordigheid van sterk steuraars.

Die simulasie-studie is gevolg deur 'n eerste-ooit praktiese toepassing van SH-kalibrasie op data wat deur 'n "Low-Frequency Array (LOFAR) low-band antenna (LBA)" en "high-band antenna (HBA)" -stasie opgeneem is. 'n Visuele inspeksie van die voor- en na- gebeelde data bewys dat SH-kalibrasie suksesvol toegepas was. Deur 'n skatting van die vlak van interferensie in die aangetekende data te maak, is dit beraam dat die SIV vir die LBA-data 'n maksimum van ongeveer 15 dB gehad het wanneer Cassiopeia A as die kalibrasiebron gebruik is, wat ooreenstem met 'n RMS-aanwinsfout van ongeveer 0,04 volgens die resultate uit die simulasie-studie. Net so is 'n maksimum SIV van ongeveer 19 dB bereken wanneer Cygnus A as kalibrasiebron vir die HBA-aangetekende data gebruik word, wat ooreenstem met 'n RMS-aanwinsfout van ongeveer 0,02. Die aanwinsberamings wat met SH verkry is, stem goed ooreen met di wat verkry is met die standaard LOFAR-kalibrasiepyplyn, wat die suksesvolle toepassing daarvan verder bevestig.

In die laaste gedeelte van hierdie proefskrif is 'n studie uitgevoer om die geskiktheid van die toepassing van SH op 'n "Mid-Frequency Aperture Array (MFAA)" -stasie van die "Square Kilometer Array (SKA)" te bepaal. 'n "Mid-Frequency Aperture Array Transient and Intensity-Mapping System (MANTIS)" -stasie is as verwysing gebruik en 'n toepaslike lugmodel is gesimuleer deur die versigtige samestelling van menigte hulpbronne. Die SIV is bereken vir verskillende potensile kalibrasiebronne vir tussenpouses van tien minute oor 24 uur en die resultate het getoon dat SIV's bo 20 dB die grootste deel verwag kan word. Dit bevestig dat SH perfek geskik sal wees om 'n MFAA-stasie te kalibreer, wat 'n belowende resultaat vir die toekoms van die SKA is.

# Acknowledgements


- Dr Jacki Gilmore, who supervised my undergraduate final year project, my Master's and finally a PhD. I am extremely grateful for the opportunities that you have provided me and your excellent guidance throughout all of it.
- Prof. Stefan J. Wijnholds, for your excellent guidance and (supernatural) patience. I am very fortunate to have had a co-supervisor of your calibre for this project.
- ASTRON, for hosting me on multiple occasions over the last 5 years.
- My ander helfte, Carmen, vir al jou liefde en ondersteuning.

# Contents

# List of Figures

# Nomenclature

### Constants

c = 299792458 m/s

$\pi$ = 3.14159265359

$e$ = 2.71828182845

### Acronyms

ADC Analogue to Digital Converter

ALMA Atacama Large Millimetre Array

ASKAP Australian Square Kilometre Array Pathfinder

CAD Computer Aided Design

DDE Direction-dependent effects

DIE Direction-independent effects

EEP Embedded element pattern

EMBRACE Electronic Multi-Beam Radio Astronomy ConcEpt

EPICal E-field Parallel Imaging Calibration

FoV Field of view

GPS Global Positioning System

GP Galactic plane

HBA High-Band Antenna

HERA Hydrogen Epoch of Reionization Array

HM Haslam map

IM Intensity map

LBA Low-Band Antenna

LFAA Low-Frequency Aperture Array

LNA Low-noise amplifier

LOFAR Low-Frequency Array

MANTIS Mid-Frequency Aperture Array Transient and Intensity-Mapping System

MeerKAT Meer-Karoo Array Telescope

MFAA Mid-Frequency Aperture Array
MWA Murchison Widefield Array
NVSS NRAO VLA Sky Survey
PAASAR Phased Array Antenna for Search and Rescue
PRBS Pseudorandom binary sequence
PSC Point source catalogue
RFI Radio frequency interference
RIME Radio interferometry measurement equation
SEFD System equivalent flux density
SH Self-holograhy
SIR Signal-to-interference ratio
SKA Square Kilometre Array
SNR Signal-to-noise ratio
StEFCal Statistically and Efficient Fast Calibration
SUMSS Sydney University Molonglo Sky Survey
VLA Very Large Array

# Chapter 1

# Introduction

## 1.1 The Square Kilometre Array

The next step towards a full understanding of the Universe requires radio telescopes that are significantly more powerful compared to existing telescopes. Over the last three decades, an international community has been working hard towards a telescope design that will have a collecting area of one million square meters. This concept is called the Square Kilometre Array (SKA).

The SKA will observe at frequencies between 50 MHz and 25 GHz to enable a wide range of science cases. Besides benefiting from the sensitivity of the SKA, some of these science cases additionally require a survey speed that is significantly higher than what existing instruments can provide [1]–[3].

Designing an instrument that satisfies these two main requirements is a monumental challenge. Needless to say, an instrument with a 1 $km^2$ collecting area will require the construction of thousands of antennas. The ultra-wide bandwidth will also require the combination of various antenna and receiver designs. Some progress has already been made in this regard - it is already realized that aperture arrays will work best for frequencies below around 1.5 GHz and arrays of reflector antennas will be best suited for the frequencies above. Since most of the design concepts of the SKA have never been built at this scale, a phased construction approach has been devised to effectively deal with potential setbacks. Phase 1 will see the construction of around 10 % of the total collecting area for the low- and mid-frequency band and phase 2 will see the completion of the full array. To date, 4 precursor facilities have been built. These are the MeerKAT [4], the Hydrogen Epoch of Reionization Array (HERA) [5], the Murchison Widefield Array (MWA) [6], [7] and the Australian SKA Pathfinder (ASKAP) [8].

Two aperture arrays will be implemented at the lower frequencies (below 1.5 GHz). These are the Low-Frequency Aperture Array (LFAA) for frequencies between 50 and 450 MHz and the Mid-Frequency Aperture Array (MFAA) for frequencies between 450 MHz and 1.5 GHz [2]. The design of the LFAA

has so far been substantially more clear-cut than the design of the MFAA. As a result, the MFAA consortium was formed and tasked with the characterisation of aperture array systems at these frequencies. So far, the consortium has conceived several potential technologies for the MFAA [9]–[12].

The design challenges of these AA instruments are not limited to hardware. The vast number of antennas impose an equally large challenge in the software design of these instruments. Existing algorithms will have to be rethought and novel solutions will be required to deal with the high data rates that these instruments will produce.

## 1.2 Calibration

Calibration of the gain and phase variations introduced by the atmosphere and the receiver system is crucial to ensure that meaningful scientific analysis can be performed on the signals received by the instrument [13]. The calibration of aperture array radio telescopes poses several unique challenges in comparison with reflector-based systems. At the sensitivity levels required of modern radio telescopes, a large number of antennas are typically required to sample the corresponding aperture area. Existing examples of these type of Instruments are the Low-Frequency Array (LOFAR)[14]–[16], Murchison Wide-Field Array (MWA) [6] and the Electronic Multi-Beam Radio Astronomy ConCEpt (EMBRACE)[1], [17], [18] which all have around three orders of magnitude more antennas than the Westerbork Synthesis Radio Telescope [19] and the Very Large Array (VLA)[20].

For aperture arrays, a hierarchical design is usually implemented to lower the data volume generated by the array. Figure 1.1 illustrates a hierarchical design in which it can be seen that each subarray, which is referred to as a *station*, is subdivided into more subarrays, which are called *tiles*. Gain and phase variations are introduced in the signal paths (indicated by the blue arrows in Figure 1.1) by the following:

- *Receiver*. Cosmic signals are typically very weak and therefore require highly sensitive receivers to be detected. The sensitivity of the receiver is inversely dependent on the level of thermal noise present in the receiver. As such, the signals are amplified with low-noise amplifiers. Changes in ambient temperature can therefore alter the response of the receiver. The signals are also transported over long distances to a processing facility where they are digitised. This transportation introduces amplitude and phase variations that are dependent on both the distance travelled and the temperature of the medium used. These complex-valued offsets are commonly referred to as the *receive path* gain of each receiver. The receive path gain is both time and frequency-dependent.

- *Instrumental response.* The direction-dependent sensitivity varies between receivers. For an array, this implies that there will be gain variations in the received signals coming from the same direction.

- *Propagation path.* Refraction and diffraction caused by ionospheric and tropospheric turbulence can have a significant impact on the propagation of radio waves. Stations placed far apart will look through different parts of the atmosphere when observing a common source. This can lead to distorted images and shifts in the apparent positions of sources.

The effects in the first point are commonly referred to as direction-independent effects (DIE's), as they are not dependent on the direction a signal is coming from. Corrections for these effects are typically applied at gain blocks 1 in Figure 1.1. Conversely, the last two points are commonly referred to as direction-dependent effects (DDE's) and corrections for it are applied at gain blocks 2 in Figure 1.1. The nature and severity of the propagation effects (as described in the third point) on the measurement made by an aperture array are dependent on the specific layout and type of receivers used by the array. This results in 4 different calibration scenarios as described in [21]. This thesis will only deal with the effects described in the first point so further discussion of the effects in the second and third point is out of scope.

Calibration entails the estimation of these parameters and subsequently correcting for it. In radio astronomy, estimation of these parameters is usually done using the well-known self-calibration (self-cal) algorithm [22]–[25]. Self-cal uses the source under observation as the calibrator for the measurement. Calibration parameters are derived by minimizing the square of the modulus of the difference between the measurement and a model of the measurement which is described by the radio interferometer measurement equation (commonly referred to as the RIME)[26]–[29]. The measurement model is usually derived using the strongest sources within the FoV of the instrument. An example of an implementation of self-cal is the Statistically Efficient and Fast Calibration (StEFCal) algorithm [30], [31] which is used in the calibration software package MEqTrees [32] and the LOFAR standard preprocessing pipeline.

This thesis focuses on the calibration of aperture array radio telescopes, but it should be noted that the problem that is being investigated is relevant in a very broad range of applications [33]–[35]. For example, in [36]–[38] self-calibration methods are presented which aim to solve the direction independent gains and antenna positions of the array.

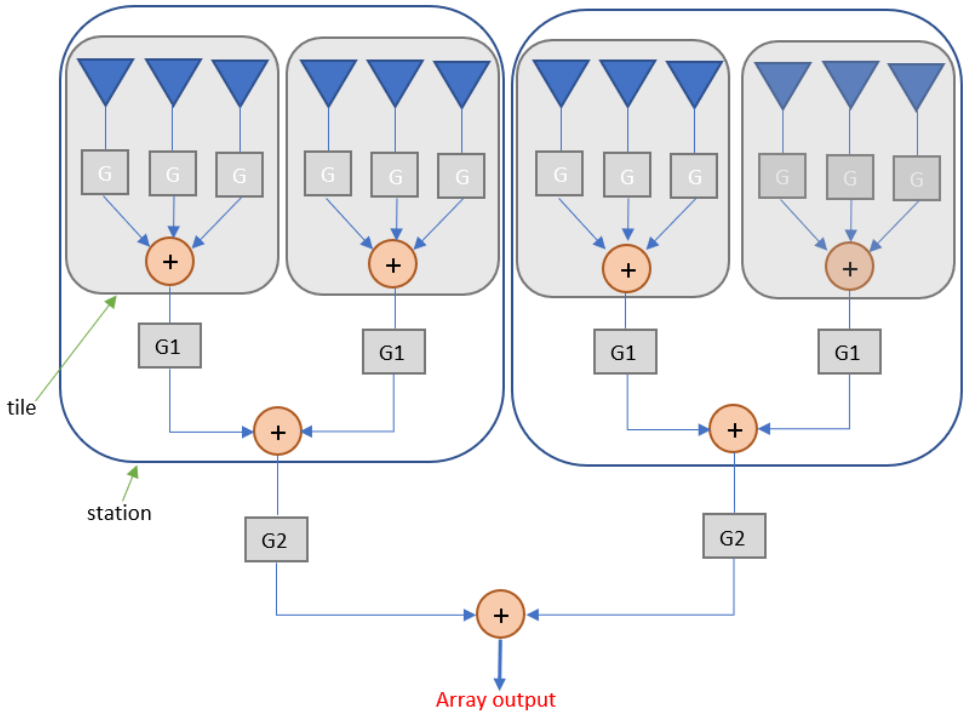


**Figure 1.1:** Diagram of an aperture array instrument showing the typical signal chain and location of gain blocks

## 1.3 Problem statement

The previous section mentioned the self-calibration algorithm which is commonly used to calibrate radio astronomy instruments. It was pointed out that the method relies on knowledge of the sky within the FoV of the telescope to construct a model of the RIME from which the unknown responses of the instrument can be derived. The RIME contains the array covariance matrix, which is a $P \times P$ matrix where $P$ is the number of receive paths of the array. This implies that the compute load and data volume required to implement self-cal, scales with the square of $P$. This may become prohibitive for large arrays or when the available computing resources are limited. The MFAA, introduced in Section 1.1, will consist of subarrays that have $10^3$ to $10^4$ receive paths each. The Phased Array Antenna for Search and Rescue [39] is a good example of a system where computing resources are limited.

To address this issue, two methods have been proposed based on the correlation of the signals from individual receive paths with the signal from a reference beam formed by the full array, namely the E-field Parallel Imaging Calibration (EPICal) algorithm [40], [41] and self-holography (SH) [42], [43]. For both methods, the processing load to acquire the measurements and the resulting data volume scale linearly with the number of elements in the array (as opposed to with the square). Unfortunately, array covariance matrices are

still used in the computation of the measurement model in EPICal while the SH method produces biased solutions that can only be remedied by careful modelling of the system noise [44].

By using a reference beam, SH aims to isolate a single signal for calibration. This simplifies the calibration procedure and resembles the situation with a single probe in an anechoic chamber measurement. However, in reality, the calibration signal is never entirely isolated due to the unavoidable presence of interference. In this thesis, the effects of this violation on the core assumption of SH, are investigated and quantified in detail. Therefore, the aim of this thesis is *"to understand in what practical scenarios the SH method is suitable for in-situ calibration of phased array systems"* and *"to what extent is self-holography applicable to LOFAR and the aperture array subsystems of the SKA"*.

## 1.4 Contributions

- In the original implementation of SH [43], the gains were derived directly from the crosscorrelations between the reference signal and the antenna signals. The reference signal is obtained using the same antennas that are under investigation, and as a result, there is an unwanted noise correlation in the crosscorrelations. This leads to a bias in the amplitudes of the gain estimates whereas the gain phase estimates converged to their true values after a number of iterations. The speed of convergence was found to be dependent on the SNR of the calibration signal. Possible performance improvements to this implementation were investigated by me in [44]. It was determined that the speed of the convergence of the gain estimates could be improved by averaging the results from the last two iterations. It was also determined that the bias in the amplitude of gain estimates could be reduced by subtracting an accurate estimate of the system noise power during iteration. During this investigation, it was discovered that the system noise is not the only contributor to the bias described above and that formulation of the method itself will cause a bias even when the system is without thermal noise.

- With the limitations of the original implementation clearly determined, a new formulation was derived by S.J. Wijnholds. In this formulation, the gains and noise powers are estimated separately by incorporating the antenna signal autocorrelations. The next unknown was the impact of interference since SH still assumes that the calibration signal is isolated. In [61], I derived an assessment criterion that relates the accuracy of the gain estimates to the level of interference. A detailed simulation analysis was performed to confirm the mathematical findings that lead to the criterion. SH calibration was then applied to real data measured with a LOFAR station. A visual inspection of the calibrated images

calculated from these measurements revealed that SH was applied successfully. To determine the accuracy of the calibration, the assessment criterion was applied by accurately estimating the level of interference in the measured data. In Chapter 4, the accuracy of the gain estimates was further assessed by comparing the SH results with those obtained from the standard LOFAR calibration pipeline.

- With the effects of interference on SH quantified in [61], I then went on to determine the possible performance improvements when using null placement as interference mitigation in [45]. The results of this study showed that null-placement can be very effective in scenarios where a single strong interferer is present. This can be especially useful in radio astronomy to null interference originating from other bright sources that are located near the calibrator. During this study, it was also determined that SH will switch to the strongest apparent source in the sky (after attenuation by the array pattern) even when the reference beam is not pointed at it.

- SH calibration was originally identified as an attractive option for calibrating large antenna arrays. With the behaviour of SH calibration established during the previous contributions, the next step was clear: to investigate the feasibility of applying SH to the MFAA. Since the MFAA is still in its conceptual phase, it was decided to base the investigation on the Mid-Frequency Aperture Array Transient and Intensity-Mapping System (MANTIS), which is the best reference to an MFAA station design to date. In Chapter 5, an accurate sky model was compiled using point-source catalogues and the Haslam map as resources. An in-depth analysis was done on each resource to determine the inter-compatibility of each. After this, the necessary conversions were applied to each resource to ensure optimal spectral continuity in the resulting compiled sky model. The interference statistics were calculated and it was determined that SH is perfectly suitable for calibrating an MFAA station. The study also provided valuable insight on factors that should be considered when selecting a calibrator.

In summary, the work done in this thesis led to the following publications:

1. C.R. Wilke, S.J. Wijnholds, and J. Gilmore, "Performance improvement of self-holography based aperture array station calibration", in *2019 13th European Conference on Antennas and Propagation (EuCAP)*, 2019, pp. 1-5.

2. C.R. Wilke, S.J. Wijnholds, and J. Gilmore, "Self-holography: slimming down calibration of large aperture arrays", in *2020 XXXIIIrd General*

*Assembly and Scientific Symposium of the International Union of Radio Science*, 2020, pp. 1-4.

3. C. R. Wilke, S. J. Wijnholds, and J. Gilmore, Calibration of Large Aperture Arrays using Self-Holography, *accepted for publication in the IEEE Transactions on Antennas and Propagation*, 2021.

## 1.5 Outline of the dissertation

A literature review on the key concepts that were used in the mathematical models throughout this thesis is presented in Chapter 2. The current formulations of self-holography are presented in Chapter 3. This includes the performance improvement study on the original implementation. Chapter 4 presents the interference (and the mitigation of it) study on the latest formulation of SH and the application example on real LOFAR data. Chapter 5 presents the study on the suitability of applying SH to an MFAA station. Lastly, concluding remarks on the work done in this thesis and a discussion on planned future work, are provided in Chapter 6.

# Chapter 2

# Theoretical Framework

## 2.1 Introduction

This dissertation makes use of various signal processing concepts to accurately analyse and simulate an antenna array system. As such, it is necessary to briefly introduce some of the key concepts and the assumptions that are made in each of them. In some cases, this requires extensive derivations to point out underlying details that are not necessarily clear in the final expressions. However, an effort was made to point out the expressions that are used in the rest of the dissertation. The concepts were carefully subdivided into sections so that the reader can easily find the relevant section that explains the concept that is being used at a specific point in the dissertation.

## 2.2 Coordinate systems

Antenna engineering usually utilizes the spherical coordinate system. The direction from which radiation is received or transmitted, is described using the Ludwig 3 coordinate system [46], i.e., azimuthal angle $\phi$ and boresight angle $\theta$. The polarization of an incoming signal can then be described using the mutually orthogonal unit vectors $\mathbf{e}_{\mathrm{r}}, \mathbf{e}_{\theta}$ and $\mathbf{e}_{\phi}$. This dissertation only deals with signals in the far-field and, as such, it is reasonable to assume that the incoming wavefronts are planar with electromagnetic field components perpendicular to the direction of propagation. With this assumption, the unit vectors $\mathbf{e}_{\theta}$ and $\mathbf{e}_{\phi}$ are sufficient to characterize the polarization of an incoming wavefront.

The coordinates of cosmic sources are usually given in either right ascension $\alpha$ and declination $\delta$ where the ecliptic is used as equatorial plane, or Galactic longitude $l$ and latitude $b$ where the galactic plane is used as equatorial plane. These coordinates will require a conversion to azimuth $(az)$ and $(el)$ at the local horizon and current time of the observer before it can be used. The azimuthal angle runs along the horizon from North (0°) to East (90°) and

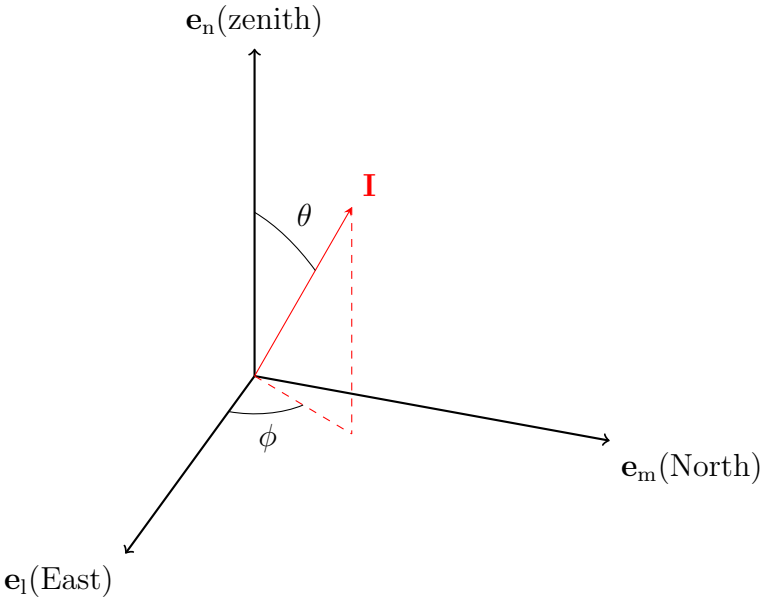


**Figure 2.1:** Coordinate systems that can be used to described incoming radiation with respect to the unit vectors $\mathbf{e}_l$, $\mathbf{e}_m$ and $\mathbf{e}_n$.

elevation is measured positively from the horizon (0°) to zenith (90°). From this, the relation to $\theta$ and $\phi$ are as follow:

$$\theta = 90^\circ - el \tag{2.1}$$
$$\phi = 90^\circ - az \tag{2.2}$$

For antenna arrays, it is convenient to project these coordinates onto a plane that touches the celestial sphere at zenith at the location of the antenna array. The position vectors of the projected coordinates are denoted by $l$ pointing towards East and $m$ pointing towards North and can be calculated as:

$$l = \sin\theta\cos\phi = \cos(el)\sin(az) \tag{2.3}$$
$$m = \sin\theta\sin\phi = \cos(el)\cos(az) \tag{2.4}$$
$$n = \cos\theta = \sin(el) \tag{2.5}$$

Figure 2.1 shows a graphical representation of the coordinate system that will be used in this dissertation. The positions of the receiving elements in the array are specified using Cartesian coordinates $\boldsymbol{\xi} = [x, y, z]^T$ where the $x$,$y$ and $z$ axis are pointing towards East, North and zenith respectively. .

## 2.3 Cosmic signals

Signals originating from cosmic sources are typically stochastic in nature. In each individual frequency channel of a receiver (assuming the channels are

narrowband [47]), their signals can be modelled as independent identically distributed Gaussian noise. The reason for this can be explained by quantum mechanics, which states that electromagnetic radiation can be described as waves or particles, called photons. Photons at radio frequencies carry very little energy. For example, at the observing frequency of the 3C catalogue [48] (178 MHz), a photon carries only $1.18{\cdot}10^{-25}$J. The flux of Cygnus A is listed in the 3C catalogue as $8100{\cdot}10^{-26}\mathrm{Wm}^{-2}\mathrm{Hz}^{-1}$. If this source is sampled with bandwidth $B$ for $\tau$ seconds with an effective area of 25 $\mathrm{m}^2$, each time sample (when $B/\tau = 1$) will only represent $2.03{\cdot}10^{-21}$ J which is over 17,000 photons which is large enough to ensure that the Poisson distribution of a photon counting experiment approximates a Gaussian distribution.

The brightness temperature of a source is defined as [49]:

$$T_{\mathrm{B}} = \frac{c^2 S}{2k_{\mathrm{b}} f^2} = \frac{\lambda^2 S}{2k_{\mathrm{b}}}, \tag{2.6}$$

where $c$ is the speed of light in m $\mathrm{s}^{-1}$, $S$ is the flux density of the source in W $\mathrm{m}^{-2}$ $\mathrm{Hz}^{-1}$ $\mathrm{sr}^{-1}$, $k_{\mathrm{b}}$ is Boltzmann's constant ($1.38 \cdot 10^{-23}$ J $\mathrm{K}^{-1}$), $f$ is frequency in Hz and $\lambda$ is the wavelength in m. This expression will be used later in this thesis to convert a brightness temperature map to an intensity map.

The physical mechanisms involved in radiation coming from cosmic sources usually produce spectra that vary smoothly with frequency. As a result, the flux density of a source generally has a power-law relationship with frequency:

$$S(f) = S(f_0)\left(\frac{f}{f_0}\right)^{\alpha}, \tag{2.7}$$

where $\alpha$ is the spectral index. This expression is used in chapter 5 to scale the integrated flux values of sources to other frequencies.

## 2.4 Reception of cosmic signals

The power received by an antenna from an unresolved source with random polarisation is defined as:

$$P_{\mathrm{A}} = k_{\mathrm{b}} T_{\mathrm{A}} B, \tag{2.8}$$

where B is the observing bandwidth in Hz and $T_{\mathrm{A}}$ is the antenna temperature in Kelvin due to the source, which is defined as:

$$T_{\mathrm{A}} = \frac{S A_{\mathrm{eff}}}{2k_{\mathrm{b}}}, \tag{2.9}$$

where $S$ is the flux of the source and $A_{\mathrm{eff}}$ is the effective area of the antenna. Substituting this into (2.8) results in:

$$P_{\mathrm{A}} = \frac{1}{2} S A_{\mathrm{eff}} B. \tag{2.10}$$

The sensitivity of the antenna plus receiver can be described by the system equivalent flux density (SEFD) which is defined as the flux of an unresolved source in the main beam that will cause the noise power to be twice the system noise in the absence of the source. Equating (2.10) to $k_{\mathrm{b}}T_{\mathrm{sys}}B$ results in the following definition for the SEFD:

$$\mathrm{SEFD} = \frac{2k_{\mathrm{b}}T_{\mathrm{sys}}}{A_{\mathrm{eff}}}. \tag{2.11}$$

The instantaneous SNR of the signal measurement is defined as $T_{\mathrm{A}}/T_{\mathrm{sys}}$. By using (2.9) and (2.11), the SNR can be related to the SEFD as:

$$\mathrm{SNR} = \frac{S}{\mathrm{SEFD}}. \tag{2.12}$$

Equations 2.11 and 2.12 will regularly be used in this thesis.

## 2.5 The measured signal

The time-varying electric field (E-field) incident at position $\mathbf{r}$ (on the horizontal plane), from a source located at $\mathbf{l}$ is described as:

$$\mathbf{E}\left(\mathbf{r}, f, t\right) = \mathbf{E}_0(\mathbf{l}, f, t)e^{j2\pi f(\mathbf{r}\cdot\mathbf{l}/c - t)}, \tag{2.13}$$

where $\mathbf{E}_0 = [E_{0\theta}, E_{0\phi}, E_{0r}]^T$ is the plane wave spectrum emitted by the source and describes the complex amplitude distribution in $\mathbf{e}_{\mathrm{r}}, \mathbf{e}_\theta$ and $\mathbf{e}_\phi$. A plane wave will have no component along the direction of propagation and therefore $\mathbf{E}_0 = [E_{0\theta}, E_{0\phi}]^T$ is sufficient to describe the field. The variable $f$ denotes frequency and $c$ is the speed of light. For multiple sources, the total incident field is simply a superposition of all fields at that point:

$$\mathbf{E}\left(\mathbf{r}, f, t\right) = \int \mathbf{E}_0(\mathbf{l}, f, t)e^{j2\pi f(\mathbf{r}\cdot\mathbf{l}/c - t)}d\Omega, \tag{2.14}$$

where $d\Omega$ is a differential solid angle element on the hemisphere above the horizon. By introducing the wave vector $\mathbf{k} = -2\pi f\mathbf{l}/c$, (2.13) can also be written as:

$$\mathbf{E}\left(\mathbf{r}, \mathbf{k}, t\right) = \mathbf{E}_0(\mathbf{k}, t)e^{-j\left(\mathbf{k}^T\mathbf{r} - |\mathbf{k}|ct\right)}, \tag{2.15}$$

The amount of power that will be received by the $p$th antenna with position vector $\boldsymbol{\xi}$ is dependent on the sensitivity of that element in the direction of the source. The sensitivity of the element is dependent on orientation of the antenna in relation to the polarisation of the sources, and the voltage response pattern (also called the radiation pattern) $\mathbf{E}_p$ that is both direction and frequency dependent. The open circuit voltage $v_{\mathrm{oc,p}}$ measured at the terminals of the antenna will be [50]:

$$v_{\mathrm{oc},p}(\mathbf{k}, t) = \frac{4\pi j\boldsymbol{\xi}_0 e^{j|\mathbf{k}|\boldsymbol{\xi}_0}}{|\mathbf{k}|\eta I_0}\mathbf{E}_p(\mathbf{k}) \cdot \mathbf{E}_0(\mathbf{k}, t)e^{-j\left(\mathbf{k}^T\boldsymbol{\xi} - |\mathbf{k}|ct\right)}, \tag{2.16}$$

where $\xi_0$ is the distance at which the voltage response pattern of the antenna is measured and $\eta$ is the intrinsic impedance of the propagation medium. For free space, $\eta$ is equal to 377 $\Omega$.

The voltage at the terminals of the antenna is amplified by a low noise amplifier (LNA), filtered and transported before it is digitised with an analogue to digital converter (ADC). This analog receive path between the antenna output port and the input port of the ADC has a transfer function $g_{\mathrm{p}}(f,t)$ that will be referred to as the direction-independent, complex valued gain of the analogue receive path. The input voltage $v_{\mathrm{p}}$ at the ADC can thus be expressed as:

$$v_p(\mathbf{k},t) = g_p(f,t)v_{\mathrm{oc},p}(\mathbf{k},t). \tag{2.17}$$

For an array of antennas, the antenna outputs and receive path gains can be stacked in $P \times 1$ column vectors, such that $\mathbf{v}_{\mathrm{oc}} = [v_{\mathrm{oc},1}, v_{\mathrm{oc},2}, \ldots, v_{\mathrm{oc},p}]^T$ and $\mathbf{g} = [g_1, g_2 \ldots, g_P]$.. Each antenna in the array will interact in the form of mutual coupling. This can be explained by the laws of Faraday and Ampere. Ampere's law states that a time varying magnetic field will exist around the antenna that is a result of the time-varying current that is flowing on the antenna. According to Faraday, an antenna in the vicinity of the this magnetic field will experience an induced current. The impedance of the output of the array is described by a mutual impedance matrix $\mathbf{Z}_{\mathrm{A}}$ and the input impedance of the receiver chain network is described by the impedance matrix $\mathbf{Z}_{\mathrm{R}}$, such that the input voltages to the ADC can be described by $P \times 1$ column vector $\mathbf{v}(\mathbf{k},t)$ as [51]:

$$\begin{aligned} \mathbf{v}(\mathbf{k},t) &= \mathbf{G}(f)\mathbf{Z}_{\mathrm{R}}(f)\left(\mathbf{Z}_{\mathrm{R}}(f)+\mathbf{Z}_{\mathrm{A}}(f)\right)^{-1}\mathbf{v}_{\mathrm{oc}}(\mathbf{k},t) \\ &= \mathbf{G}(f)\mathbf{Q}(f)\mathbf{v}_{\mathrm{oc}}(\mathbf{k},t), \end{aligned} \tag{2.18}$$

where $\mathbf{G} = \mathrm{diag}(\mathbf{g})$ and $\mathbf{Q} = \mathbf{Z}_{\mathrm{R}}(f)\left(\mathbf{Z}_{\mathrm{R}}(f)+\mathbf{Z}_{\mathrm{A}}(f)\right)^{-1}$ describes the mutual coupling between the elements. This shows that the input to each ADC is a function of the output of the specific receive path and a scaled and delayed version of the outputs of all the other receive paths in the array. Mutual coupling is not considered in the models used in this dissertation, but it is still important to point out where it fits in reality. For now, the mutual coupling term will be included in the following derivations.

By assuming the narrowband condition, the frequency dependence in the above expressions will be dropped. The total output voltage for each antenna in the array can be obtained by integrating (2.18) over the hemisphere above the horizon:

$$\mathbf{v}(t) = \int_{-\pi}^{\pi}\int_{0}^{\pi/2} \mathbf{G}\mathbf{Q}\mathbf{v}_{\mathrm{oc}}(\mathbf{l},t)|\sin(\theta)|d\theta d\phi = \int_{\Omega} \mathbf{G}\mathbf{Q}\mathbf{v}_{\mathrm{oc}}(\mathbf{l},t)d\Omega. \tag{2.19}$$

The entries of the vector $\mathbf{v}_{\mathrm{oc}}(\mathbf{l},t)$ are defined according to (2.16) where $\mathbf{E}_p(\mathbf{l})$ now represents the embedded element pattern (EEP) of element $p$, i.e., the

radiation pattern of the element when placed in an array with all other elements terminated with matched loads. A direction dependent gain term $g_{0p}$ can be introduced per element by splitting $\mathbf{E}_0(\mathbf{l},t)$ into a unit polarization vector $\mathbf{e}_0(\mathbf{l},t)$ and signal term $s(\mathbf{l},t)$, and then combining it with the radiation pattern $\mathbf{E}_p(\mathbf{l})$ as:

$$g_{0p}(\mathbf{l},t) = \frac{4\pi j \boldsymbol{\xi}_{0p} e^{j|\mathbf{k}|\boldsymbol{\xi}_0}}{|\mathbf{k}|\eta I_0}\mathbf{e}_0(\mathbf{l},t)\cdot\mathbf{E}_p(\mathbf{l}). \tag{2.20}$$

Additional direction dependent effects such as distortion of the incoming signal due to ionospheric variations, can be added as complex multiplicative factors.

The phase of an incoming plane wave at element $p$ is denoted by the phasor $a_p(\mathbf{l},t)$ which is defined as:

$$a_p(\mathbf{l},t) = e^{-j\left(\mathbf{k}^T\boldsymbol{\xi}_p - |\mathbf{k}|ct\right)}. \tag{2.21}$$

By stacking the element positions in $p\times 3$ matrix $\boldsymbol{\Xi} = [\xi_1,\xi_2,\ldots,\xi_P]^T$, the $P\times 1$ array response vector $\mathbf{a}(\mathbf{l},t)$ can be calculated as:

$$\mathbf{a}(\mathbf{l},t) = \frac{1}{\sqrt{P}}e^{-j(\boldsymbol{\Xi}\mathbf{k}-|\mathbf{k}|ct)}, \tag{2.22}$$

where $1/\sqrt{P}$ normalizes the vector such that $\mathbf{a}^H(\mathbf{l},t)\mathbf{a}(\mathbf{l},t) = 1$.

By stacking the direction-dependent gains in $\mathbf{g}_0(\mathbf{l},t) = [g_{01}(\mathbf{l},t), g_{02}(\mathbf{l},t),\ldots g_{0P}(\mathbf{l},t)]^T$, (2.19) can be written as:

$$\mathbf{v}(t) = \int_\Omega \mathbf{GQ}\left(\mathbf{a}(\mathbf{l},t)\odot\mathbf{g}_0(\mathbf{l},t)\right)s(\mathbf{l},t)d\Omega, \tag{2.23}$$

where $\odot$ represents the Hadamard product or element-wise multiplication of two vectors or matrices.

The influence of thermal noise $n(t)$ in the receive paths has been ignored up to this point. With the noise of all the receive paths stacked in $P\times 1$ vector $\mathbf{n}(t) = [n_1(t), n_2(t),\ldots,n_P(t)]^T$, the input voltages to the ADC's can be described as:

$$\mathbf{v}(t) = \int_\Omega \mathbf{GQ}\left(\mathbf{a}(\mathbf{l},t)\odot\mathbf{g}_0(\mathbf{l},t)\right)s(\mathbf{l},t)d\Omega + \mathbf{n}(t). \tag{2.24}$$

## 2.6 The array covariance matrix

The array covariance matrix $\boldsymbol{\Sigma}$ which represents the expected value of the visibilities, can now be calculated as:

$$\boldsymbol{\Sigma} = \mathcal{E}\left\{\mathbf{v}(t)\mathbf{v}^H(t)\right\}. \tag{2.25}$$

Using (2.24) and (2.19), we find:

$$\boldsymbol{\Sigma} = \mathcal{E}\left\{\left(\int_\Omega \mathbf{GQ}\mathbf{v}_{\mathrm{oc}}(\mathbf{l},t)d\Omega + \mathbf{n}(t)\right)\left(\int_\Omega \mathbf{GQ}\mathbf{v}_{\mathrm{oc}}(\mathbf{l},t)d\Omega + \mathbf{n}(t)\right)^H\right\}. \tag{2.26}$$

Since $\mathbf{n}(t)$ is uncorrelated with the antenna output signals $\mathbf{v}_{\text{oc}}(\mathbf{l},t)$, this can also be written as:

$$\boldsymbol{\Sigma} = \mathcal{E}\left\{\left(\int_{\Omega}\mathbf{GQ}\mathbf{v}_{\text{oc}}(\mathbf{l},t)d\Omega\right)\left(\int_{\Omega}\mathbf{GQ}\mathbf{v}_{\text{oc}}(\mathbf{l},t)d\Omega\right)^{H}\right\} + \mathcal{E}\left\{\mathbf{n}(t)\mathbf{n}^{H}(t)\right\}, \tag{2.27}$$

which shows that the array covariance matrix can be split into signal and noise covariance matrices that respectively represent the contribution from the measured signal and the noise generated by the receive paths:

$$\boldsymbol{\Sigma} = \boldsymbol{\Sigma}_{\text{s}} + \boldsymbol{\Sigma}_{\text{n}}. \tag{2.28}$$

By assuming that the source signals are spatially uncorrelated, the array covariance matrix for the measured signal can be written as:

$$\boldsymbol{\Sigma}_{\text{s}} = \mathbf{GQ}\left(\int_{\Omega}\mathcal{E}\left\{\mathbf{v}_{\text{oc}}(\mathbf{l},t)\mathbf{v}_{\text{oc}}^{H}(\mathbf{l},t)\right\}d\Omega\right)\mathbf{Q}^{H}\mathbf{G}^{H}. \tag{2.29}$$

By substituting the factorization of $\mathbf{v}_{\text{oc}}(\mathbf{l},t)$ as shown in (2.23) and taking the expected values, this can be written as:

$$\boldsymbol{\Sigma}_{\text{s}} = \mathbf{GQ}\left(\int_{\Omega}\left(\mathbf{a}(\mathbf{l})\odot\mathbf{g}_0(\mathbf{l})\right)\sigma_{\text{s}}(\mathbf{l})\left(\mathbf{a}(\mathbf{l})\odot\mathbf{g}_0(\mathbf{l})\right)\right)^{H}d\Omega\Bigg)\mathbf{Q}^{H}\mathbf{G}^{H}, \tag{2.30}$$

where $\sigma_{\text{s}}(\mathbf{l}) = \varepsilon\left\{s(\mathbf{l},t)\bar{s}(\mathbf{l},t)\right\}$ represents the signal power coming from $\mathbf{l}$.

If the signals originate from Q discrete sources, which is typically the assumed scenario in this dissertation, then $\boldsymbol{\Sigma}_{\text{s}}$ can also be written as:

$$\boldsymbol{\Sigma}_{s} = \mathbf{GQ}\left(\sum_{q=1}^{Q}\left(\mathbf{a}_q\odot\mathbf{g}_{0q}\right)\sigma_q\left(\mathbf{a}_q\odot\mathbf{g}_{0q}\right)^{H}\right)\mathbf{Q}^{H}\mathbf{G}^{H}. \tag{2.31}$$

A final simplification can be done by introducing the $P\times Q$ matrices $\mathbf{A} = [\mathbf{a}_1,\mathbf{a}_2,\ldots,\mathbf{a}_Q]$ and $\mathbf{G}_0 = [\mathbf{g}_{01},\mathbf{g}_{02},\ldots,\mathbf{g}_{0Q}]$, and the $Q\times Q$ matrix $\boldsymbol{P}_{\text{s}} = \text{diag}([\sigma_1,\sigma_2,\ldots,\sigma_Q]^T)$, such that:

$$\boldsymbol{\Sigma}_{\text{s}} = \mathbf{GQ}\left(\mathbf{A}\odot\mathbf{G}_0\right)\boldsymbol{P}_{\text{s}}\left(\mathbf{A}\odot\mathbf{G}_0\right)^{H}\mathbf{Q}^{H}\mathbf{G}^{H}. \tag{2.32}$$

If the voltages are sampled with sample time T, then the $n$th time sample of the array signal vector $x[n]$ can be written using a source descretized version of (2.24):

$$x[n] = \mathbf{GQ}\left(\sum_{q=1}^{Q}\left(a_q(nT)\odot g_{0q}(nT)\right)s_q(nT)\right) + \mathbf{n}(nT). \tag{2.33}$$

The Q source signals can be compiled in
$Q \times 1$ vector $\mathbf{s}(nT) = [s_1(nT), s_2(nT), \ldots, s_Q(nT)]^T$. Using this definition with $\mathbf{A}$ and $\mathbf{G}$ as defined previously, (2.33) can be written as:

$$x[n] = \mathbf{GQ}\left(\mathbf{A} \odot \mathbf{G}_0\right)\mathbf{s}(nT) + \mathbf{n}(nT) \tag{2.34}$$

For N samples, the signal vectors can be stacked in $P \times N$ matrix $\mathbf{X} = [\mathbf{x}[1], \mathbf{x}[2]], \ldots, \mathbf{x}[N]]$. Over $N$ samples (which is called an integration interval), the short term integrated array covariance matrix is estimated as:

$$\mathbf{\Sigma} = \frac{1}{N}\mathbf{X}\mathbf{X}^H. \tag{2.35}$$

Equation 2.35 will regularly be used in this dissertation.

## 2.7 Signal subspace

Eigenvalue decomposition is a powerful tool for the analysis of array covariance matrices. It is often used in high resolution direction-of-arrival estimation [52], [53] and source detection [54], [55]. It is also very useful to determine the number of sources to include in a source model for accurate calibration. In this project, it will be used to analyse and distinguish signal and interference components in a measured covariance matrix to calculate the signal-to-interference ratio (SIR).

Eigenvalue decomposition decomposes the array covariance matrix in a set of orthonormal eigenvectors:

$$\mathbf{\Sigma} = \mathbf{V}\mathbf{\Lambda}\mathbf{V}^H, \tag{2.36}$$

where $\mathbf{V}$ is a full rank $P \times P$ matrix containing the eigenvectors and $\mathbf{\Lambda}$ is a $P \times P$ diagonal matrix containing the eigenvalues $\lambda_1, \lambda_2, \ldots \lambda_P$ along its main diagonal. This can further be split into eigenvectors associated with the source signals and eigenvectors associated with the noise signals:

$$\mathbf{\Sigma} = \mathbf{V}_\mathrm{s}\mathbf{\Lambda}_\mathrm{s}\mathbf{V}_\mathrm{s}^H + \mathbf{V}_\mathrm{n}\mathbf{\Lambda}_\mathrm{n}\mathbf{V}_\mathrm{n}^H \tag{2.37}$$

## 2.8 Spatial filtering and imaging

Spatial filtering is the process of coherently adding signals coming from the desired direction while suppressing signals coming from unwanted directions. This is done in an operation called beamforming where an appropriate weight is assigned to each antenna in the array prior to the addition of all the signals.

The voltage output of a classical delay beamformer of an array with isotropic element patterns (i.e., $\mathbf{G}_0$ is a $P \times P$ matrix with all entries equal to

1), no mutual coupling between the antennas ($\mathbf{Q} = \mathbf{I}$) and unity receiver gain ($\mathbf{G} = \mathbf{I}$), pointed to $\mathbf{l}_0$ is described as:

$$y(t) = \mathbf{w}^H(\mathbf{l}_0)\mathbf{a}_s(\mathbf{l}_s)s_s(t), \tag{2.38}$$

where $\mathbf{w}(\mathbf{l}_0)$ is the vector containing the antenna weights, $\mathbf{a}_s(\mathbf{l}_s)$ is the array response vector and $s_s(t)$ is the source signal. From this it is clear that to maximise the amplitude of $s_s(t)$ it is required that $\mathbf{w}(\mathbf{l}_0) = \mathbf{a}_s(\mathbf{l}_s)$. In practice, the weight vector will generally contain small imperfections due to phase quantization and calibration errors. If the RMS phase error $\sigma_\phi$ is reasonably small, [56] shows that the beamformer efficiency $\eta_{\text{BF}}$ can be calculated as:

$$\eta_{\text{BF}} = \cos^2(\sigma_\phi). \tag{2.39}$$

This expression will be used later in this thesis to assess the severity of calibration errors.

As explained earlier, the input signal is stochastic in nature, so the output of the beamformer will be stochastic as well. Therefore, the power of the beamformer output can be described as:

$$\begin{aligned} \mathcal{E}\left\{|y(t)|^2\right\} &= \varepsilon\left\{\mathbf{w}^H(\mathbf{l}_0)\mathbf{a}_s(\mathbf{l}_s)s_s(t)\bar{s}_s(t)\mathbf{a}_s^H(\mathbf{l}_s)\mathbf{w}(\mathbf{l}_0)\right\} \\ &= \mathbf{w}^H(\mathbf{l}_0)\mathbf{\Sigma}_s(\mathbf{l}_s)\mathbf{w}(\mathbf{l}_0), \end{aligned} \tag{2.40}$$

in which the equivalence of beamforming to the coherent addition of visibilities is apparent. The process of coherently adding visibilities is generally called imaging. A detailed discussion on this equivalence is provided in [57]. The main difference between beamforming and imaging is that an imager can assign baseline weights which provides more flexibility compared to individual antenna based weights.

This form of beamforming essentially describes a direct Fourier transform, which makes it particularly attractive for regular arrays that can exploit the fast Fourier transform. Unfortunately, it also suffers from the same sampling effects as the Fourier transform. For example, a sparsely sampled aperture (element spacing $> \lambda/2$) will result in spatial aliasing in the form of grating lobes [58]. A grating lobe has the same magnitude as the main lobe, and, as a result, the array will be unable to distinguish between signals coming from the main lobe and a grating lobe.

More sophisticated beamforming techniques have been proposed in which power from unintended directions is minimised. Unfortunately, these methods depend on the details of the array covariance matrix, which can make it computationally expensive for large arrays. However, they can be particularly useful in scenarios where strong RFI sources are present. As a result, the use of these more advanced beamformers has been demonstrated on real data [59], [60].

This thesis analyses a calibration method that avoids the calculation of the array covariance matrix. The beamformer described by (2.38) is, therefore,

the most appropriate for most of the analysis in this thesis. In some practical examples, an array covariance matrix measurement is provided in which case (2.40) will be used.

The imaging process that is based on consecutive pointings of the array beam within the FoV of the array using (2.40) is called a direct Fourier transform imager. This is the type of imager that will be used in this thesis since it is the simplest and its capabilities are more than sufficient for the imaging examples that will be presented.

## 2.9 Conclusion

This chapter introduced the key signal processing concepts that are used throughout this dissertation. In some cases, this required extensive derivations to point out underlying details and assumptions that are not necessarily clear in the final expression. However, in each section an effort was made to point out the expressions that are actually used in this dissertation.

The following chapter introduces the self-holography calibration method.

# Chapter 3

# Self-Holography

## 3.1 Introduction

The holographic measurement technique [49] is commonly used to derive the surface accuracy of reflector antennas. The technique stems from the Fourier relation between the voltage response pattern of an antenna and the electric field distribution in its aperture plane. The amplitude of the voltage response pattern is measured by scanning the antenna under test over the direction of a transmitter while the phase of the response pattern is measured using a second non-scanning antenna. Here the aim is to derive the direction-independent gains of the receivers which are related to the aperture distribution function. By beamforming the array to an isolated point source, the distribution function can be sampled in amplitude and phase by correlating the obtained point source signal with the signals of the individual receive paths in the array. The accuracy of the sampling, which is thoroughly discussed in this chapter, is highly dependent on the operating conditions of the array and the specific formulation of the method. The point source signal and the array beam used to obtain it will further be referred to as the reference signal and reference beam respectively. Since the holographic measurement is done using the array as both the antenna under test and the probe, the name "self-holography" (SH), was appropriately chosen by Wijnholds in [43].

Currently, there are two formulations of SH. The original formulation is presented first. The results from the original study [43] on the basic method are reproduced to provide the reader with a comprehensive understanding of its drawbacks that led to the second formulation and the subsequent novel work in this thesis. Possible solutions to these issues as originally suggested in [44] are also presented and discussed. This is followed by an introduction to the latest formulation of SH that was published in [61].

## 3.2 Original implementation and its drawbacks

This section introduces the basic formulation of the self-holography method that was originally presented in [43].

### The model

A station consists of $P$ tiles, each combining $M$ antennas in an analogue beamforming stage. To maintain a clear connection with the original work, in this Chapter which is based on [43], [44], $M$ denotes the total number of elements on a tile, while in Chapters 4 and 5 which are based on [45], [61], $M$ denotes the number of elements on a side of a tile.

There are $P$ receive paths with unknown complex gains. It is assumed that a calibration source is located in both the tile and reference beam. With the narrowband condition assumed, the geometric delay of the calibration signal at the $m$th antenna in the $p$th tile at frequency $f$ is described by the phasor $a_{p,m} = e^{2\pi j \boldsymbol{\xi}_{p,m} \cdot \mathbf{l}/\lambda}$, where $\boldsymbol{\xi}_{p,m}$ is the position vector of the $m$th antenna in the $p$th tile and $l$ is the direction cosine of the phase reference position. The source is spatially filtered by applying the weights $w_{p,m} = a_{p,m}$ in the analogue beamforming stage. With the beamforming weights stacked in $M \times 1$ vector $\mathbf{w}_p$, the delay phasors in $M \times 1$ vector $\mathbf{a}_p$ and the receiver noise in $M \times 1$ vector $\mathbf{n}_p(t)$, the signal at the $p$th tile can be expressed as:

$$x_p(t) = g_p \mathbf{w}_p^H (\mathbf{a}_p s(t) + \mathbf{n}_p(t)), \tag{3.1}$$

where $g_p$ denotes the receive path gain for the $p$th tile and $s(t)$ denotes the signal from the calibration source. It is assumed that the attenuation by the element pattern is included in the signal term $s(t)$. By assuming $\mathbf{a}_p$ exactly compensates for $\mathbf{w}_p$, (3.1) can be rewritten as:

$$x_p(t) = g_p M s(t) + \mathbf{w}_p^H \mathbf{n}_p(t). \tag{3.2}$$

With the tile signals stacked in $P \times 1$ vector $\mathbf{x}(t)$, the reference beam signal $y(t)$ is formed by multiplying it with the $P \times 1$ weight vector $\mathbf{w}_{\text{ref}}$:

$$y(t) = \mathbf{w}_{\text{ref}}^H \mathbf{x}(t). \tag{3.3}$$

The expected value of the crosscorrelations between the tile signals and the reference signal ($\mathbf{r}_{\text{xy}}$) are calculated as:

$$\begin{aligned} \mathbf{r}_{\text{xy}} &= \mathcal{E}\left\{\mathbf{x}(t) y(t)^H\right\} \\ &= \mathcal{E}\left\{\mathbf{x}(t) \left(\mathbf{w}_{\text{ref}}^H \mathbf{x}(t)\right)^H\right\} \\ &= \mathbf{g}(\mathbf{g}^H \mathbf{w}_{\text{ref}}) M^2 \sigma_{\text{cal}} + M \sigma_{\text{n}} \mathbf{w}_{\text{ref}}, \end{aligned} \tag{3.4}$$

where $\sigma_{\text{cal}}$ is the apparent power of the calibration source and $\sigma_{\text{n}}$ is the noise power in an individual antenna. From this, it can be seen that the measured correlations are directly proportional to the true gain vector $\mathbf{g}$ if the SNR is high enough. The proportionality constant is related to the power of the reference signal which can be calculated by its autocorrelation as:

$$r_{\text{yy}} = \left|\mathbf{w}_{\text{ref}}^H \mathbf{g}\right|^2 M^2 \sigma_{\text{cal}} + (\mathbf{w}_{\text{ref}}^H \mathbf{w}_{\text{ref}}) M \sigma_{\text{n}}. \tag{3.5}$$

Dividing (3.4) with (3.5) gives:

$$\frac{\mathbf{r}_{\text{xy}}}{r_{\text{yy}}} = \frac{\mathbf{g}(\mathbf{g}^H \mathbf{w}_{\text{ref}}) M^2 \sigma_{\text{cal}} + M \sigma_{\text{n}} \mathbf{w}_{\text{ref}}}{\left|\mathbf{w}_{\text{ref}}^H \mathbf{g}\right|^2 M^2 \sigma_{\text{cal}} + (\mathbf{w}_{\text{ref}}^H \mathbf{w}_{\text{ref}}) M \sigma_{\text{n}}}. \tag{3.6}$$

The reference beam weights are chosen as:

$$\mathbf{w}_{\text{ref}} = \mathbf{1} \oslash \bar{\mathbf{g}}_0 / P, \tag{3.7}$$

where $\mathbf{g}_0$ is the current best gain estimate. In this way, the true gains can be estimated in an iterative manner.

If $M^2 \sigma_{\text{cal}}$ dominates the noise-related term in the numerator and the denominator, then $\mathbf{r}_{\text{xy}}/r_{yy}$ will converge towards the true gain value after a number of iterations. If the noise-related terms are not negligible then the gain estimates will converge with a bias. The dependencies of this bias will be analysed in the simulation section below.

## Initial results

The simulation results in [43] are reproduced in this section to highlight the issues of this SH formulation. A dense regular array with an antenna pitch of 0.125 m is assumed. A fixed number of 100,096 antenna elements are chosen such that the array can be divided into an integer number of tiles for $M \in \{4, 16, 64, 256\}$. It is assumed that calibration should be done using a source inside the FoV of the tile. The power of the calibration source is based on the source statistics collected in [62]. A Monte Carlo simulation is implemented where the true receive path gains are modelled as zero-mean Gaussian noise on the real and imaginary part with a standard deviation of 0.1 added to a nominal value of unity ($g_{\text{p}} = 1 + CN(0, 0.1)$). The true gains are calibrated by applying (3.6) up to 20 times, where after each iteration, $\mathbf{w}_{\text{ref}}$ is updated according to (3.7). Expected values were used for the signal terms to isolate the effects of the SNR in (3.6). Figure 3.1 shows the typical SNR with which $\mathbf{r}_{\text{xy}}/r_{\text{yy}}$ can be measured before and after integration over 10 MHz and 10 s. The SNR per element ($\text{SNR}_{\text{elem}}$) is shown additionally on the same axis. The SNR per element depends on the FoV which explains its dependence on tile size. The SNR of the measurement depends on both the SNR per element and the sensitivity of the station. However, a very weak dependence on tile size

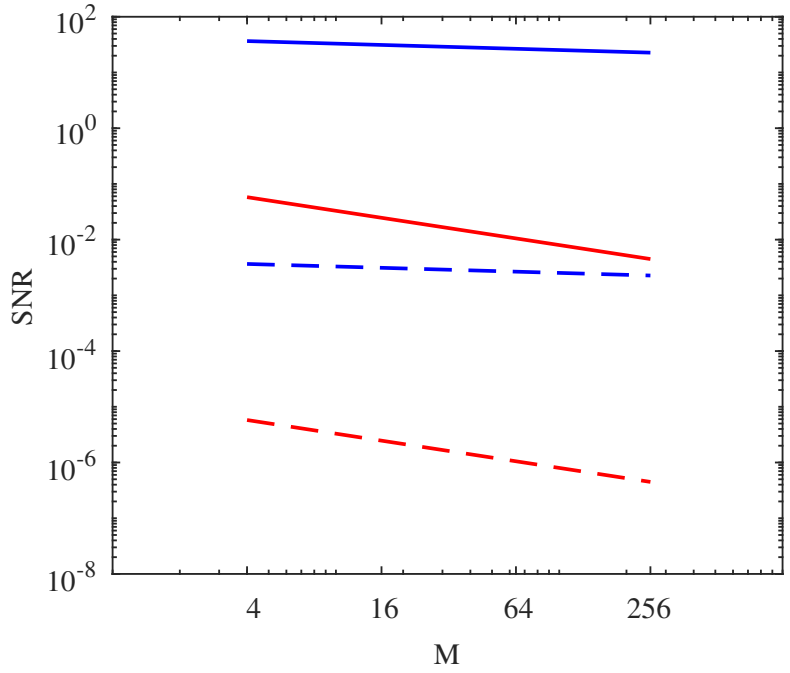


**Figure 3.1:** SNR with which $\mathbf{r}_{xy}/r_{yy}$ can typically be measured before (dashed blue line) and after (solid blue line) integration over 10 MHz and 10 s. The red lines show the corresponding SNR values for a single antenna element in the array.

is noted, indicating that the SNR of the measurement is mostly dependent on the sensitivity of the station.

Figure 3.2 shows the mean magnitude and phase errors of the gain estimates as a function of iteration. The gain magnitudes converge to a fixed offset from the true gains indicating a bias. It is also seen that the bias is dependent on tile size. Conversely, the gain phases will converge to their true values after iterating long enough. The speed of convergence is dependent on the tile size. Using these gain estimates for calibration will therefore provide high pointing accuracy of the main beam, but the station will be unable to reach optimal sensitivity due to the noisy aperture weighting that is a result of the offsets in the gain amplitudes.

## Improvements

The oscillation of the gain amplitudes are commonly observed in alternating direction implicit schemes as well [30], [40]. A typical solution to this is to implement an averaging scheme where every gain estimate is averaged with the previous estimate [30]. For self-holography, this can simply be implemented using Algorithm 1. The results after applying averaging are shown in Figure 3.2. Overall, a dramatic increase in the speed of convergence is achieved. The quicker convergence as $P$ decreases can be explained by the relatively constant oscillation amplitude as a function of iteration number for those values of $P$.

The noise related terms in (3.6) are a function of only one unknown - the individual element noise power which is defined as $\sigma_{\mathrm{n}} = \sigma_{\mathrm{cal}}/\mathrm{SNR}_{\mathrm{elem}}$. Assuming a fixed $T_{\mathrm{sys}}$ for all elements, the SNR will solely vary as a function of FoV which is dependent on the tile size. The effect of tile size (and FoV) is evident when studying the results in Fig. 3.2.

Phased antenna arrays can form multiple beams which means that, in theory, a hemispherical FoV can be achieved by "filling" the sky with beams. In this case, the noise-related terms will be independent of tile size. A simulation is performed to illustrate this in more detail. For consistency, the simulation model remains unchanged from the previous.

Figure 3.3 show the mean error of the estimated gain amplitude and phase when a hemispherical FoV is assumed. As expected, the bias is now almost equal for each value of $P$. The fact that they are not exactly equal is caused by the fact that, after each iteration, the weights for the reference beam are updated in an attempt to compensate the gain differences between the receive paths while forming the reference beam. According to (3.6), this also affects the noise contribution of the individual receive paths. As a result, the exact relation between the signal and the noise term in both the numerator and the denominator does not only depend on the SNR per element but also the level of variation between the receive path gains. Since the noise power term is dependent on the sky and the operating conditions of the array, it should, in theory, be possible to estimate the noise term given an accurate model of the sky and the array. If the noise power can be estimated accurately, then it can be compensated for by subtracting the noise-related term during measurement. This method was tested by simulation using Algorithm 2.

The gain estimate results are shown in Fig 3.4. It is seen that a bias is still present. However, it is significantly lower than in the previous results, indicating that the true gains have been more accurately estimated. It is also interesting to notice that the mean absolute difference between the estimated amplitude and phase does not change by iteration. This can be explained by considering (3.6) when compensated for noise:

$$\frac{\mathbf{r}_{\mathrm{xy}}}{r_{\mathrm{yy}}} = \frac{\mathbf{g}(\mathbf{g}^H \mathbf{w}_{\mathrm{ref}})}{\left|\mathbf{w}_{\mathrm{ref}}^H \mathbf{g}\right|^2}, \tag{3.8}$$

which can also be expressed as:

$$\frac{\mathbf{r}_{\mathrm{xy}}}{r_{\mathrm{yy}}} = \frac{\mathbf{g}\sum_{p=1}^{P} \frac{g_p}{g_{0,p}P}}{\left|\sum_{p=1}^{P} \frac{g_p}{g_{0,p}P}\right|^2} = \mathbf{g}\frac{\alpha}{|\alpha|^2}, \tag{3.9}$$

where $\alpha$ represents the sum term in the numerator and denominator. If the initial estimated gains are initialised as $\mathbf{g}_0 = \mathbf{1}$, and $P$ is large, then $\alpha$ will

approach 1 if the true gain differences are reasonably small, resulting in $\mathbf{g_0} = \mathbf{r}_{\mathrm{xy}}/r_{\mathrm{yy}} \approx \mathbf{g}$. Any further iterations will then result in the same value for $\mathbf{g}_0$. The extent of the bias can therefore be directly related to the number of receive paths in the system and their initial gain differences.

**Algorithm 1** Averaging

$\mathbf{g}_0 = \mathbf{1}$
$\mathbf{g}^{[0]} = \mathbf{g}_0$
**for** $i = 1$ to $i_{\max}$ **do**
  $\mathbf{w}_{\mathrm{ref}} = 1 \oslash \mathbf{g}_0/P$
  $\mathbf{g}^{[i]} = \mathbf{r}_{\mathrm{xy}}^{[i]}/r_{\mathrm{yy}}^{[i]}$
  $\mathbf{g}_0 = \left(\mathbf{g}^{[i]} - \mathbf{g}^{[i-1]}\right)/2$
**end for**

**Algorithm 2** Noise Correcting

$\mathbf{g}_0 = \mathbf{1}$
$\mathbf{g}^{[0]} = \mathbf{g}_0$
**for** $i = 1$ to $i_{\max}$ **do**
  $\mathbf{w}_{\mathrm{ref}} = 1 \oslash \mathbf{g}_0/P$
  $\mathbf{g}^{[i]} = \left(\mathbf{r}_{\mathrm{xy}}^{[i]} - M\sigma_{\mathrm{n}}\mathbf{w}_{\mathrm{ref}}\right) / \left(r_{\mathrm{yy}}^{[i]} - (\mathbf{w}_{\mathrm{ref}}^{H}\mathbf{w}_{\mathrm{ref}})M\sigma_n\right)$
  $\mathbf{g}_0 = \mathbf{g}^{[i]}$
**end for**

## Computational complexity

Traditional covariance matrix based calibration schemes require $4P^2\Delta f$ operations to calculate a model of the array covariance matrix. Self-holography requires that the beamformer forms a reference beam which amounts to $8P\Delta f$ operations [63], followed by correlating the signal from the reference beam with the individual tile signals which amounts to a further $4(P+1)\Delta f$ operations. If $N_{\mathrm{iter}}$ iterations are needed for the gain estimates to converge, then the required operations increase to $N_{\mathrm{iter}}\Delta f(12P+4)$. The linear scaling with $P$ makes self-holography computationally attractive when P is (very) large.

By applying the averaging method during iterations it was seen that the number of iterations required to converge to the true gains is significantly reduced, especially for large tile counts. It is therefore a remarkable improvement to the basic self-holography method since the number of required operations and measurements have been reduced even further. A trade-off between the number of receiver paths and the rate of convergence is evident. The results,

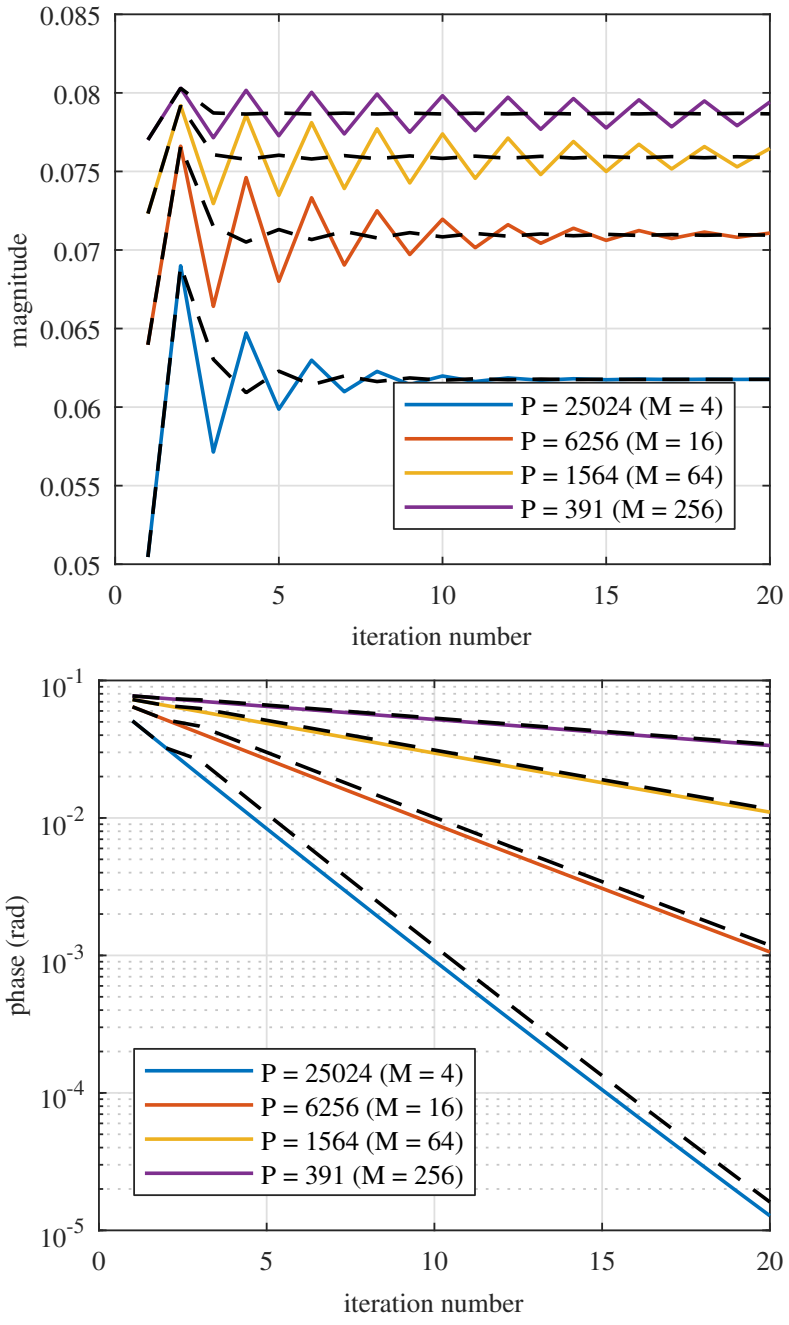


**Figure 3.2:** Mean error in magnitude (top) and phase (bottom) as a function of iteration and tile size. The black dashed lines indicate the corresponding results when averaging is applied using Algorithm 1.

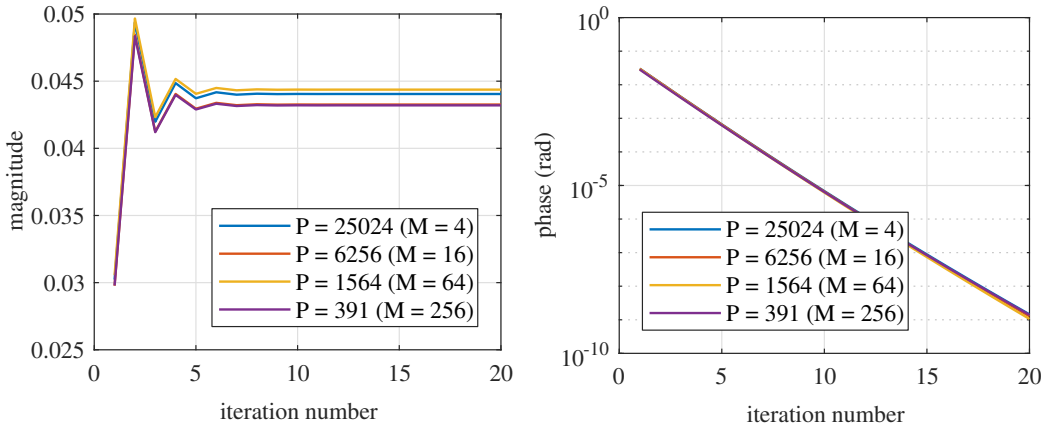


**Figure 3.3:** Mean error in magnitude (left) and phase (right) as a function of iteration and tile size when assuming a hemispherical FoV.

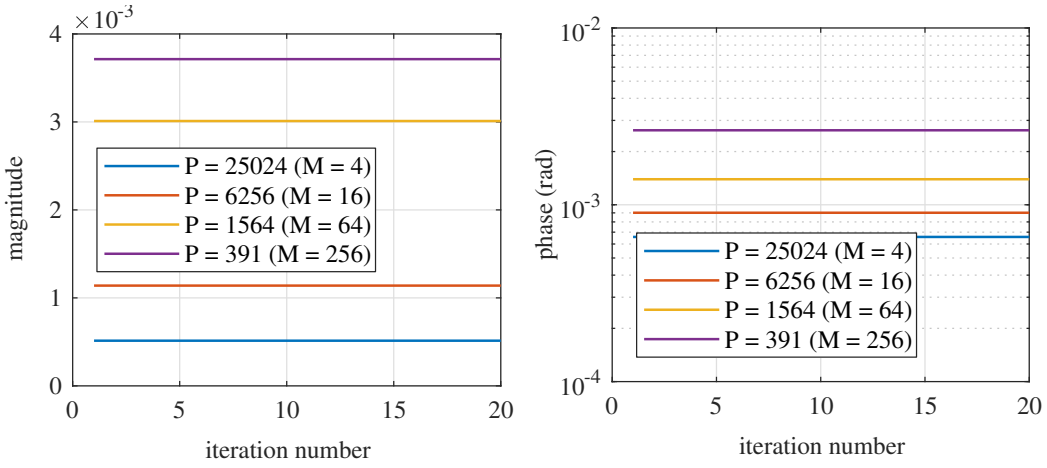


**Figure 3.4:** Mean error in magnitude (left) and phase (right) as a function of iteration and tile size while assuming a hemispherical FoV.

therefore, additionally provide a guideline from which the calibration performance can be determined given a set of design constraints.

It was also shown that the noise-related term can, theoretically, be compensated for during measurement. A simulation was performed and the results showed that the true gains are estimated fairly accurately after the first iteration and that no further iterations are required. In terms of the required computational operations, this is the largest achievable reduction. However, it was pointed out that a very accurate estimation of the noise power of individual antennas will be required. Even just a small compensation error will result in a significant reduction in estimation accuracy.

## 3.3 Estimating the gains and noise powers simultaneously

As the reference beam used in EPICal and SH is formed by the same array whose receive paths need to be calibrated, a correction is needed for the correlated noise in the individual receive paths and the reference beam [40], [44]. Below, it is shown that a rigorous mathematical formulation of the problem allows the gains and the noise powers of the individual receive paths to be solved simultaneously.

It is assumed that the complex valued gains of the receive paths are stable over the duration of the calibration signal measurement, so the time dependence of the gains is dropped in the following expressions.

If the input voltage is exactly Nyquist sampled with sample time $T$, then the number of samples produced for an integration time of $\tau$ seconds, will be equal to $N = 2f_{\max}\tau$. All $N$ measured samples can be stacked in a $P \times N$ matrix $\mathbf{X} = [\mathbf{x}(0), \cdots \mathbf{x}((N-1)T)]^T$ Similarly, the samples of the signal and noise can be stacked in matrices $\mathbf{S}$ and $\mathbf{N}$. By assuming zero mutual coupling ($\mathbf{Q} = \mathbf{I}$), EEP's that are equal ($\mathbf{G}_0 = \mathbf{I}$) and that the antenna signals are compensated for the phase delay of the calibrator, the entire measurement can be described by:

$$\mathbf{X} = \mathbf{GS} + \mathbf{N}, \tag{3.10}$$

The signal from the reference beam or reference signal $\mathbf{y}$ is formed by multiplying the measured signals $\mathbf{X}$ with the beamformer weights $\mathbf{w}$:

$$\mathbf{y} = \mathbf{w}^H\mathbf{X}, \tag{3.11}$$

where $\mathbf{w}$ is a $P \times 1$ vector containing the weights for each antenna, and $\mathbf{y}$ is the $1 \times N$ row vector containing the reference signal samples.

The expected value of the crosscorrelation between the reference and antenna signals $\mathbf{r}_{\text{xy}}$ is calculated as:

$$\mathbf{r}_{\text{xy}} = \mathcal{E}\left\{\mathbf{X}\mathbf{y}^H\right\}, \tag{3.12}$$

which, when substituting (3.10) and (3.11), becomes:

$$\begin{aligned} \mathbf{r}_{\text{xy}} &= \mathbf{G}\mathcal{E}\left\{\mathbf{S}\mathbf{S}^H\right\}\mathbf{G}^H\mathbf{w} + \mathcal{E}\{\mathbf{N}\mathbf{N}^H\}\mathbf{w} \\ &= \mathbf{G}\mathbf{\Sigma}_{\text{s}}\mathbf{G}^H\mathbf{w} + \mathbf{\Sigma}_{\text{n}}\mathbf{w}, \end{aligned} \tag{3.13}$$

where $\mathbf{\Sigma}_{\text{s}}$ and $\mathbf{\Sigma}_{\text{n}}$ denote the covariance matrices for the received voltages and noise signals respectively. The latter is assumed to be diagonal.

Next, the expected value of the autocorrelation of the antenna signals are calculated as:

$$\mathbf{r}_{\text{xx}} = \text{vecdiag}\left(\mathcal{E}\{\mathbf{X}\mathbf{X}^H\}\right), \tag{3.14}$$

where vecdiag $(\cdot)$ converts the main diagonal of its argument into a vector. When substituting (3.10), this becomes:

$$\begin{aligned}\mathbf{r}_{\text{xx}} &= \text{vecdiag}\left(\mathcal{E}\{(\mathbf{GS}+\mathbf{N})(\mathbf{GS}+\mathbf{N})^H\}\right)\\ &= \text{vecdiag}\left(\mathbf{G}\mathcal{E}\{\mathbf{SS}^H\}\mathbf{G}^H+\mathcal{E}\{\mathbf{NN}^H\}\right)\\ &= \text{vecdiag}\left(\mathbf{G}\boldsymbol{\Sigma}_{\text{s}}\mathbf{G}^H\right)+\boldsymbol{\sigma}_{\text{n}}. \end{aligned} \tag{3.15}$$

At this stage there are $2P$ equations with $2P$ unknowns, namely $\mathbf{g} = \text{vecdiag}(\mathbf{G})$ and $\boldsymbol{\sigma}_{\text{n}} = \text{vecdiag}(\boldsymbol{\Sigma}_{\text{n}})$. To solve the unknowns, the problem is first expressed as a matrix equation:

$$\begin{bmatrix}\mathbf{r}_{\text{xy}}\\ \mathbf{r}_{\text{xx}}\end{bmatrix} = \begin{bmatrix}\mathbf{G}\left(\boldsymbol{\Sigma}_{\text{s}}\mathbf{G}^H\mathbf{w}\right)+\boldsymbol{\Sigma}_{\text{n}}\mathbf{w}\\ \text{vecdiag}\left(\mathbf{G}\boldsymbol{\Sigma}_{\text{s}}\mathbf{G}^H\right)+\boldsymbol{\sigma}_{\text{n}}\end{bmatrix}, \tag{3.16}$$

which can further be factored into the following form:

$$\begin{bmatrix}\mathbf{r}_{\text{xy}}\\ \mathbf{r}_{\text{xx}}\end{bmatrix} = \begin{bmatrix}\text{diag}\left(\boldsymbol{\Sigma}_{\text{s}}\mathbf{G}^H\mathbf{w}\right) & \text{diag}(\mathbf{w})\\ \text{diag}\left(\text{vecdiag}\left(\boldsymbol{\Sigma}_{\text{s}}\mathbf{G}^H\right)\right) & \mathbf{I}\end{bmatrix}\begin{bmatrix}\mathbf{g}\\ \boldsymbol{\sigma}_{\text{n}}\end{bmatrix}, \tag{3.17}$$

where $\mathbf{I}$ is the identity matrix. This can be expressed as:

$$\mathbf{r} = \mathbf{A}\mathbf{u}, \tag{3.18}$$

where $\mathbf{r}$ is a $2P\times 1$ vector containing the measured correlations, $\mathbf{A}$ is a $2P\times 2P$ matrix containing the values as indicated above, and $\mathbf{u}$ contains the unknown gains and noise powers. This can be solved using:

$$\mathbf{u} = \mathbf{A}^{-1}\mathbf{r}. \tag{3.19}$$

Given that $\boldsymbol{\Sigma}_{\text{s}}$ in (3.17) only accounts for the calibration source, it is clear that any interference in the signal measurement will reduce the accuracy of the signal model which will subsequently affect the accuracy of the gain estimates. This will be analysed in more detail in the next chapter.

## 3.4 Conclusion

This chapter introduced the two variations (or implementations) of self-holography calibration. The original simulation results from the first variation were reproduced to highlight its issues that ultimately led to the second variation. Two methods were suggested to remedy the issues of the first implementation. The first method aimed to reduce the oscillation of the estimated gains by averaging the estimation results from the last two iterations. The results showed that the oscillation is significantly lowered, which led to a vastly improved convergence time. The second method aimed to reduce the bias observed in the gain estimates during normal operation. This was done

by assuming that the noise-related terms can be exactly predicted based on knowledge of the operating environment of the receiver. The results showed that the bias is significantly reduced and that the true gains are almost exactly estimated after the first iteration. However, it does require a very accurate compensation of the noise-related term. This can be quite challenging in practice which suggests that this issue should not be explored further. Lastly, it should be noted that without noise compensation the phase estimate error reduces to zero if sufficient iterations are made. This shows that only a small, in many cases even negligible, bias in amplitude is unavoidable in the self-holography calibration method.

The second variation of self-holography calibration allows the gains and noise powers to be solved simultaneously, which solves the issue that an accurate model of the noise powers is required to get the best possible gain estimates. However, as with the first variation, the signal model that is used to solve the unknowns is derived with the assumption that the calibration signal is entirely isolated. As a result, the accuracy of the signal model will decline when interference is present in the signal measurement. Since interference is generally unavoidable in a practical sense, its exact impact must be analysed to establish whether self-holography is suitable in any real scenario. The next chapter will thoroughly address this issue.

# Chapter 4

# Calibratability of Arrays using Self-Holography

## 4.1 Introduction

The previous chapter concluded with a self holography (SH) formulation that seems the most suitable for application in aperture arrays. The resulting simplicity of the formulation stems from the assumption that the calibration signal is entirely isolated, removing the need to model a complex array covariance matrix. Unfortunately, interference will always be present to some extent in a real environment. The degree of apparent interference for a certain spatial distribution of sources will largely be dictated by the beam pattern of the array. Based on this, it is expected that the performance of SH will increase with an increasing array size. It was also assumed that the noise covariance matrix is diagonal, implying that the noise crosscorrelation of the antennas are zero. This is a reasonable assumption to make based on the fact that the noise signals, by nature, are mutually uncorrelated. However, arrays with closely spaced antennas will experience some degree of noise coupling which will result in non-zero crosscorrelation terms in the noise covariance matrix.

This chapter investigates the impact of interference and measurement noise in SH calibration. The impact of interference and noise is initially evaluated theoretically in sections 4.2 and 4.3 to arrive at the analytical expressions that form the core of this thesis. These theoretical findings are then further analysed and established using controlled simulations in section 4.4. The final product of the theoretical analysis, combined with the findings of the simulations, is an assessment criterion that can be used to predict the performance of SH calibration in a given scenario. The assessment criterion is finally tested in section 4.5 by applying SH to three practical examples that are representative of extreme calibration scenarios.

Sections 4.2 to 4.4.2 and Section 4.5 are largely based on [61] and Section 4.4.3 is largely based on [45]. The comparison of the gain solutions obtained

by SH and StEFCal in Section 4.4.2 is an addition compared to [61].

## 4.2 The impact of interference

To assess the impact of interference, (3.17) is first rearranged to get an expression for the gain estimate:

$$\begin{bmatrix} \mathbf{g} \\ \boldsymbol{\sigma}_{\mathrm{n}} \end{bmatrix} = \begin{bmatrix} \mathrm{diag}\left(\boldsymbol{\Sigma}_{\mathrm{s}}\mathbf{G}^{H}\mathbf{w}\right) & \mathrm{diag}\left(\mathbf{w}\right) \\ \mathrm{diag}\left(\mathrm{vecdiag}\left(\boldsymbol{\Sigma}_{\mathrm{s}}\mathbf{G}^{H}\right)\right) & \mathbf{I} \end{bmatrix}^{-1} \begin{bmatrix} \mathbf{r}_{\mathrm{xy}} \\ \mathbf{r}_{\mathrm{xx}} \end{bmatrix} \tag{4.1}$$

and the inverse is calculated:

$$\begin{bmatrix} \mathbf{g} \\ \boldsymbol{\sigma}_{\mathrm{n}} \end{bmatrix} = \begin{bmatrix} \mathbf{S}^{-1} & \mathbf{0} \\ \mathbf{0} & \mathbf{S}^{-1} \end{bmatrix} \begin{bmatrix} \mathbf{I} & -\mathrm{diag}\left(\mathbf{w}\right) \\ -\mathrm{diag}\left(\mathrm{vecdiag}\left(\boldsymbol{\Sigma}_{\mathrm{s}}\mathbf{G}^{H}\right)\right) & \mathrm{diag}\left(\boldsymbol{\Sigma}_{\mathrm{s}}\mathbf{G}^{H}\mathbf{w}\right) \end{bmatrix} \begin{bmatrix} \mathbf{r}_{\mathrm{xy}} \\ \mathbf{r}_{\mathrm{xx}} \end{bmatrix} \tag{4.2}$$

where

$$\mathbf{S} = \mathrm{diag}(\boldsymbol{\Sigma}_{s}\mathbf{G}^{H}\mathbf{w}) - \mathrm{diag}(\mathbf{w})\mathrm{diag}\left(\mathrm{vecdiag}(\boldsymbol{\Sigma}_{s}\mathbf{G}^{H})\right). \tag{4.3}$$

Equation 4.2 is now in the form of (3.19). Note that this expression is derived using the well-known inverse of a 2-by-2 matrix. This works because all blocks in $\mathbf{A}$ are diagonal matrices and therefore are commuting matrices. This produces the following expression for the $P \times 1$ gain estimate vector $\mathbf{g}$:

$$\mathbf{g} = \mathbf{S}^{-1}\left(\mathbf{r}_{\mathrm{xy}} - \mathrm{diag}(\mathbf{w})\mathbf{r}_{\mathrm{xx}}\right). \tag{4.4}$$

Next, the measured correlations $\mathbf{r}_{\mathrm{xy}}$ and $\mathbf{r}_{\mathrm{xx}}$ as defined by (3.13) and (3.15) respectively are substituted:

$$\begin{aligned} \mathbf{g} = \mathbf{S}^{-1}\Big(&(\tilde{\mathbf{G}}\tilde{\boldsymbol{\Sigma}}_{\mathrm{s}}\tilde{\mathbf{G}}^{H}\mathbf{w} + \tilde{\boldsymbol{\Sigma}}_{\mathrm{n}}\mathbf{w}) \\ &- \mathrm{diag}(\mathbf{w})\left(\mathrm{vecdiag}\left(\tilde{\mathbf{G}}\tilde{\boldsymbol{\Sigma}}_{\mathrm{s}}\tilde{\mathbf{G}}^{H}\right) + \tilde{\boldsymbol{\sigma}}_{\mathrm{n}}\right)\Big), \end{aligned} \tag{4.5}$$

where $\tilde{\mathbf{G}}$ is the diagonal matrix containing the true gains, $\tilde{\boldsymbol{\Sigma}}_{\mathrm{s}}$, and $\tilde{\boldsymbol{\Sigma}}_{\mathrm{n}}$ are the measured signal and noise covariance matrices and $\tilde{\boldsymbol{\sigma}}_{\mathrm{n}}$ is a vector containing the true noise powers.

Using this expression, the response of the system to noise and interference can be mathematically analysed. However, the response of the system without noise or interference will first be determined, so the noise terms are set to zero and it is assumed that the FoV contains only the calibration source:

$$\begin{aligned} \mathbf{g} &= \mathbf{S}^{-1}\left((\tilde{\mathbf{G}}\tilde{\boldsymbol{\Sigma}}_{\mathrm{s}}\tilde{\mathbf{G}}^{H}\mathbf{w}) - \mathrm{diag}(\mathbf{w})\mathrm{vecdiag}(\tilde{\mathbf{G}}\tilde{\boldsymbol{\Sigma}}_{\mathrm{s}}\tilde{\mathbf{G}}^{H})\right), \\ &= \mathbf{S}^{-1}\tilde{\mathbf{G}}\left((\tilde{\boldsymbol{\Sigma}}_{\mathrm{s}}\tilde{\mathbf{G}}^{H}\mathbf{w}) - \mathrm{diag}(\mathbf{w})\mathrm{vecdiag}(\tilde{\boldsymbol{\Sigma}}_{\mathrm{s}}\tilde{\mathbf{G}}^{H})\right). \end{aligned} \tag{4.6}$$

where $\tilde{\boldsymbol{\Sigma}}_{\mathrm{s}} = \boldsymbol{\Sigma}_{\mathrm{c}} = \sigma_{c}\mathbf{1}\mathbf{1}^{H}$. If $\mathbf{w} \approx 1 \oslash \tilde{\mathbf{g}}^{H}$, i.e., it is assumed that the current best estimate of $\mathbf{g}$ is close to its true value, then (4.3) becomes:

$$\mathbf{S} \approx P\sigma_{c}\mathbf{I} - \sigma_{c}\mathbf{I} = (P-1)\sigma_{c}\mathbf{I}. \tag{4.7}$$

Equation (4.6) then becomes:

$$\mathbf{g} \approx \mathbf{S}^{-1}\tilde{\mathbf{G}}(P\sigma_c\mathbf{1} - \sigma_c\mathbf{1}) = \tilde{\mathbf{g}}, \tag{4.8}$$

which shows that $\mathbf{g}$ will be equal to the true gains when (4.6) converges and there is no noise or interference present in the measurements. This is a significant improvement on the basic SH formulation where it was determined that the true gains will never be estimated exactly even if the conditions are ideal.

To analyse the effects of interference, the source covariance matrix is expanded to be a superposition of the covariance matrices for the calibration source and interferers, i.e., $\tilde{\mathbf{\Sigma}}_\mathrm{s} = \mathbf{\Sigma}_\mathrm{c} + \mathbf{\Sigma}_\mathrm{int}$. Substituting this into (4.6) gives:

$$\mathbf{g} = \mathbf{S}^{-1}((\tilde{\mathbf{G}}(\mathbf{\Sigma}_\mathrm{c} + \mathbf{\Sigma}_\mathrm{int})\tilde{\mathbf{G}}^H\mathbf{w}) - \mathrm{diag}(\mathbf{w})\mathrm{vecdiag}(\tilde{\mathbf{G}}(\mathbf{\Sigma}_\mathrm{c} + \mathbf{\Sigma}_\mathrm{int})\tilde{\mathbf{G}}^H)). \tag{4.9}$$

Multiplying out and grouping related terms gives:

$$\begin{aligned} \mathbf{g} &= \mathbf{S}^{-1}\tilde{\mathbf{G}}(\mathbf{\Sigma}_\mathrm{c}\tilde{\mathbf{G}}^H\mathbf{w} - \mathrm{diag}(\mathbf{w})\mathrm{vecdiag}(\mathbf{\Sigma}_\mathrm{c}\tilde{\mathbf{G}}^H) \\ &\quad +\mathbf{\Sigma}_\mathrm{int}\tilde{\mathbf{G}}^H\mathbf{w} - \mathrm{diag}(\mathbf{w})\mathrm{vecdiag}(\mathbf{\Sigma}_\mathrm{int}\tilde{\mathbf{G}}^H)). \end{aligned} \tag{4.10}$$

As demonstrated by (4.8), the terms on the first row will give the correct gain values. The terms on the second row represent the error caused by the presence of the interfering sources, a systematic error that will be labelled as $\Delta\mathbf{g}$. The relative errors $\Delta\mathbf{g} \oslash \mathbf{g}$, are related to the SIR as:

$$\begin{aligned} \Delta\mathbf{g} \oslash \mathbf{g} &= \left|\left(\mathbf{\Sigma}_\mathrm{int}\tilde{\mathbf{G}}^H\mathbf{w} - \mathrm{diag}(\mathbf{w})\mathrm{vecdiag}(\mathbf{\Sigma}_\mathrm{int}\tilde{\mathbf{G}}^H)\right)\right| \oslash \\ &\quad \left|\left(\mathbf{\Sigma}_\mathrm{c}\tilde{\mathbf{G}}^H\mathbf{w} - \mathrm{diag}(\mathbf{w})\mathrm{vecdiag}(\mathbf{\Sigma}_\mathrm{c}\tilde{\mathbf{G}}^H)\right)\right| \\ &= \mathbf{1} \oslash \mathrm{SIR}, \end{aligned} \tag{4.11}$$

where $\oslash$ denotes element-wise division, which indicates that the SIR and, hence, the calibration error, may vary across the array depending on the array and source geometry. If the current best gain estimate is close to its true value, then the expression for the SIR can be reduced to:

$$\mathrm{SIR} \approx \left|(\mathbf{\Sigma}_\mathrm{c}\mathbf{1} - \mathrm{vecdiag}(\mathbf{\Sigma}_\mathrm{c}))\right| \oslash \left|(\mathbf{\Sigma}_\mathrm{int}\mathbf{1} - \mathrm{vecdiag}(\mathbf{\Sigma}_\mathrm{int}))\right|. \tag{4.12}$$

The numerator can be further simplified to:

$$\begin{aligned} \mathbf{\Sigma}_\mathrm{c}\mathbf{1} - \mathrm{vecdiag}(\mathbf{\Sigma}_\mathrm{c}) &= \sigma_\mathrm{c}\mathbf{1}\mathbf{1}^H\mathbf{1} - \sigma_\mathrm{c}\mathrm{vecdiag}(\mathbf{1}\mathbf{1}^H) \\ &= \sigma_\mathrm{c}(P-1)\mathbf{1}, \end{aligned} \tag{4.13}$$

With $\mathbf{\Sigma}_\mathrm{int} = \sum_i \sigma_i\mathbf{a}_i\mathbf{a}_i^H\mathbf{1}$, where $\mathbf{a}_i$ is a $P \times 1$ column vector containing the geometric delays of interferer $i$ at each receiving element, the denominator of (4.12) can be written as

$$\mathbf{\Sigma}_\mathrm{int}\mathbf{1} - \mathrm{vecdiag}(\Sigma_\mathrm{int}) = \sum_i \sigma_i(\mathbf{a}_i(\mathbf{a}_i^H\mathbf{1}) - \mathbf{1}). \tag{4.14}$$

Substituting these results into (4.12) gives

$$\text{SIR} = \sigma_{\text{c}}(P-1)\mathbf{1} \oslash \left| \sum_i \sigma_i(\mathbf{a}_i(\mathbf{a}_i^H\mathbf{1}) - \mathbf{1}) \right|, \tag{4.15}$$

which gives an analytical expression from which the SIR can be calculated for a given interferer distribution. Note that the SIR as defined here is a vector presenting the SIR per element. In the simulations below, it was found that the SIR variations across the array were reasonably small, so a single SIR value is introduced by dividing the average value of the numerator by the average value of the denominator.

## 4.3 The impact of noise

The impact of noise on the quality of the gain estimates is analysed by re-arranging the terms in (4.5) such that the noise-related terms are grouped together:

$$\begin{aligned} \mathbf{g} &= \mathbf{S}^{-1}\Big(\tilde{\mathbf{G}}\Big((\boldsymbol{\Sigma}_{\text{c}}\tilde{\mathbf{G}}^H\mathbf{w}) - \text{diag}(\mathbf{w})\text{vecdiag}(\tilde{\mathbf{G}}\boldsymbol{\Sigma}_{\text{c}}\tilde{\mathbf{G}}^H)\Big) \\ &\quad + \boldsymbol{\Sigma}_{\text{n}}\mathbf{w} - \text{diag}(\mathbf{w})\boldsymbol{\sigma}_{\text{n}}\Big). \end{aligned} \tag{4.16}$$

From inspection it is seen that the noise-related terms will cancel if they are equal, resulting in the ideal scenario as described by (4.8). Spatially white noise is therefore not expected to bias the results.

However, they will only be equal if the off-diagonal entries of $\boldsymbol{\Sigma}_{\text{n}}$ are zero, which implies that there is zero crosscorrelation in the noise signals. It is reasonable to assume that the noise signals themselves are uncorrelated between the elements, meaning that the amplitude of the noise crosscorrelations will approach zero when integrating for a long time. However, practically, a finite correlation in the noise will exist due to noise coupling between the elements [64], [65]. The level of noise coupling depends, a.o., on the spacing of the elements. To quantify the impact of non-zero cross-correlations between the noise signals of the receiving elements, an SNR expression is defined that is similar to (4.12):

$$\text{SNR} \approx |(\boldsymbol{\Sigma}_{\text{c}}\mathbf{1} - \text{vecdiag}(\boldsymbol{\Sigma}_{\text{c}}))| \oslash |(\boldsymbol{\Sigma}_{\text{n}}\mathbf{1} - \text{vecdiag}(\boldsymbol{\Sigma}_{\text{n}}))|. \tag{4.17}$$

## 4.4 Simulations

### 4.4.1 The scene

For the simulation analysis in this section, the strong sidelobe response of a dense regular array configuration is specifically exploited to highlight the

effects of interference. A comparison with a random array configuration is ultimately shown in the concluding result to prove that the analysis in this section holds for any array configuration.

A uniform rectangular array of identical antennas with half-wavelength spacing is considered. The array has a uniform amplitude distribution with zero phase shift between the elements resulting in a station beam pointed at boresight, where the calibration source is also located. The array has 576 elements which are 24 elements on a side for a square layout.

The antennas in the array will experience mutual coupling to an extent that is dependent on the inter-element spacing. This will lead to distortions in the embedded element patterns (EEPs) that can potentially cause systematic errors in the calibration solutions [66]. In [56] a study was done to determine the severity of this impact in large distributed arrays. It was concluded that the assumption of an average EEP will generally not cause unacceptable degradation of the system performance in most scenarios. For the array considered in this simulation, it is reasonable to assume that the mutual coupling effects are equal across the array and that the embedded element patterns can be approximated accurately by a single pattern. A simulated dipole radiation pattern was chosen as the approximation in this simulation scenario. However, the aim of this study and its conclusions are not dependent on the specific choice of EEP. The use of a non-isotropic EEP was merely chosen to highlight the effect it has on the performance of SH.

Large arrays are often subdivided into subarrays, referred to as *tiles*, to lower the digitisation load. The beam pattern of a tile varies with its size which subsequently affects the crosscorrelations as defined by (3.13). It is therefore of practical interest to study the impact of tile size which, in this study, is done by controlling the number of elements $M$ a tile has on a side. As the focus of this study is on the digital beamforming stage of the array, it is assumed that the tile beamformer (analogue or digital) is already calibrated and provides sufficient pointing accuracy for the application of SH.

The scene consists of a calibration source and a single interfering source, with a spatial distribution as shown in Figure 4.1. The calibration source is indicated by the green star and the interfering source by the black star. The signals of both sources are modelled as mutually uncorrelated random noise. The output of each receiving element is calculated by combining each signal with the appropriate geometric delay for that element. These outputs are then multiplied with the true gains which are modelled as $g_p = 1 + CN(0, 0.1)$, i.e., as zero-mean Gaussian noise on the real and imaginary part with a standard deviation of 0.1 added to a nominal value of unity.

The impact of interference and noise will be studied first. This will be followed by a study in which SH is optimised by mitigating interference using null-placement.

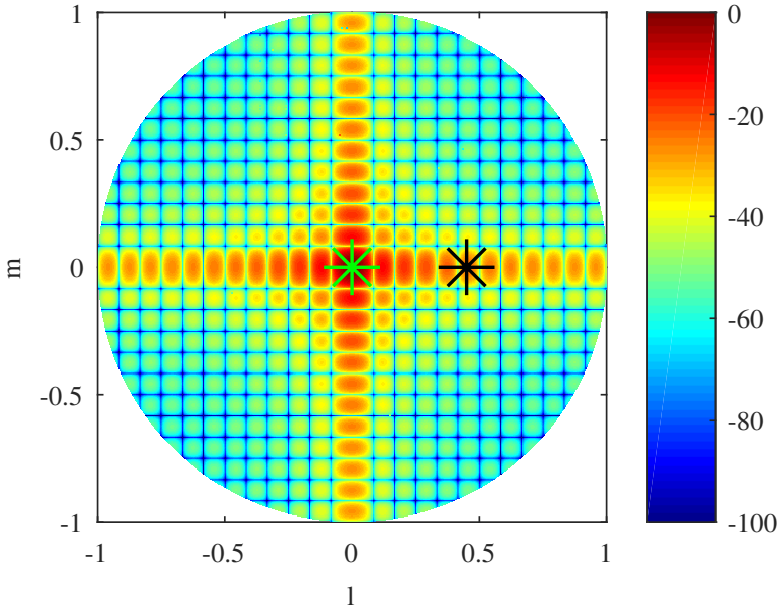


**Figure 4.1:** Positions of the two sources overlaid on top of the radiation pattern of the array. The calibration source and interferer are indicated by the green and black stars respectively. The scale is normalised and in dB.

### 4.4.2 Interference and noise

The level of apparent interfering power is varied by tuning the boresight angle of the interfering source while keeping its azimuthal angle constant. The boresight angle is varied in 1-degree steps between 10 and 85 degrees, chosen such that the interferer is outside the main beam and above the horizon. The combination of the embedded element pattern and array pattern provides different attenuation levels over this range allowing the calibration performance to be explored for a wide range of interfering power levels. Furthermore, the power of the interferer is set to twice that of the calibration source to highlight its impact. While stepping through the interferer boresight angles, the impact of measurement noise is simultaneously investigated by varying the instantaneous SNR at element level from -40 to -18 dB. The results of this simulation are shown in Figure 4.2. The results show that the interfering source causes a bias in the estimates while a closer inspection shows that the SNR determines the noise on the estimates. Below, the effects of both will be studied separately.

#### Interference only

Figure 4.3 shows the mean gain error in magnitude and phase for different tile sizes as a function of interferer boresight angle and for a signal measurement that is free of noise. Also, to isolate the effects of interference entirely, it is assumed that the measurements are integrated for a very long time by using the expected value of the measured correlations. It is seen that the error

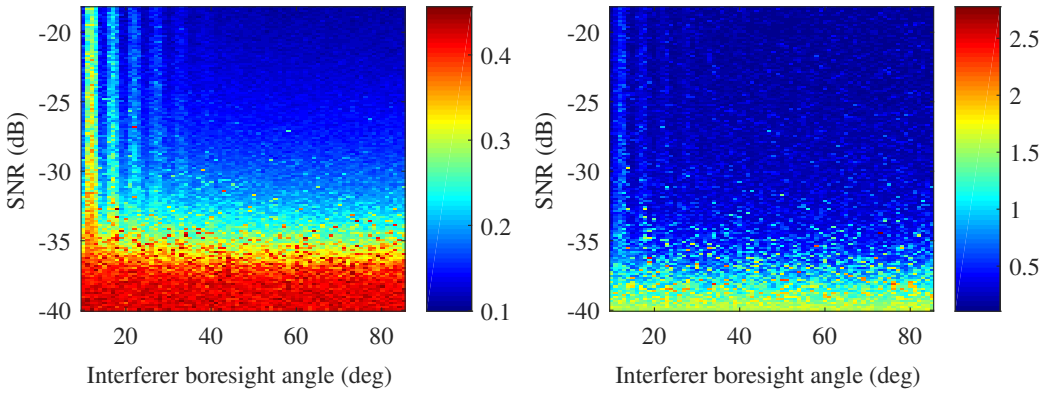


**Figure 4.2:** Relative error in magnitude (left) and phase error (right, in radian) as a function of instantaneous SNR at element level and interferer boresight angle.

resembles the sidelobe pattern of the array and that the error lowers as the tile size increases. This can be explained by the auto- and crosscorrelation magnitudes of the interferer, i.e., $|\mathbf{r}_{\text{xy}}^{\text{int}}| = \mathbf{\Sigma}_{\text{int}}\mathbf{1}$ and $|\mathbf{r}_{\text{xx}}^{\text{int}}| = \text{diag}(\mathbf{\Sigma}_{\text{int}})$, which are plotted in Figure 4.4 as a function of interferer boresight angle and tile size. It is seen that the mean $|\mathbf{r}_{\text{xy}}^{\text{int}}|$ resembles the sidelobe pattern of the array which is simply a result of the interferer moving through the sidelobes of the array. The mean $|\mathbf{r}_{\text{xx}}^{\text{int}}|$ resembles the tile pattern in the same way. Since $|\mathbf{r}_{\text{xy}}^{\text{int}}|$ is codependent on the station and tile pattern, of which the latter becomes more directive with an increase in tile size, better gain estimation performance is observed for larger tiles. Figure 4.5 summarises these results by showing the gain errors plotted in Figure 4.3 versus SIR as defined in (4.15). Note that the results for the different tile sizes correspond fairly well, which shows that the assumption in using average values in the SIR definition is reasonable. The results for a random array layout are additionally shown in Figure 4.5. The regular and random array layout results correspond fairly well which further confirms the suitability of using average values in the SIR calculation. The results in Figures 4.3, 4.4 and 4.5 suggest using larger tiles, which provide better isolation of the calibration source. However, larger tiles limit the scan range. The alternative is to increase the array size to increase the directivity of the array pattern, which, as shown above, also dictates the performance.

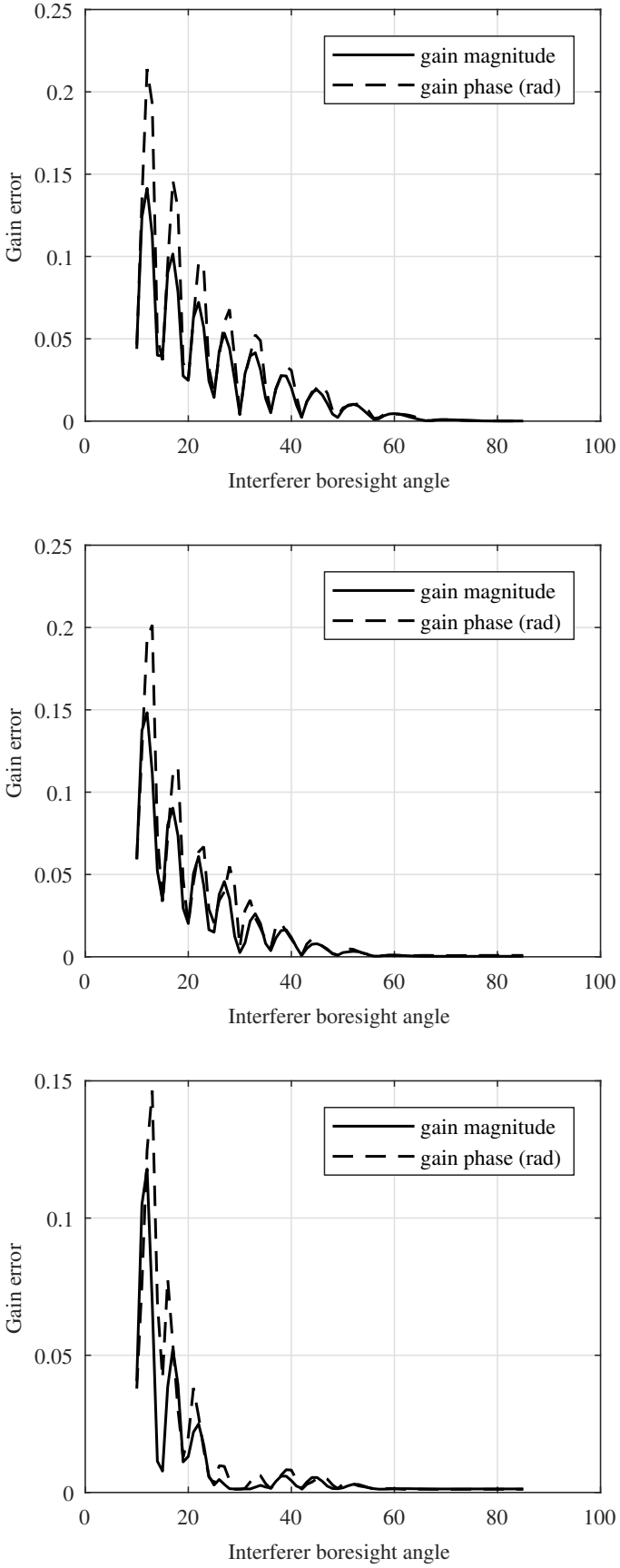


**Figure 4.3:** Mean gain error as a function of interferer boresight angle for $M = 1$ (top), $M = 2$ (middle) and $M = 4$ (bottom).

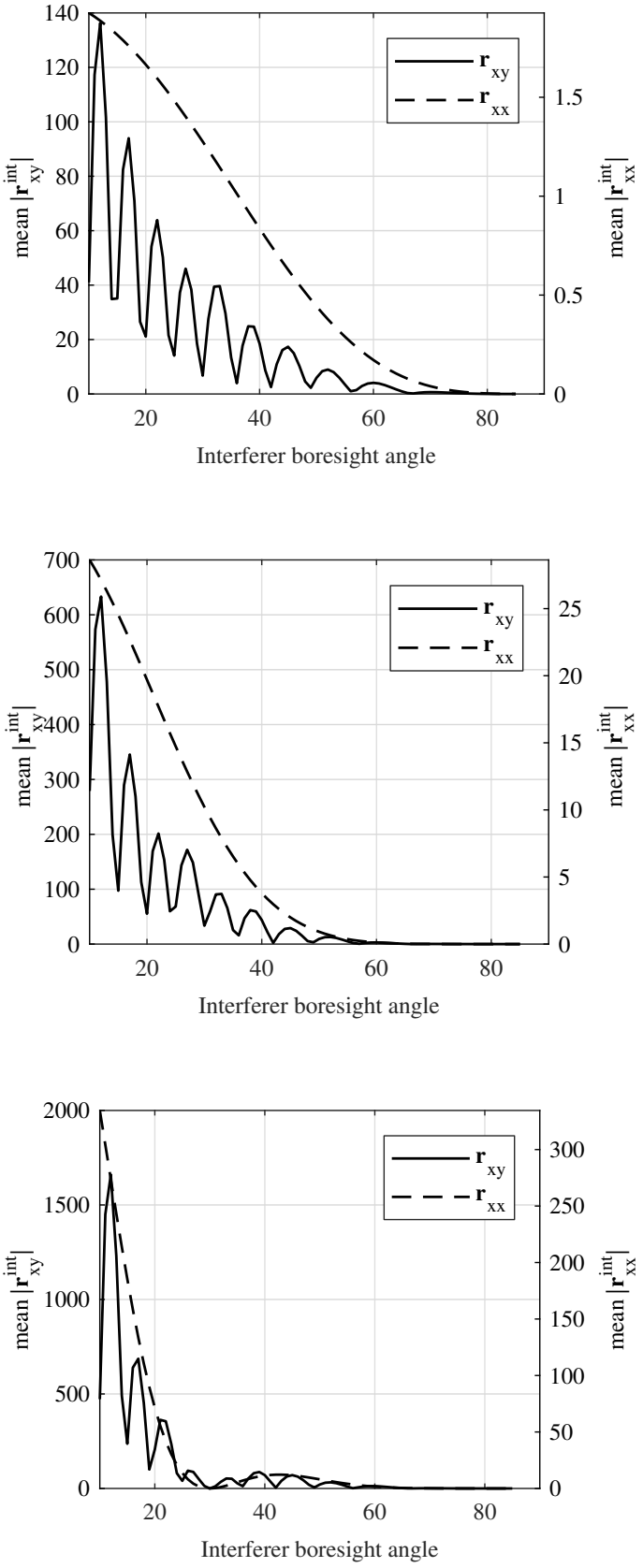


**Figure 4.4:** Mean $|\mathbf{r}_{\mathrm{xy}}^{\mathrm{int}}|$ and $|\mathbf{r}_{\mathrm{xx}}^{\mathrm{int}}|$ as a function of interferer boresight angle for $M = 1$ (top), $M = 2$ (middle) and $M = 4$ (bottom).

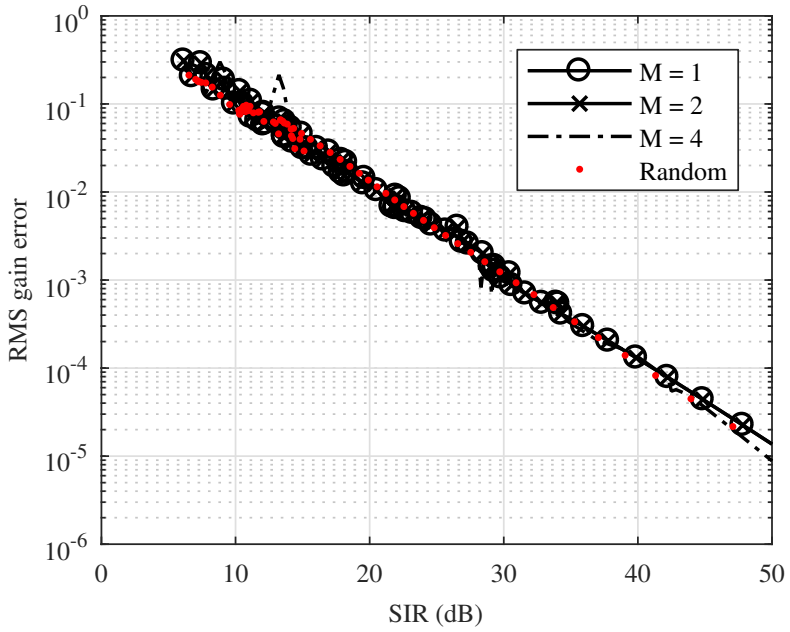


**Figure 4.5:** RMS gain error as a function of SIR and tile size (M). The RMS gain error for a random array configuration is also shown.

### Noise only

In Section 4.3, it was shown that system noise will have no impact on the performance if the crosscorrelation terms of the noise covariance matrix are zero. While the noise signals themselves are expected to be mutually uncorrelated, the crosscorrelations will only approach zero when integrating long enough. Additionally, noise coupling will exist between elements located close together [65]. Since any practical array is limited to finite integration time and could have a dense configuration, it is necessary to study the impact of noise more closely. Figure 4.6 shows the RMS gain error as a function of instantaneous SNR at element level for different signal lengths ($N$) and no interference. It is seen that the error lowers as the instantaneous SNR improves. It is also seen that, below a certain SNR, the error reaches a maximum. The gains are solved iteratively, where, after each iteration, the reference beam weights are updated with the latest gain estimates. The gains are derived from the measured correlations, which contain the noise, so after the first iteration, the reference beam weights are updated with noisy estimates that subsequently distort the array beam. This process repeats until the array beam is entirely distorted resulting in gain estimates that are simply just noise. As the gain amplitudes are normalised while the gain phases cannot get further randomised than a uniform distribution between 0 and $2\pi$, the errors do not grow indefinitely but taper off. As expected, the point at which this happens also depends on the integration time as shown in Fig. 4.6. In Fig. 4.7, the RMS gain error is shown

as a function of SNR calculated using (4.17). This result is useful when the noise covariance matrix is known for a measured dataset.

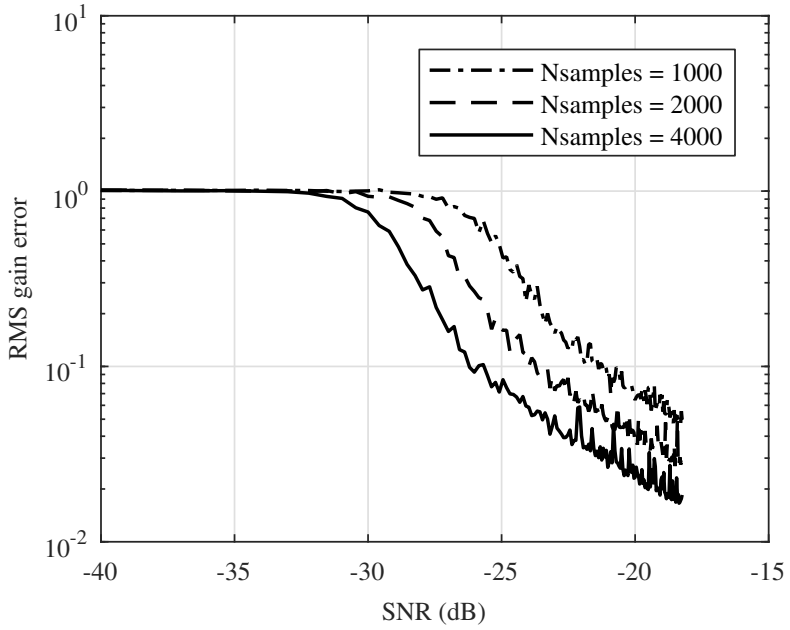


**Figure 4.6:** RMS gain error as a function of instantaneous SNR at element level and number of time samples (Nsamples).

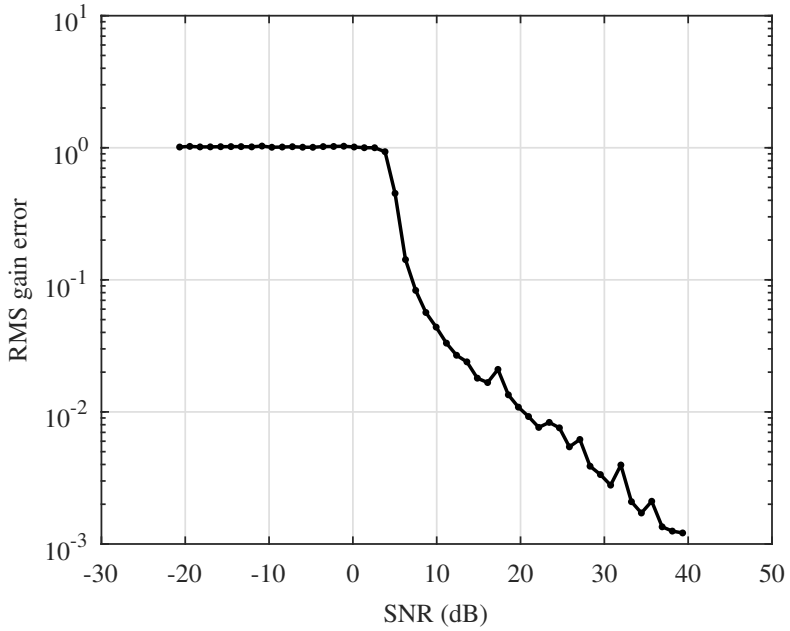


**Figure 4.7:** RMS gain error as a function of SNR calculated using (4.17).

### 4.4.3 Mitigation of interference using null placement

It was determined that interference will have a detrimental effect on the accuracy of the gain estimates when using SH. In reality, multiple interfering sources will typically be present. Depending on the extent of the contribution to the SIR, placement of multiple nulls could be necessary. However, to highlight the residual effects of nulling when using SH, this study is limited to a single interferer as depicted in Fig. 4.1.

An all-digital ($M$=1) configuration is assumed when investigating the following two scenarios:

1. The boresight angle of the interferer is varied between 10 and 85 degrees while the power of the interferer is constant and equal to the power of the calibration source.

2. The boresight angle of the interferer matches the first sidelobe of the array and its power is varied.

In both cases, a null is placed at the location of the interferer. The null is applied by multiplying the antenna signals with the appropriate weights that are calculated as:

$$\mathbf{w}_{\text{null}} = \mathbf{a}_{\text{c}} - \mathbf{a}_{\text{i}} \frac{\mathbf{a}_{\text{i}}^H \mathbf{a}_{\text{c}}}{\mathbf{a}_{\text{i}}^H \mathbf{a}_{\text{i}}}, \tag{4.18}$$

where $\mathbf{a}_{\text{c}}$ and $\mathbf{a}_{\text{i}}$ are $P \times 1$ vectors containing the geometric delay phasors of the antennas towards the calibration and interfering source respectively. This changes (3.11) to $\mathbf{y} = \mathbf{w}_{\text{null}}^H \mathbf{X}$.

#### Scenario 1: interferer with variable position

Figure 4.8 shows a comparison of the mean magnitude and phase error of the gain estimates as a function of interferer boresight angle with nulling enabled and disabled.

When nulling is disabled, it is seen that the mean error follows the sidelobe pattern of the array. This is expected since, as explained earlier, the estimation error is directly proportional to the level of interference. Without nulling, the level of interference is mainly influenced by the sidelobe pattern of the array, which is a combination of the array factor and the average embedded element pattern (EEP).

With nulling enabled, it is seen that the mean error decreases as the interferer boresight angle increases. However, the level of error is similar to the level achieved in the nulls of the sidelobe pattern. This is an intuitive result as, at those locations, the interfering source is nulled even without nulling that direction specifically. The error curve also indicates that the result is non-zero. This is caused by the fact that the total power detected on the autocorrelations of the element signals is still the sum of the power of the two sources

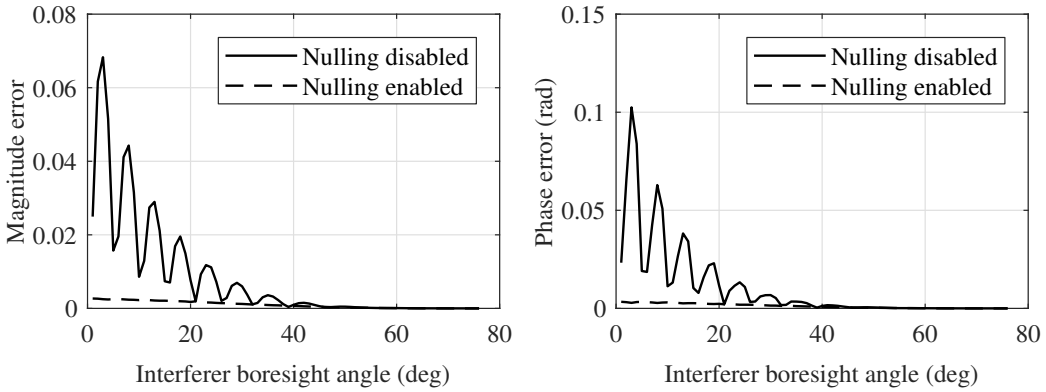


**Figure 4.8:** Error in magnitude (left) and phase (right) as a function of interferer boresight angle.

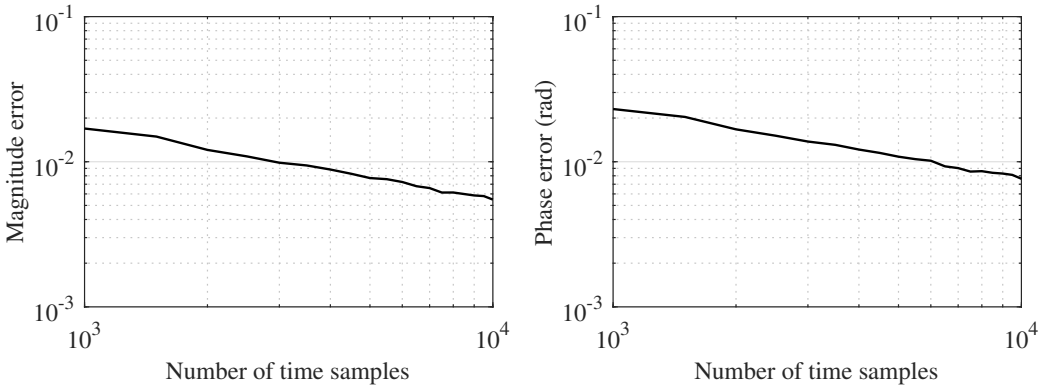


**Figure 4.9:** Error in magnitude (left) and phase (right) as a function of signal length when an interferer is located at 10 degrees.

as detected by the individual elements in the array. As our simulations are based on a finite-length time series based on noise-like signals, this causes a self-noise effect [67]. As the power picked up from the interfering source is directly proportional to the embedded element patterns (EEPs) of the array, the mean error level gradually decreases to zero as the boresight angle increases.

Since the remaining error with nulling is caused by self-noise, it is expected that the remaining error will decrease as the signal length increases. Figure 4.9 shows the estimation error as a function of signal length when an interferer is located at 10 degrees. This confirms our conjecture.

### Scenario 2: interferer with variable power

Figure 4.10 show a comparison of the mean magnitude and phase error of the gain estimates as a function of the SIR calculated using (4.12).

With nulling disabled, a steady increase in gain error is observed as a function of decreasing SIR up until a discontinuity is encountered. Separate analysis showed that this is the point where the calibration procedure switches

to the interferer because of its dominant power. As expected, the gain error then continues to lower as the interfering power increases as it is now effectively the calibration source. When the power of the interferer is increased further, calibration with nulling enabled also breaks down. However, the null remains effective in cancelling the effects of the interferer for a very wide range of interfering power before the breakdown point.

A detailed analysis in which the length of the time series and the magnitudes of the gain errors were varied, indicated that this is due to a combination of self-noise and beam errors at the start of the calibration iterations. The beam errors limit the suppression of the interferer while the self-noise restricts the achievable calibration accuracy in the first iteration of the calibration loop. As consecutive iterations are based on exactly the same time series, i.e., no new measurement is simulated, the iterations lock-in to an erroneous solution.

Figure 4.11 (left) shows a comparison of the phase estimation error of all the antennas per iteration for SIR values of 0 dB and -20 dB. Notice the difference in convergence in the first few iterations between the two scenarios. The gains are estimated from the measured correlations (of which the phase is dominated by the strongest source), so as the nulling starts to break down, the phase of the estimated gains change to the geometric phase delays of the interferer. The reference beam is then beamformed towards the interferer as the reference beam weights are being updated after each solving iteration. This is demonstrated by Figure 4.11 (right) which shows the reference beam magnitude towards the interferer for high and low SIR values, as a function of iteration. It is seen that the magnitude quickly approaches the nominal magnitude when the SIR is low, indicating that the reference beam is forming a maximum towards the interferer. This finding is further supported by the results in Figures 4.12 and 4.13. Figure 4.12 shows the reference beam magnitude towards the calibrator and interferer vs SIR and Figure 4.13 shows the SIR of the array output signal vs the SIR of the incident signal. The discontinuities correspond with those in Figure 4.10 which confirms the transitions between the calibrator and interferer.

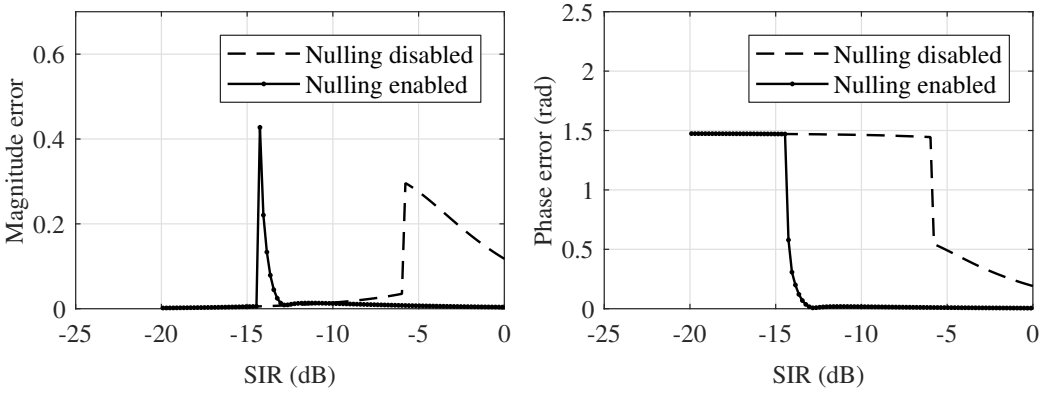


**Figure 4.10:** Error in magnitude (left) and phase (right) as a function of SIR.

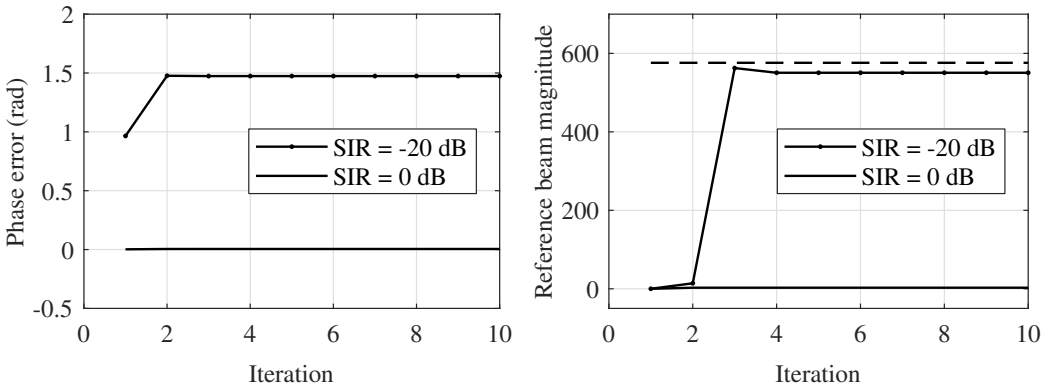


**Figure 4.11:** Left: mean phase error of all the antennas versus solving iteration for high and low SIR. Right: Magnitude of the reference beam towards the interferer versus solving iteration for high and low SIR. The reference beam magnitude when beamformed to broadside is indicated by the dashed line.

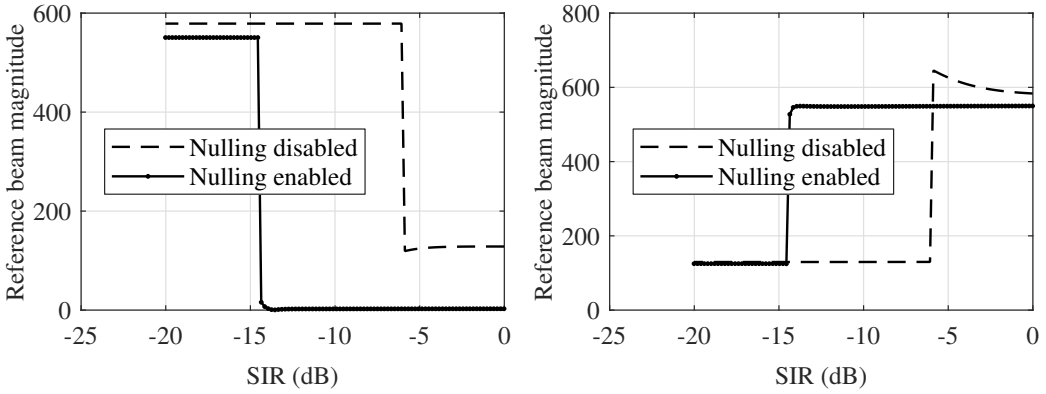


**Figure 4.12:** Reference beam magnitude towards interferer (left) and calibrator (right) vs SIR with nulling enabled and disabled.

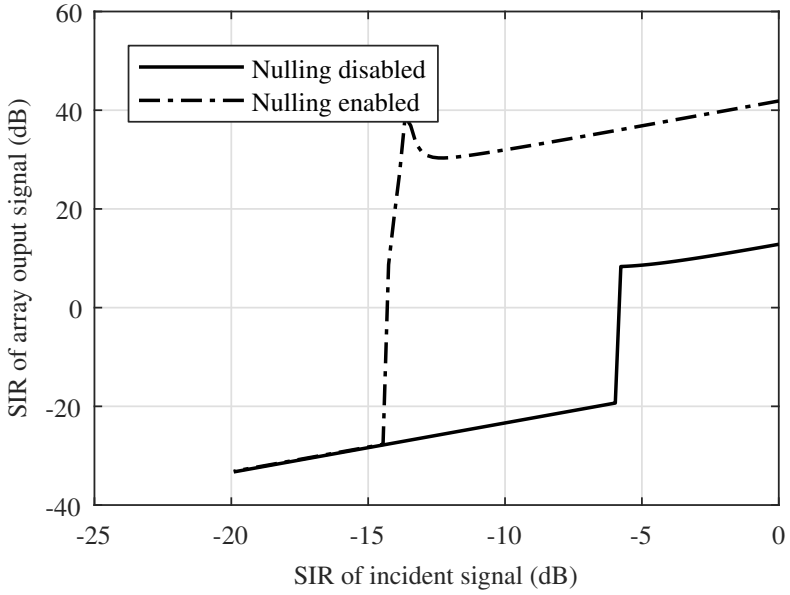


**Figure 4.13:** SIR of array output signal versus SIR of incident signal.

## 4.5 Applications

### 4.5.1 LOFAR subarray

A LOFAR station (or subarray) consists of two separate receiver systems to effectively cover the 10-250 MHz frequency band. These receivers are called the low-band antenna (LBA) station and the high-band antenna (HBA) station. Below is a calibration study on real measurements made with these instruments. First, a very brief introduction on both systems is given.

#### Low-band antenna

An LBA station consists of 96 antennas in a random configuration and is designed to cover the 10-90 MHz frequency range. The frequency range is subdivided into 512 subbands where each subband is integrated over 1-s time intervals. The EEPs of the central elements in the array are significantly distorted due to mutual coupling, so for this example, only the outer 48 antennas of station CS302 are used. The array layout of these antennas is shown in Figure 4.14 top.

#### High-band antenna

An HBA station consists of 48 (Dutch stations) or 96 tiles (European stations) in a regular configuration as shown in Figure 4.14 (bottom) for the station DE601 in Germany. Each tile has 16 antennas placed in a regular square

configuration with an inter-element spacing of 1.25 m. It is designed to cover the 110-250 MHz frequency range. The frequency range is subdivided into 512 subbands where each subband is integrated over 1 s.

### Estimating the SIR from the measured data

The expected performance of SH in each dataset can accurately be determined by calculating the SIR using (4.12) for the measured datasets. To do that it is necessary to extract $\mathbf{\Sigma}_{\mathrm{c}}$ and $\mathbf{\Sigma}_{\mathrm{int}}$ from the measured covariance matrix $\mathbf{\Sigma}_{\mathrm{meas}}$ which can be modelled as:

$$\mathbf{\Sigma}_{\mathrm{meas}} = \mathbf{\Sigma}_{\mathrm{s}} + \mathbf{\Sigma}_{\mathrm{n}}, \tag{4.19}$$

where $\mathbf{\Sigma}_{\mathrm{s}}$ and $\mathbf{\Sigma}_{\mathrm{n}}$ are the covariance matrices for the sky signals and system noise respectively. First, it is assumed that $\mathbf{\Sigma}_{\mathrm{n}}$ is diagonal and the dominant contributor to the diagonal entries of $\mathbf{\Sigma}_{\mathrm{meas}}$, i.e., $\mathrm{diag}(\mathbf{\Sigma}_{\mathrm{meas}}) \approx \mathbf{\Sigma}_{\mathrm{n}}$. So to isolate the sky-signal space, the diagonal entries of $\mathbf{\Sigma}_{\mathrm{meas}}$ are set to zero. However, in reality, the diagonal entries also contain power received from the sky, which is now removed as well. This will result in some of the eigenvalues of $\mathbf{\Sigma}_{\mathrm{s}}$ to be negative. This can be corrected by increasing the eigenvalues such that the smallest eigenvalue becomes zero and subsequently reconstructing the matrix using:

$$\mathbf{\Sigma}_{\mathrm{s}} = \mathbf{V}_{\mathrm{s}}\mathbf{\Lambda}_{\mathrm{s}}\mathbf{V}_{\mathrm{s}}^{H}, \tag{4.20}$$

where $\mathbf{V}_{\mathrm{s}}$ is a P×P matrix containing the eigenvectors and $\mathbf{\Lambda}_{\mathrm{s}}$ is the P×P diagonal matrix containing the eigenvalues of $\mathbf{\Sigma}_{\mathrm{s}}$. To isolate the contribution from the interference, $\mathbf{\Sigma}_{\mathrm{s}}$ is decomposed as:

$$\mathbf{\Sigma}_{\mathrm{s}} = \mathbf{\Sigma}_{\mathrm{c}} + \mathbf{\Sigma}_{\mathrm{int}}, \tag{4.21}$$

where $\mathbf{\Sigma}_{\mathrm{c}}$ and $\mathbf{\Sigma}_{\mathrm{int}}$ are the covariance matrices of the calibration source and interferers respectively. Using accurate knowledge of the apparent power and position of the calibration source in each example, $\mathbf{\Sigma}_{\mathrm{c}}$ can be calculated as:

$$\mathbf{\Sigma}_{\mathrm{c}} = \sigma_{\mathrm{c}}\mathbf{a}_{\mathrm{c}}\mathbf{a}_{\mathrm{c}}^{H}, \tag{4.22}$$

where $\mathbf{a}_{\mathrm{c}}$ is a vector containing the geometric delay phasors of the calibration source and $\sigma_{\mathrm{c}}$ is its apparent power. Finally, the covariance matrix for the interferers can be calculated as:

$$\mathbf{\Sigma}_{\mathrm{int}} = \mathbf{\Sigma}_{\mathrm{s}} - \sigma_{\mathrm{c}}\mathbf{a}_{\mathrm{c}}\mathbf{a}_{\mathrm{c}}^{H}. \tag{4.23}$$

### Results: LBA

Three measured datasets at 43.5 MHz corresponding to altitude angles ($\theta_{\mathrm{alt}}$) for Cassiopeia A (Cas A) of 84°, 46° and 26° were considered. All three measurements were taken on 20 November 2018. The latter dataset was chosen to

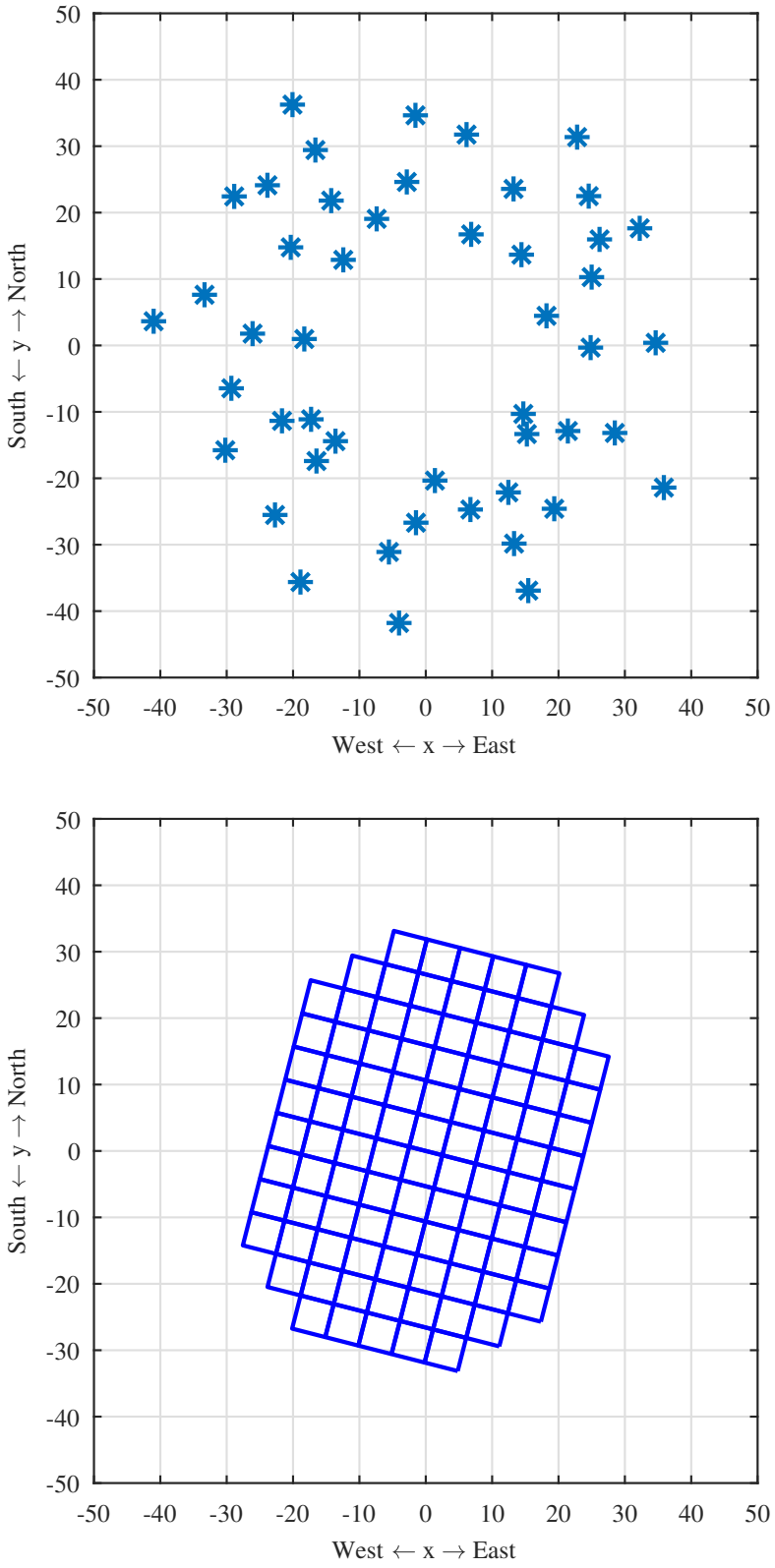


**Figure 4.14:** LOFAR subarray antenna layouts. The positions of the LBA's used for our experiment are shown at the top and the positions of the HBA tiles used for our experiment are shown at the bottom.

represent an extreme scenario. When selecting Cassiopeia A as the calibration source, the SIR's for these datasets were estimated as 14.6, 9.8 and 5 dB in the order of the altitude angles mentioned above. For maximum accuracy, the measured datasets were calibrated before calculating the SIR. Based on these estimates alone and the results in Fig. 4.5, it is already expected that SH will produce gain estimates that are suitable for calibrating these datasets. Specifically, the RMS gain errors for SIR's of 14.6, 9.8 and 5 dB correspond to beamformer efficiencies of approximately 99.9, 99.6 and 96% according to (2.39).

Comparisons between the calibrated and uncalibrated imaged visibilities are shown in Fig. 4.15. All three datasets show improved images after SH calibration has been applied. The noise has been reduced significantly and the main beam of the array is apparent. The corresponding gain phase estimation results are shown in Fig. 4.16. The gain solutions differ between the measurements, which is expected based on the time dependence of the receive path gains and the fact that these datasets are measured many hours apart. However, further analysis shows that the calibration solutions can be used interchangeably between the datasets and still produce improved images. The grouping of the gain solutions is due to the grouping of the antennas before they are connected to the station cabinet using cables with two or three distinct lengths. A comparison with the gain phases obtained with the Statistically Efficient and Fast Calibration (StEFCal) [30] algorithm is also shown and it is reassuring to see that there is relatively close agreement between the results. A certain degree of the difference in the results of the SH and StEFCal can be explained by a possible difference in the phase referencing of each method. Also note that phase wrapping occurs at some of the antennas. StEFCal is a well established and proven algorithm, making it an excellent reference for these results.

It was previously determined that the level of apparent interference is a major factor that determines the accuracy of the gain estimates. In the dataset where $\theta_{\text{alt}} = 84°$ for Cas A, Cygnus A (Cyg A) is also clearly visible as a strong point source in the imaged visibilities. One would expect it to be a strong source of interference and that it would result in a lower SIR when comparing it to the dataset where $\theta_{\text{alt}} = 46°$ for Cas A, in which Cyg A is below the horizon. The fact that it does not have a lower SIR can be explained by two factors. The power attenuation by the station beam in the direction of Cyg A is approximately -22 dB when the beam is pointed at Cas A, making its contribution much less significant than what it seems in the image. When Cyg A is below the horizon, Cas A also has a much lower altitude angle and as such has a lower apparent brightness due to the attenuation by the EEP's. In this case, the lower apparent brightness of Cas A has a much larger impact on the SIR.

Based on the successful calibration of the LBA station, there is growing confidence that SH may work for the low-frequency aperture array stations of

the SKA as well. This confidence is further increased by successful calibration of two prototype stations using conventional calibration methods using the Sun as single calibration source, i.e., while ignoring all other sources in the sky [68]. This experiment exploits the same underlying assumption of isolation of the signal from a single source for calibration. Since the sun is not always available as a calibration source, some satellite signals are also being considered as artificial calibration sources. Experiments with SH on these prototype stations are being conducted and the first results seem promising [69].

**Results: HBA**

An HBA dataset measured that were measured at 187.7 MHz on 2 October 2011 20:55 UTC was considered. The tile beams were pointed at Cygnus A with $\theta_{\text{alt}} = 60°$. The SIR was estimated as 18.6 dB which corresponds to an RMS gain error of approximately 0.02 according to Figure 4.5. With these gain error statistics, the beamformer efficiency approaches 100% according to (2.39). The higher SIR in comparison with the LBA example can be attributed to the superior isolation of the calibration source by the tile beams and the larger number of elements in the array. Fig. 4.17 shows the calibrated and uncalibrated imaged visibilities of this dataset. There is a clear improvement in the noise across the map, with Cygnus A clearly visible as a point source after calibration. The repetition in the image is due to the sparse spacing of the centre points of the tiles. The centre-to-centre distance is 5.15 m which is 3.1 wavelengths at 187,7 MHz. Fig. 4.18 shows the corresponding gain phase estimates versus iteration number. The estimates converge quickly and there is close agreement with the gain phases obtained with StEFCal. As was the case in the LBA results, a certain degree of the difference in the results of the SH and StEFCal can be explained by a possible difference in the phase referencing of each method. Also, note that phase wrapping occurs at some of the antennas.

### 4.5.2 PAASAR

The concept of PAASAR is to receive medium Earth orbit search and rescue (MEOSAR) signals that are relayed using GPS, Glonass and Galileo satellites. The 406-MHz distress signals from SAR beacons picked up by the satellites are retransmitted to terrestrial receivers at 1545 MHz [70].

The zenith facing segment of the PAASAR icosahedron sphere was considered for simulation. As shown in Figure 4.19, one segment consists of 5 triangles with 10 antennas each.

The GPS satellite positions (altitude and azimuth angles) were acquired from two-line element (TLE)[1] data which can be found online. The period of

[1]https://www.celestrak.com/NORAD/elements/

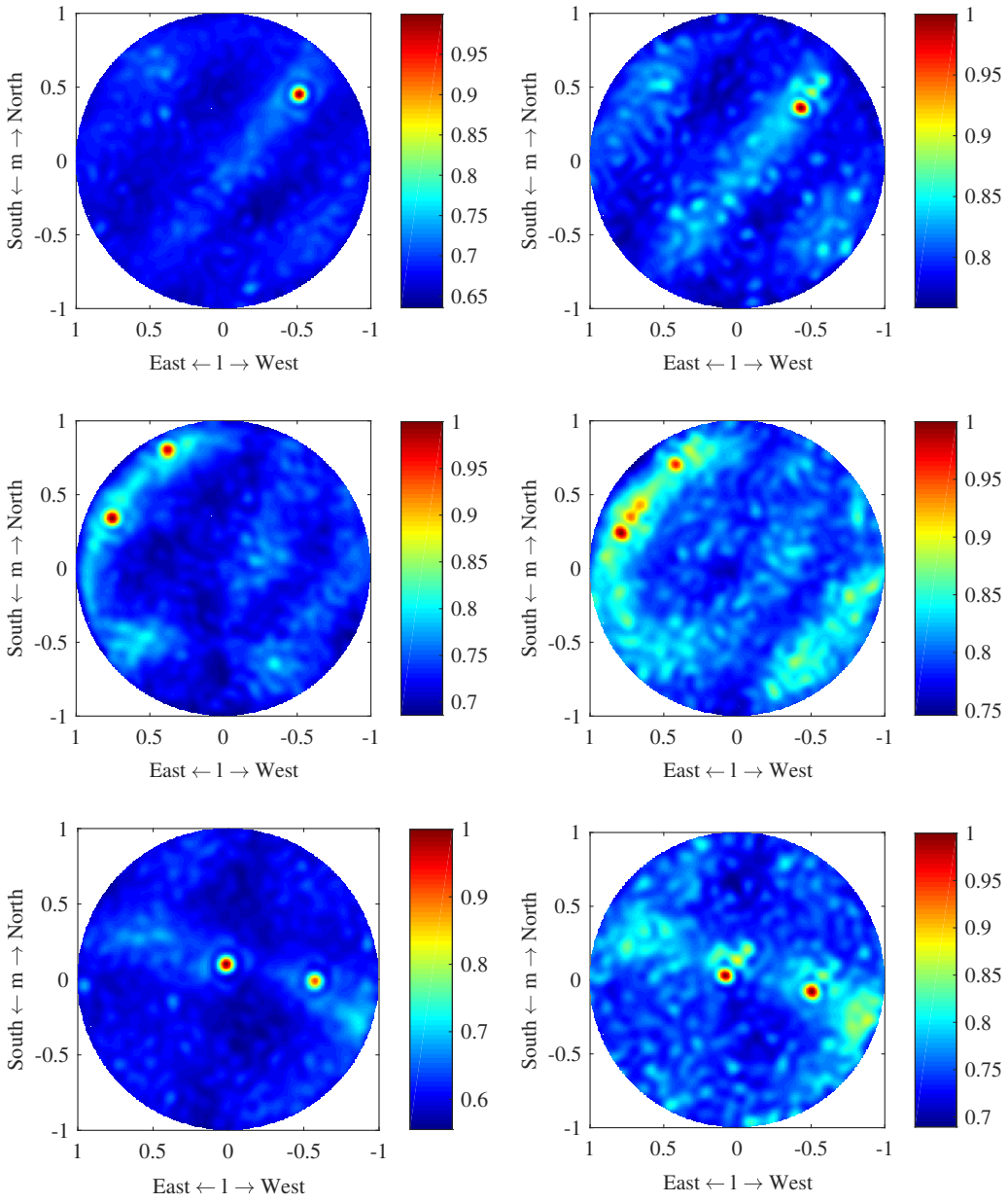


**Figure 4.15:** LOFAR LBA all-sky images at 43.5 MHz for three different times. The images are shown in pairs with calibrated versions on the left and non-calibrated on the right. Starting from top to bottom, the dates are 20 November 2018 at 00:18 ($\theta_{\text{alt}} = 46°$), 10:00 ($\theta_{\text{alt}} = 26°$) and 18:54 ($\theta_{\text{alt}} = 84°$) UTC.

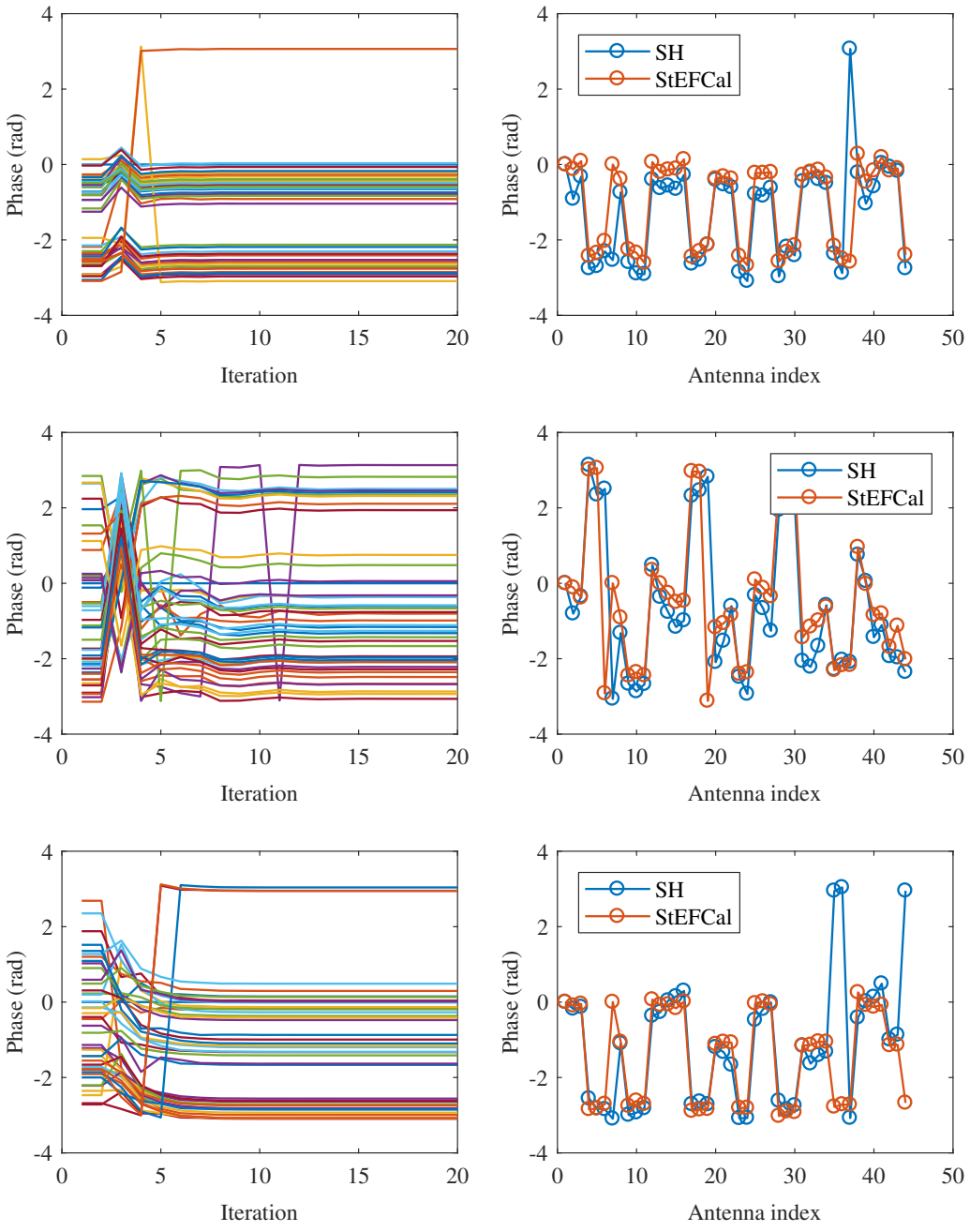


**Figure 4.16:** LOFAR LBA gain phase estimates for the measurements presented in Fig. 4.15 (in the same order from top to bottom). The gain phase estimates versus iteration for all the antennas are shown on the left and a comparison of the final gain phase estimates of SH with those obtained when using StEFCal is shown on the right.

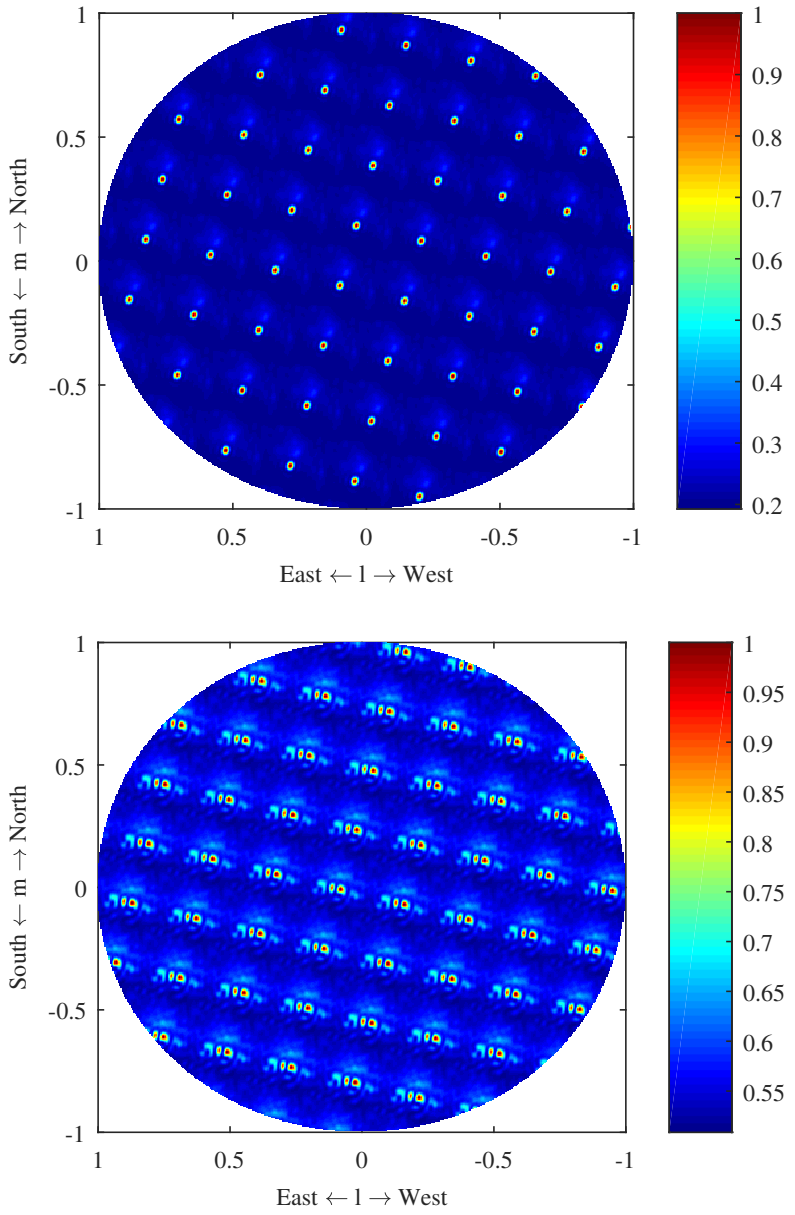


**Figure 4.17:** Calibrated (top) and uncalibrated (bottom) all sky images for a LOFAR HBA measurement on 2 October 2011 20:55 UTC.

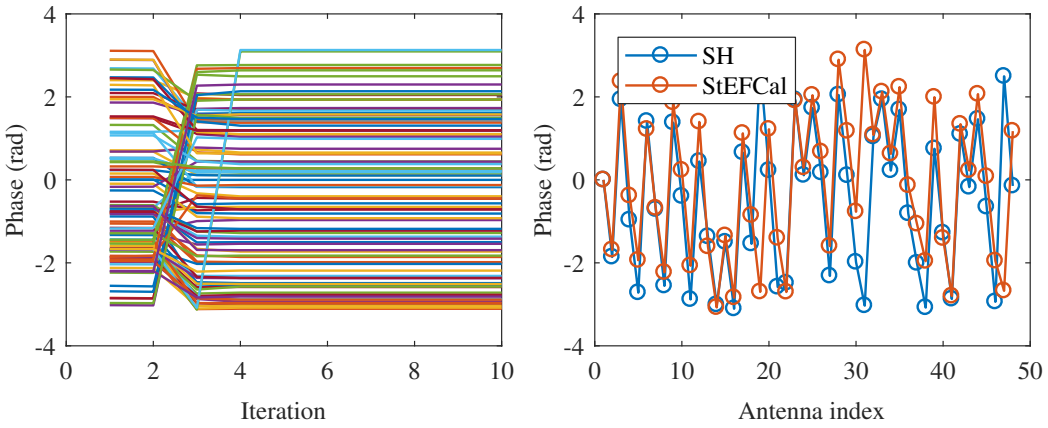


**Figure 4.18:** LOFAR HBA gain phase estimates for the measurements presented in Fig. 4.17. The gain phase estimates versus iteration number for all the antennas are shown on the left and a comparison of the final gain phase estimates of SH with those obtained when using StEFCal is shown on the right.

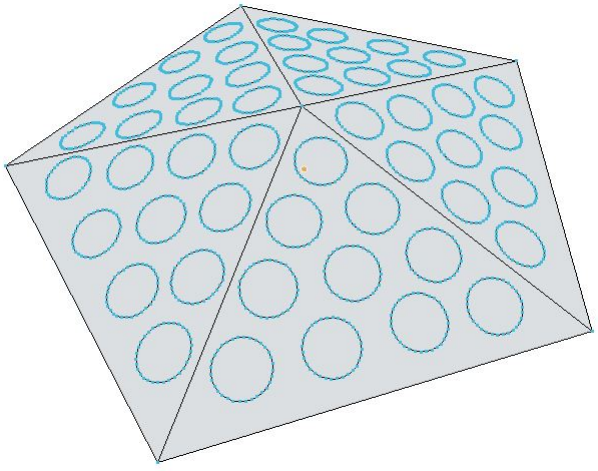

**Figure 4.19:** Perspective view of the PAASAR antenna layout for a single segment of the icosahedron sphere. The antenna positions are indicated by the blue circles.

a GPS satellite is half a sidereal day so to get a comprehensive overview of the SIR statistics, their positions were recorded at 10-minute intervals over 12 hours.

For simulation, it was assumed that all the satellites transmit at the same power level. Their signals were modelled as mutually uncorrelated random noise. The SNR of the output signals at element level is 2 dB [71]. The EEPs of the receiving elements in the array were modelled as a cosine function so that the attenuation in the direction of a certain satellite for a certain receiving element could be calculated as the cosine of the angle between the normal vector of the element, and the unit vector pointing towards the satellite.

Figure 4.20 shows an example of the sky at a random recording. The dots show the positions of the satellites and the colour scale indicates the normalised relative power received from that satellite by the array. Due to the geometry of the array, some satellites will not be visible to all the array elements simultaneously. These satellites are indicated by the empty circles, and as expected, they are mostly located towards the horizon. The SIR, calculated using (4.15), is annotated for each satellite when it is chosen as calibration source. It is interesting to note that some of the weaker sources have a higher SIR compared to that of some of the strong sources. This shows that the SIR also depends on the isolation of the calibration source and not merely on its apparent power. Figure 4.21 shows the maximum SIR at each satellite position recording instance over 12 hours. The maximum SIR varies between 4.5 and 7.5 dB, so it is expected that self-holography will produce converging results with a quality similar to that obtained in the LOFAR LBA example. However, it should be noted that the SIRs will significantly improve if nulling is applied to the strongest interferers. This confirms the conclusions in the original PAASAR calibration study [42]. Also, each GPS satellite transmits a unique pseudo-random binary sequence (PRBS), so, when using the GPS signal itself, the SIR can probably be improved by filtering the output signals of the array elements with the PRBS of the satellite that is being used for calibration.

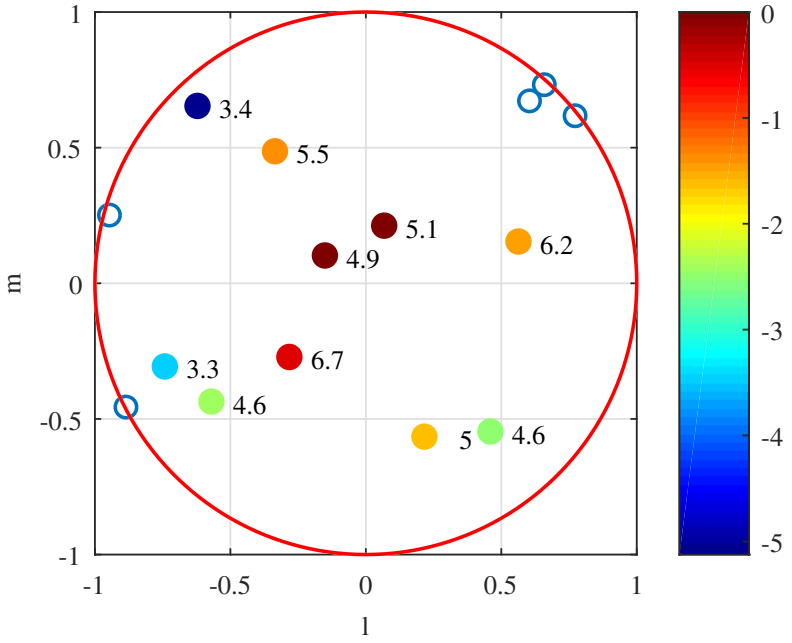


**Figure 4.20:** PAASAR skymap. The dots show the positions of satellites and the colour scale indicates the normalised relative power (dB) received by the array from that source. Empty circles indicate sources that are not visible to all the elements simultaneously. The SIR (dB) of each visible satellite is annotated.

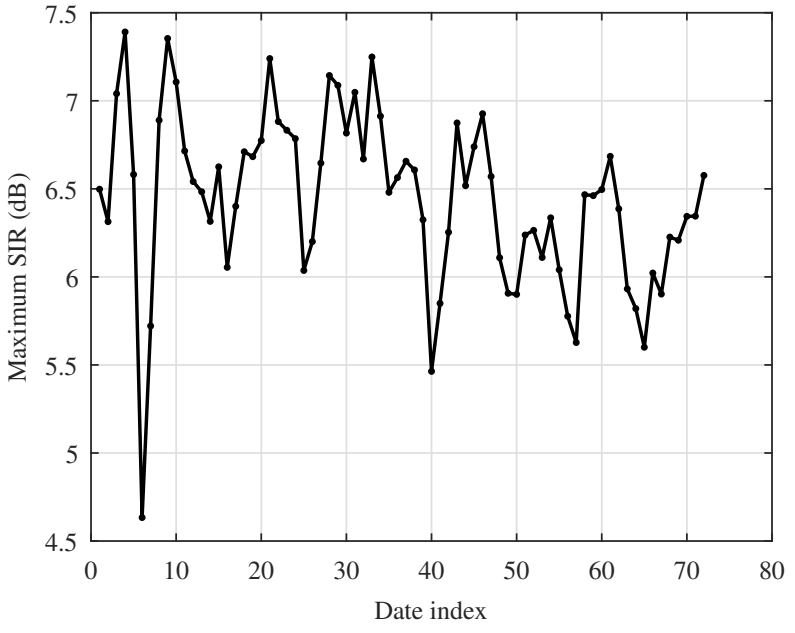


**Figure 4.21:** Maximum SIR of all visible GPS satellites at each 10 minute recording interval over 12 hours.

## 4.6 Conclusion

The simplicity of the SH method stems from the assumption that the calibration signal is free of interference and that the covariance matrix of the system noise is diagonal. This chapter investigated the impact of these assumptions when SH is applied in a non-ideal environment, i.e., a calibration signal containing interference and a noise covariance matrix with non-zero crosscorrelation terms. The impact was first analysed mathematically which resulted in analytical expressions that can be used to predict the performance of SH in a given scenario. These theoretical findings were then further established by simulation. Part of the simulation section included analysis where interference mitigation using null placement was investigated as a possible way of increasing the performance of SH when strong interferers are present. The results showed that null placement can be very effective in maximising the performance of SH under very low SIR conditions. Additionally, it also revealed that SH will switch the main beam to an interferer when its power is high enough.

The chapter concluded by applying SH to three practical examples: A Low-Frequency Array (LOFAR) low-band antenna (LBA) and high-band antenna (HBA) station, and the Phased Array Antenna for Search and Rescue (PAASAR) system. Actual measured data was used for the LOFAR examples which maximise its realism and therefore render its results extra significant. The PAASAR example lacked real measurements, instead, a realistic measurement was simulated from a realistic sky model that was generated using actual positions of GPS satellites. The suitability of applying SH calibration in each example was determined by estimating the SIR for each example. For the LOFAR example, this was done by extracting the relevant signal components from the measured data. The SIR estimates indicated that SH will be able to provide high-quality calibration solutions in all three examples. In the LOFAR example, the quality was confirmed after applying SH calibration to the measured data and noting significant improvements in the all-sky images that were generated from the measurements. Additionally, a close agreement was shown between the gain phase estimates obtained with SH and the gain phase estimates obtained with StEFCal, which is a well studied and proven calibration algorithm.

# Chapter 5

# Calibrating the Mid-Frequency Aperture Array using Self-Holography

## 5.1 Introduction

In this chapter, a detailed analysis is done to assess the calibratability of a Mid-Frequency Aperture Array (MFAA) station [2] using self-holography. This is done by simulating a realistic sky model for an array that is based on the preliminary specifications of the Mid-Frequency Aperture Array Transient and Intensity-Mapping System (MANTIS)[72], which is a planned science demonstrator of the MFAA.

Constructing a realistic sky model from which the SIR can efficiently be calculated using (4.15) is not a simple task. As a result, an extensive analysis is done on multiple resources that can be used to model the sky, to arrive at a modelling methodology that minimises the computational load while upholding an adequate accuracy standard.

The SIR is analysed over 24 hours for a station placed at the SKA site in South Africa. Valuable insights are obtained on more than just the achievable performance of SH.

## 5.2 MANTIS

The Mid-Frequency Aperture Array Transient and Intensity-Mapping System (MANTIS) [72] will be a science demonstrator for the SKA and is planned to be built at the SKA site in South Africa among the existing SKA1-Mid and MeerKAT systems. It will serve as a reference for the science possibilities of a fully populated MFAA system, while also providing insight on costing and technology performance. The MANTIS will integrate well with the existing MeerKAT and SKA1-Mid telescopes. For example, the wide FoV of the

MANTIS will enable the monitoring and detection of transient events that, once detected, can be followed up by observations with the more sensitive MeerKAT and SKA1-Mid telescopes.

The theoretical capabilities of aperture arrays are very attractive for radio astronomy. However, it has been realized that some of these capabilities will be unreachable due to its cost scaling and the limited budgets that are usually associated with astronomy projects. The MANTIS will therefore provide scientists with a testbed from which budget-viable technology can be tested and optimised. The lessons learnt from this experiment will form an integral part of the definition and design of the full MFAA system. Calibration of the MANTIS is a crucial aspect that will have to be studied in detail to ensure that viable scaling can be done to a full MFAA system.

The exact specifications of the MANTIS are not yet finalized. However, the aim is to have a system that closely resembled an MFAA station. Based on this and the planned science cases, the following preliminary specifications seem the most reasonable [72]:

- Frequency range: 450 - 1450 MHz
- Collecting area: 1500 - 2500 $m^2$
- SEFD: 74 - 44 Jy
- FoV: 200 $deg^2$ at 1 GHz
- Bandwidth: >500 MHz
- Transient buffering

These specifications provide enough information to define a realistic receiver system for a calibration study based on SH. The only outstanding aspect required to conduct the study is a realistic sky model. The following sections discuss the steps that were involved in deriving a sky model that is analytically compatible with the SIR definition (4.15), while simultaneously remaining an accurate representation of the true sky.

## 5.3 Modelling the sky

Modelling the sky for MANTIS is not a straightforward task. Keeping the model simple while maximising its accuracy is the first challenge. The Haslam map might seem an obvious choice as a resource for the model since it covers the entire sky. However, modelling the entire sky using the Haslam map will introduce serious computational and complexity issues for an SIR analysis that is based on the MANTIS. Point source catalogues (PSC's) are a logical alternative because they provide a comprehensive overview of the flux distribution

across the sky and are much easier to work with. The Haslam map remains a useful resource and will be used to model certain regions of the sky that cannot be accurately modelled by the PSC's.

To maximise the spectral accuracy of the sky model, it is important that a chosen PSC has an observing frequency that is at least close to the operating band of the MANTIS. This requirement, together with the geographical placement of the MANTIS, introduces a unique challenge for the modelling process. The Sydney University Molonglo Sky Survey (SUMSS) source catalogue compiled using the Molonglo Observatory Synthesis Telescope (MOST) at 843 MHz [73] is the only PSC for the southern hemisphere sky with an appropriate observation frequency. The only drawback is that its coverage is limited to declination angles $\delta < -30°$, which is only around half the sky as seen from the geographical location of MANTIS. Furthermore, Galactic latitudes $-10° < b < 10°$ are unobserved which means that the Galactic plane (GP) is entirely omitted. This coverage issue can partially be solved using the National Radio Astronomy Observatory Very Large Array Sky Survey (NVSS) PSC at 1400 MHz [74] which covers the entire sky north of $\delta = -40°$. Coverage of the GP remains an issue. However, it will be seen that PSC's do not suffice to accurately model the GP anyway and that the Haslam map is far more appropriate.

Combining the two PSC's and the Haslam map requires appropriate conversions and detailed analysis to ensure compatibility and spectral continuity. Before the combination process is discussed, an introduction to each PSC and the Haslam map is provided in which the processes that were followed to compile each is discussed. Understanding these processes specifically for the PSC's is crucial to get an idea of the inter-compatibility of each and the achievable spectral continuity of a sky model compiled from it.

### 5.3.1 The NRAO VLA Sky Survey (NVSS)

The NVSS [74] was conducted using the VLA at 1.4 GHz for the entire sky north of declination $\delta \geq -40°$ which corresponds to approximately 33,810 square degrees ($\Omega \approx 10.3$ sr) of sky area. The observations stretched from 1993 to 1996 with additional observations in 1997 to fill in small gaps that were left by the initial observations. The sky was uniformly covered using a hexagonal grid of pointing centres where each pointing centre had a separation corresponding to the modelled full-width at half-maximum (FWHM) of each VLA antenna, which is 26 arc minutes (0.43°). In total, 217,446 snapshot observations were made where each observation was imaged separately. To maintain near-constant sensitivity at each pointing centre, longer integration times were used at high zenith angles where the system temperature will typically increase due to radiation from the ground. These small images were then combined to form a set of 2,326 $4° \times 4°$ image cubes where the third axis comprised the Stokes polarization parameters I, Q and U.

A special program called VSAD was used to automate the identification of source components in the images. VSAD fits two-dimensional Gaussian distributions to the brightness peaks in each $4^\circ \times 4^\circ$ image. The parameters of each Gaussian are its position in $\alpha$ and $\delta$, peak amplitude in Jy beam$^{-1}$ and FWHM diameter on the major- and minor axis. The fitted Gaussian diameters were constrained to the synthesized beamwidth of the VLA which is 45 arcseconds ($0.0125^\circ$). All the peaks brighter than 1.5 mJy were analysed and fitted with Gaussians but only those with fitted peak brightness >2 mJy beam$^{-1}$ were eventually compiled in the catalogue. The integrated flux densities were calculated after careful consideration was given to the level to which a source is resolved. The reliability of the flux estimates was verified by comparing some of them with the corresponding estimates obtained in the 1412 MHz Westerbork/Einstein surveys [75] conducted with the Westerbork Synthesis Radio Telescope (WSRT). A large fraction of the sources showed a close comparison. The discrepancies were explained to possibly be due to the confusion caused by the larger NVSS synthesized beam in comparison with the smaller WSRT beam and variations in the source parameters (as a function of time). Figure 5.1 shows the positions of sources (in right ascension $\alpha$ and declination $\delta$) with integrated flux $S_{\mathrm{I}} > 1$ Jy from the NVSS and SUMSS PSC's.

### 5.3.2 The Sydney University Molonglo Sky Survey (SUMSS)

The SUMSS [73] was conducted using the Molonglo Observatory Synthesis Telescope (MOST) at 843 MHz for declination angles $\delta \leq -30^\circ$ while excluding galactic latitudes $-10^\circ \leq b \leq 10^\circ$. The end product consists of 590 $4.3^\circ \times 4.3^\circ$ images compiled from individual $2.7^\circ$ diameter observations covering a total of 8100 square degrees (2.5 sr) of the sky. The resolution of these images is $45 \times 45$ cosec$|\delta|$ arcsec$^2$ which is similar to the resolution of the images produced in the NVSS.

Point sources were identified from the images using the same software that was used in the NVSS (VSAD). All the peaks that were brighter than 5 mJy beam$^{-1}$ for $\delta \leq -50^\circ$, and 10 mJy beam$^1$ for $\delta > -50^\circ$ were fitted with Gaussians. The uncertainty in the positions of the fitted sources was found to be a combination of the calibration and fitting uncertainties of the MOST. The positional accuracy of the fitted Gaussians was found to be at least higher than 10 arcsec.

Figure 5.1 shows the positions of sources (in right ascension $\alpha$ and declination $\delta$) with integrated flux $S_{\mathrm{I}} > 1$ Jy from the NVSS and SUMSS PSC's. The sources in the overlapping region of the NVSS and SUMSS ($-40^\circ \leq \delta \leq -30^\circ$) show a median spectral index of -0.83 between 1.4 GHz and 843 MHz.

### 5.3.3 The Haslam map

The Haslam map (HM) is a 408-MHz all-sky continuum survey [76], [77] with an angular resolution of 0.85°. The map was compiled from four separate observations that were all made with the same observing technique: using large parabolic reflector telescopes with identical calibration procedures. The four observations in chronological order are:

- Observations of the Galactic anticentre region made with the Jodrell Bank MkI telescope
- Observations of the northern sky for declinations $-8° \leq \delta \leq 48°$ using the Effelsberg 100-metre telescope.
- Observations of the entire southern sky using the Parkes 64-metre telescope.
- Observations of the north celestial polar region with the Jodrell Bank MkIA telescope.

The all-sky atlas was compiled after applying small correction factors to each survey to ensure near-perfect continuity in the resulting brightness distribution. The derived brightness distribution of each observation was not corrected for the sidelobe response of the individual telescopes involved. The observations made with the higher resolution telescopes were smoothed to the resolution of the lower resolution telescopes using a convolution with a two-dimensional Gaussian function. Figure 5.2 shows the complete atlas in galactic coordinates

### 5.3.4 Compiling the sky model

The flux density and positional uncertainties of the sources in PSC's are expected to have a negligible impact on the accuracy of the SIR calculations in this analysis. It therefore seems reasonable to directly combine the PSC's by only applying an appropriate spectral scaling. Figure 5.3 shows a comparison of the flux densities of a number of common sources, before and after scaling those from the NVSS from 1400 MHz to 843 MHz using the spectral index (0.83) that was derived in [73]. A close agreement is observed which confirms that the scaling is done correctly.

As was discussed earlier, the PSC's alone will not suffice to model a complete and accurate sky. This is because the sky not only consists of point sources, but also diffuse emission as can clearly be seen in Figure 5.2. The diffuse emission will make a relatively small contribution to the visibilities of MANTIS, but it remains a source of interference when performing SH calibration and should therefore be accounted for in the SIR analysis. The only way to account for all the diffuse emission is to use the Haslam map alone

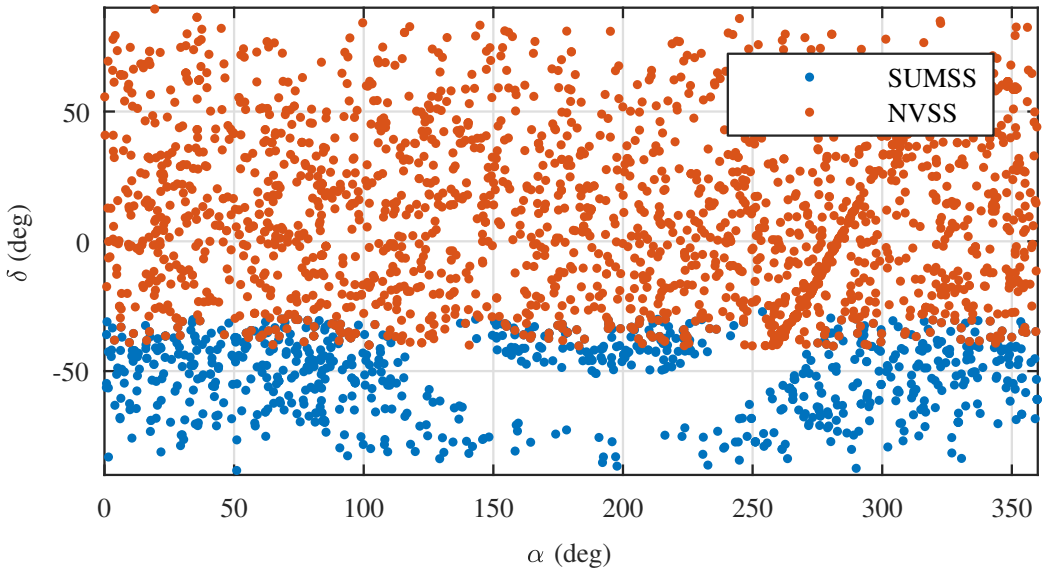


**Figure 5.1:** Point source positions from the NVSS and SUMSS catalogues for $S_{\mathrm{I}} > 1$ Jy

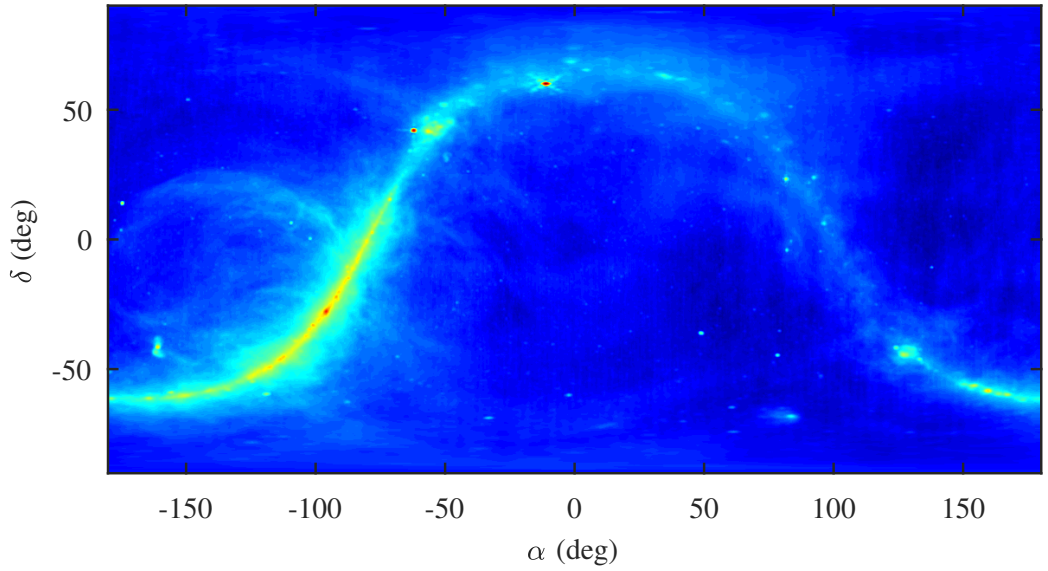


**Figure 5.2:** Haslam 408-MHz all-sky brightness distribution atlas

as resource in the sky model, but it has already been pointed that this will cause a serious computational issue. A quick inspection of Figure 5.2 shows that the highest concentration of diffuse emission is located along the GP. It is therefore suggested that this region of the sky is modelled using the Haslam atlas while the rest of the sky is modelled using the PSC's. In this way, the accuracy is balanced against the computational load.

It is first necessary to apply the appropriate conversions to the HM before it can be added to the sky model. For the analysis in this chapter, the SUMSS observation frequency of 843 MHz is chosen as the operating frequency for the analysis which is conveniently close to the midpoint of the operating band of MANTIS. This also allows more accurate cross checking of certain assumptions in the model.

The Haslam atlas in its native format is a brightness map with Kelvin as brightness unit. A conversion to an intensity map (IM) with units in Jy/sr is therefore necessary before it can be combined with the point source catalogues. This conversion is done using (2.6). Next, a conversion to units of Jy/pixel is done by sampling the IM at a resolution that is related to the spatial resolution of MANTIS. Finally, the flux is scaled to 843 MHz using a spectral index of 0.55. If the conversion of the HM is done correctly (from brightness to intensity and scaling in frequency), it is at least expected that there will be a good flux density comparison with the point sources from the PSC's in regions containing very little to zero diffuse emission. To test this, a collection of bright spots in the HM in isolated regions (far from the GP) were chosen for declinations $\delta < -40^\circ$ so that they can be compared with point sources in the SUMSS catalogue. In this way, only one frequency scaling factor (Haslam from 408 MHz to 843 MHz) has to be taken into account as a factor impacting the accuracy of the comparison. Due to the superior resolution of the SUMSS, each bright spot (an apparent point source) in the IM likely contains several SUMSS point sources. An effort was therefore made to only choose bright spots that are represented by one or two point sources with flux densities that are much higher than the remaining point sources in the bright sport. In this way it can be assumed that the total flux (sum of the pixels) of the bright spot will be dominated by the flux of the strongest point sources it contains. The uncertainty in the source parameters in both the IM and the PSC is inversely proportional to the flux density, which further supports this methodology. The analysis of one of these sources is shown in Figure 5.4 in which close agreement between the total flux of the IM and SUMSS can be seen. Analysis of the remaining bright spots shows similar results which confirms that at least the flux scaling in frequency of the IM is accurate enough. The remaining differences can be attributed to underlying imperfections such as the fitting techniques used in SUMSS and the fact that each pixel in the IM contains a contribution from the flux of the rest of the sky (uncorrected for sidelobe response). A similar analysis for regions in the GP shows a very large flux difference between PSC's and the HM, which is expected given the

large concentration of diffuse emission in that region.

It is therefore concluded that an appropriate sky model can be constructed by using the HM for the GP, i.e., for galactic latitudes $-10° < b < 10°$, and the PSC's for the remaining regions of the sky. In this way the number of sources that needs to be evaluated in the SIR is minimised while an accurate idea of the power distribution across the sky is maintained.

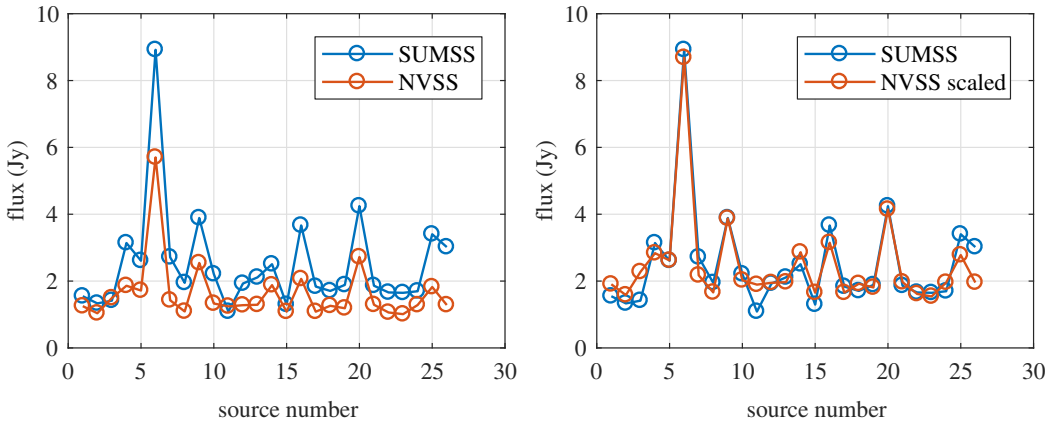


**Figure 5.3:** Fluxes of common point sources in the NVSS and SUMSS catalogues before (left) and (right) after scaling NVSS flux from 1400 MHz to 843 MHz using spectral index $\alpha = 0.83$.

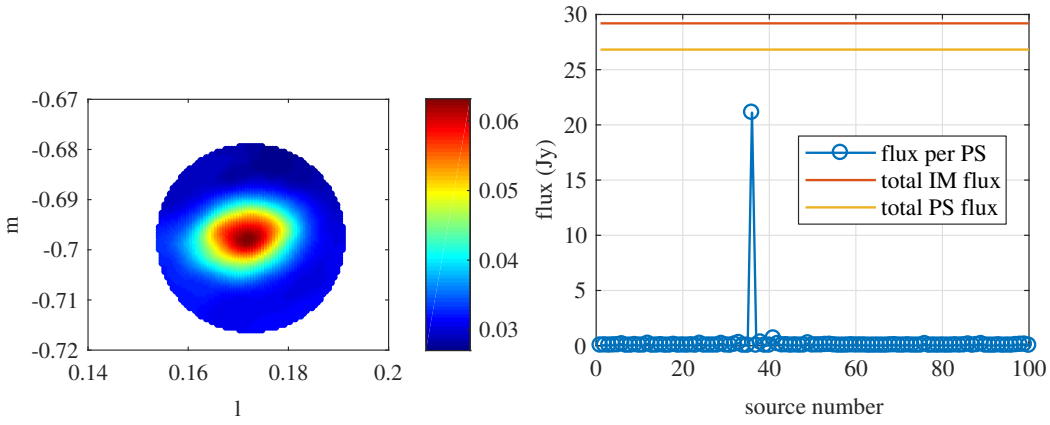


**Figure 5.4:** Left: bright spot in the intensity map (IM) used for analysis. Scale is in Jy/pixel at 843 MHz. Right: flux per SUMSS point source (PS) in the same region. A comparison of the total flux in the IM vs the total PS flux is also shown.

## 5.4 Simulation

### The receiver

The geographic coordinates of the array are 30.72° S and 21.41° E. A square regular array configuration is assumed where the inter-element spacing $d = \lambda/2$ at 1 GHz. To ensure a collecting area of at least 1500 m$^2$ at 1.45 MHz, 336 elements on a side of the array are required when assuming an individual antenna directivity of 4.

The preliminary MANTIS specifications make no direct mention of subdividing the array into tiles. However, it does give a minimum FoV specification of 200 square degrees at 1 GHz. Assuming that the elements on a tile have a regular square layout with a spacing of $\lambda/2$ at 1 GHz, 200 square degrees corresponds to a maximum of 7 elements on a side of a tile ($M$=7). The results in Chapter 5 provided insight on tile sizes of $M$=1, $M$=2 and $M$=4 which is relevant for the analysis in this chapter. By using the same tile sizes in this chapter, the findings and conclusions can be substantiated by directly referring to those results.

The EEP's of the array are assumed to be a sinusoidal function such that the power attenuation in the direction of a source can be calculated as $\sin^2(\theta_{\text{alt}})$ where $\theta_{\text{alt}}$ is the altitude angle of the source.

### Calibrator selection strategy

It was previously determined that the apparent power and isolation are the most important aspects to consider when selecting a calibrator for SH. This was especially true in the PAASAR application example where only a couple of sources with relatively equal apparent power were considered. Using a calibrator that is located in the GP might therefore seem dubious since this is also where sources are the least isolated. However, it was seen in the LOFAR application example that using either Cassiopeia A or Cygnus A (which are both located in the GP) as the calibration source produces excellent calibration results. A LOFAR station is much larger than the PAASAR system which shows that as the directivity of the array increases, the isolation of the calibrator becomes a minor factor in the accuracy of the calibration (assuming the brightest apparent source is chosen). Given the directivity of an array the size of MANTIS, it is therefore reasonable to assume that the most accurate calibration results will be achieved when using the brightest apparent point source in the sky as the calibration source, regardless of its isolation. Unfortunately, with the way the sky is modelled for MANTIS as discussed in Sec. 5.3.4, it will be challenging to select a calibration source from the GP. The available region from which a calibrator can be selected is therefore limited to regions outside the GP where the sky is modelled using the PSC's. This region will further be referred to as the calibration region. The point source

nature of the sky model in the calibration region enables effective automatic identification and evaluation of potential calibrators.

Figure 5.5 (left) shows the cumulative point source count versus lower flux density limit for the calibration region. The exponential nature of the number of point sources versus lower flux limit, together with the fact that the point sources have a uniform random distribution, suggests that it is not unreasonable to assume that the brightest sources are fairly well separated at the resolution of the telescope. It is therefore assumed that the isolation of a bright source (from other bright sources) is not a concerning factor when identifying potential calibrators. A quick visual inspection confirms this assumption. The region from which a calibrator can be selected is further limited to altitude angles $\theta_{\text{alt}} > 30^\circ$ to ensure that the required scan angle of MANTIS to reach a potential calibrator remains realistic in a practical sense.

Due to the superior resolution of the VLA and the MOST, some sources that are resolved in the NVSS and the SUMSS will be unresolved by MANTIS. A good example is Cygnus A, which, at the resolution of the VLA and the MOST, has its two lobes resolved into two separate point sources. At the resolution of MANTIS, Cygnus A will be seen as a single source. Therefore, a potential calibrator in the calibration region will likely be a "cluster" of bright point sources. So when evaluating a potential calibrator, it is a simple matter of determining the flux distribution of that cluster within the main beam of MANTIS to determine an optimal pointing angle for that cluster. For example, the flux distribution might be such that the strongest component is close to the edge of the cluster so when pointing the beam at that component, the rest of the cluster might fall outside the beam. Instead, it is better to point the beam at the cluster component that will ensure that the remaining components of the cluster are inside the beam. A special function is written that receives the positions and corresponding powers of sources stronger than 1 Jy, from which an optimal cluster (and its corresponding pointing angle) is selected based on the apparent power of its brightest component. Obviously, these clusters also contain sources with powers less than 1 Jy, but these are considered to have a negligible contribution to the integrated power of the cluster. The process of calculating the SIR from the sky model is discussed next.

## Calculating the SIR

The SIR is calculated using (4.15), reproduced here for better readability:

$$\text{SIR} = \sigma_{\text{c}}(P-1)\mathbf{1} \oslash \left| \sum_i \sigma_i(\mathbf{a}_i(\mathbf{a}_i^H\mathbf{1}) - \mathbf{1}) \right|. \tag{5.1}$$

For a specific sidereal time, $\mathbf{a}_i$ is the geometric delay vector of each interfering source in the calibration region and each pixel in the GP region ($-10^\circ < b < 10^\circ$). The apparent powers $\sigma_c$ (calibrator) and $\sigma_i$ (interferer) take the

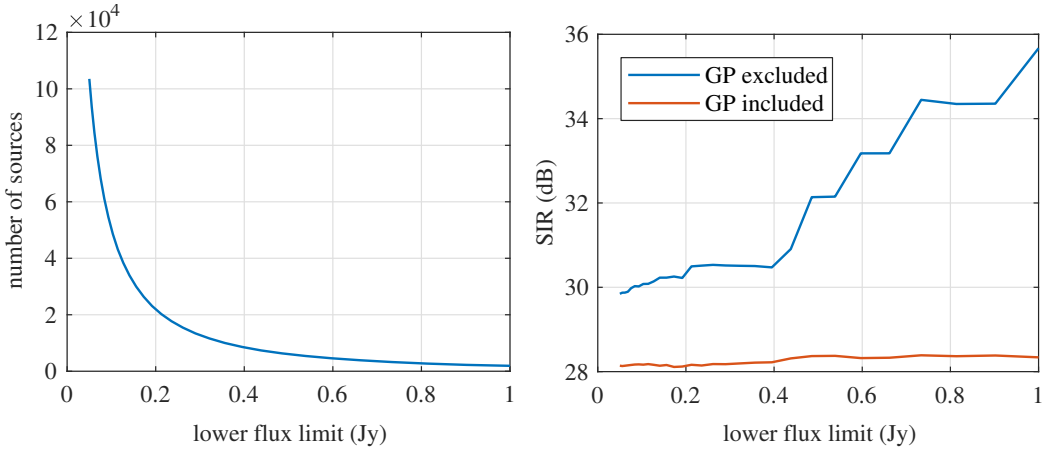


**Figure 5.5:** Cumulative source count (left) and SIR (right) for $M$=1 versus lower flux limit of the sources in the calibration region.

attenuation of both the tile beam (for $M$ >1) and the EEP of each antenna into account. When implementing the sum by looping over all the sources in the sky, the SEFD (after integration) of MANTIS is taken into account by disregarding sources that are below the SEFD. An integration time of 1 second is assumed when calculating the sensitivity of MANTIS. This should be long enough for the integrated signals to approach their expected values, which validates the use of (4.15).

The MANTIS sky model consists of thousands of sources to evaluate. This might become a computational bottleneck when determining the SIR as a function of sidereal time in small increments. By closely examining the source statistics in the calibration region and its effect on the SIR, it is possible to optimise the simulation by limiting the lower flux limit of the sources that are included in the sky model. Figure 5.5 shows the cumulative source count (at a random sidereal time) and the corresponding SIR, as a function of the lower flux limit of the sources in the calibration region. An exponential relationship is observed in the source count while a very weak dependence is observed in the SIR for flux limits < 400 mJy (GP excluded). When including the GP, a very weak dependence is observed for the full lower flux limit range (which highlights the dominance of the interference coming from the GP). A significant optimisation can therefore be done by only regarding point sources with apparent flux densities higher than 400 mJy. In general, the linear (instead of an exponential) dependence of the SIR on the number of sources in the calibration region is largely due to the high directivity of MANTIS.

## Results

The SIR was calculated at 10 minute intervals over 24 hours on 7 November 2020. The results are shown in Figure 5.6. The apparent power of the calibrator $\sigma_c$ at each time instance is plotted on the right axis. The selection of

a calibrator and its apparent power is independent of tile size which is why it can be represented by a single curve.

As expected, the SIR, in general, improves significantly as a function of increasing tile size. This is mostly due to an increase in directivity and a subsequent increase in the isolation of the calibrator. The noisiness of the results can be explained by the movement of bright sources through the sidelobes as time passes. The discontinuities in the calibrator flux over time indicate the instances at which the algorithm selects a new calibrator. A smooth relationship is otherwise noticed in which the attenuation of the EEP is clear.

It is interesting to note that the maximum SIR does not coincide with a the maximum value of $\sigma_c$, which is unexpected based on the earlier assumption that the apparent power of calibrator is the dominant factor in the SIR. A closer look at the flux distribution across the sky can provide some answers. Figure 5.7 shows the positions of all the sources at the indicated times, and their corresponding apparent powers after attenuation by the EEP's and the array beam for $M$=1. Also shown is the corresponding intensity map (Jy/pixel) for the GP with the pointing direction of the array beam indicated by the red cross. The arms of the cross also represent the principal planes of the array.

For $M$=1, the SIR reaches a maximum around midnight when $\sigma_c$ is around half its maximum value over the 24 hours. Several hours later (at t = 09:00), $\sigma_c$ reaches its maximum value while the SIR has decreased slightly. This is explained by the plots in the top two rows in Figure 5.4 which shows the corresponding sky maps at each of these time instances. In both instances, the calibrator is close to the GP and as a result, the array beam samples the GP through its sidelobes in the principal plane with relatively low attenuation. However, at the second instance (t = 09:00), when $\sigma_c$ reaches its maximum, the sidelobes in the principal planes of the array cut through much brighter regions of the GP than in the first instance (t = 00:10), resulting in a much higher level of interference.

A relatively sharp drop in the SIR is noticed around t = 16:00 followed by a sharp rise a short time later. Initially, the SIR decreases as $\sigma_c$ goes down (for t > 09:00) which is an expected trend. However, a few moments later, the SIR increases significantly while $\sigma_c$ remains relatively constant. At t = 15:50 the array beam is pointed at a calibrator close to the horizon with the GP and its centre, where the spatial concentration of power is the highest, close by to the left of the pointing direction. It is visibly clear that the array beam is sampling a significant portion of the GP through its sidelobes with relatively low attenuation due to its close proximity to the main beam. A few moments later at 16:10, the array beam shifts to a new calibrator with similar apparent power but located further away from the GP. The increased distance between this calibrator and the GP results in higher attenuation (by the array beam) of the power coming from it. The result is a sudden increase in the SIR. As expected, the exact increase in SIR at this point is strongly dependent on tile size. As was seen in Chapter 5, for a fixed calibration scenario, an increase

in tile size will always result in a higher SIR due to the higher directivity imposed by the tile beams. After switching to the new calibrator, the SIR continues to increase as a function of time while the apparent power of the calibrator remains relatively constant. This is because the calibrator moves along a contour of the EEP's while the GP moves closer to the horizon resulting in an increase in its attenuation by the EEP's. Eventually, the entire GP dips partially below the horizon, causing the SIR to spike for $M$=2 and $M$=4. This spike is much lower for $M$=1 due to its much lower attenuation at the horizon.

## Discussion

This analysis showed that the isolation of a calibrator from the GP has a much higher impact than initially thought. It was also seen that two calibrators with similar isolation from the GP but significant different power levels can produce counter-intuitive results just because of the specific region of the GP that falls in a principal plane of the array. This shows that, for a regular array layout, care should be taken if a calibrator is selected that is located in the GP. At some instances it is possible that a principal plane aligns exactly with the GP which will probably lead to significant interference levels. These findings suggest that the source with the highest apparent brightness will not always be the optimal calibrator, especially in regions close to the GP.

The calibration strategy and sky model in this analysis is not perfect, but the relevance of the resulting SIR figures remain significant. These SIR figures are expected based on the findings in Chapter 5 where the maximum estimated SIR's in the LOFAR application examples were around 14.6 and 18.6 dB respectively. The much larger size of MANTIS in comparison to a LOFAR station suggests that the achievable SIR for MANTIS should at least be higher than this. In this analysis, the SIR's in almost all instances are above 20 dB which already leads to very accurate calibration results according to Figure 4.5. These results therefore serves as an "at least" guideline to the achievable calibration accuracy when applying SH on MANTIS at frequencies close to 843 MHz.

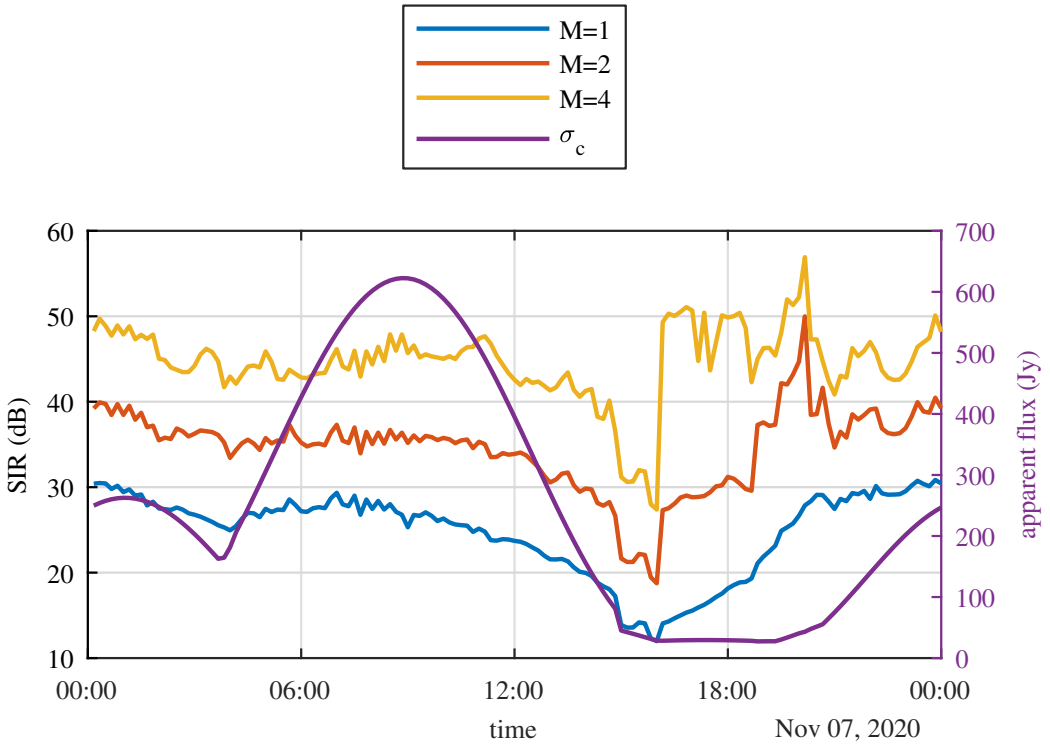


**Figure 5.6:** The SIR at 10 minute intervals over 24 hours on 7 November 2020. The apparent power of the calibrator is shown on the right axis.

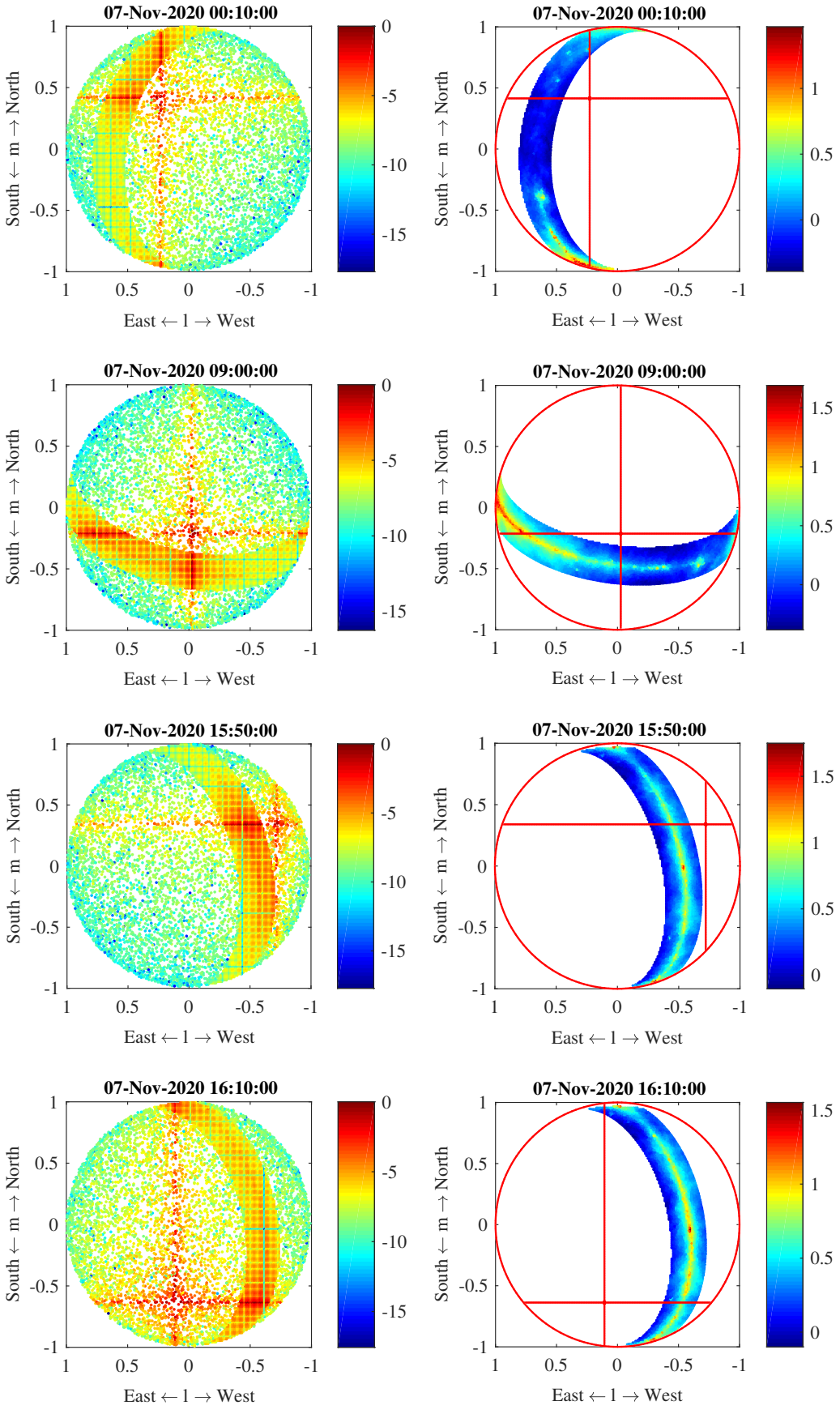


**Figure 5.7:** Left: positions of sources at the indicated times. The logarithmic colour scale indicates their apparent powers after attenuation by EEP's and the array beam. The powers are normalized to the brightest source. Right: the corresponding intensity map (Jy/pixel) for the GP with the pointing direction of the array beam indicated by the red cross. The arms of the cross also represent the principal planes of the array.

## 5.5 Conclusion

This chapter analysed the calibratability of a Mid-Frequency Aperture Array (MFAA) station when using self-holography. To do this, a realistic sky model was simulated for an array that is based on the preliminary specifications of the Mid-Frequency Aperture Array Transient and Intensity Mapping System (MANTIS). Constructing the sky model was not a simple task. Multiple resources were required to construct a model that will have an acceptable computational load when calculating the SIR using (4.15). Extensive analysis was done on each resource to ensure that they are inter-compatible and that a subsequent combination will provide a reasonably accurate version of the sky suitable for the purpose of our analysis.

The SIR was then analysed over 24 hours for a station placed at the SKA site in South Africa. The results revealed that the isolation and position of a potential calibrator close to the GP has a larger impact on the SIR than was previously assumed. For example, the brightest potential calibrator might be located such that a principal plane of the array cuts through a bright region of the GP, resulting in a lower SIR that can otherwise be achieved with a fainter source that is more isolated from the GP. The results showed that SIR's higher than 20 dB are achievable across a full sidereal day. The sub-optimal calibrator selection strategy implies that these results are an "at least" measure of the achievable SIR of MANTIS. It can therefore be concluded, with confidence, that SH will be able to produce high-quality calibration results when applied to the MANTIS. This further implies that a system like an MFAA station can benefit from the low computing requirements of SH compared to full covariance matrix-based calibration methods.

# Chapter 6

# Conclusion and Future Work

Self-holography (SH) was conceived to address some of the computational issues in the calibration of large antenna arrays. The original implementation of self-holography had some drawbacks which ultimately led to a revised implementation. This dissertation presented possible improvements to the original implementation and investigated the performance implications when the assumptions of the revised implementation are violated.

The original implementation of SH directly derives the receive path gains of an antenna array from the correlations between the reference signal and the individual antenna signals. These crosscorrelations contain an unwanted correlation of the thermal noise in the receive paths. This causes a bias in the amplitudes of the gain estimates which will lead to a subsequent decrease in the sensitivity of the array. It was also noted that the amplitudes of the gain estimates oscillate before they converge. It was determined that an accurate compensation of the noise powers in the crosscorrelations can significantly reduce the bias and the oscillation can be reduced by applying an averaging scheme during iteration. It was also determined that an entire elimination of the bias in the amplitudes can never be achieved with this implementation of SH. These issues led to the revised formulation in which the gains and noise powers are estimated simultaneously.

The revised formulation avoids the calculation of the $P^2$ unique entries of the array covariance matrix by assuming that the array only receives the reference signal. This is not an unreasonable assumption to make for large arrays which typically have very high directivities. However, to ensure that SH is suitable for calibrating aperture array instruments, it was necessary to investigate the adverse effects in a scenario where this assumption is violated.

The assumption of an isolated reference signal is violated when interference is present and received through the side lobes of the array. The accuracy of the gain estimates can therefore directly be related to the level of apparent interference received by the array. For a fixed spatial distribution of interferers, the contribution to the total interference by each element is dependent on its position relative to a common reference point. However, it was determined

that these variations were small enough to justify the use of the average of the interference in the crosscorrelations with the reference signal to define an SIR value for the reference signal. The subsequent variations in the gain errors between elements were also small. As such, it seemed possible to accurately relate the gain errors to the signal-to-interference ratio (SIR) of the reference signal. These theoretical findings were then confirmed by a detailed simulation study. In the final step of the simulation study, the gain error was determined as a function of SIR for a given scenario. The relation between the gain error and SIR showed no dependence on the spatial distribution of the interferers or the distribution of the antenna elements which consolidates the use of average values in the SIR. This result is therefore useful to assess the achievable accuracy of SH calibration in an arbitrary scenario.

SH calibration was applied to measured Low-Frequency Array (LOFAR) high-band antenna (HBA) and low-band antenna (LBA) data and a visual inspection of the imaged results indicated that the calibration was applied successfully. The SIR, when using Cassiopeia A as calibration source, was determined by estimating the interference in the dataset. The estimated SIR values were in line with the quality of the imaged results, indicating that the theoretical findings that led to the SIR assessment criterion, are indeed accurate. This was further established by a comparison between the gain estimates obtained with SH and the gain estimates obtained with the Statistically Efficient and Fast Calibration (StEFCal) algorithm, in which close agreement was observed.

With the theoretical findings established, the next step was to analyse the calibratability of a Mid-Frequency Aperture Array (MFAA) station when using SH. Since the MFAA design is not yet finalised, it was decided to use the Mid-Frequency Aperture Array Transient and Intensity-Mapping System (MANTIS) as a reference for the properties of an MFAA station. A realistic sky model was simulated for a station placed at the SKA site in South Africa. Simulating a realistic sky was not trivial - it required a combination of the Sydney University Molonglo Sky Survey (SUMSS) and the NRAO VLA Sky Survey (NVSS) point source catalogues and the Haslam map. A detailed analysis was done on each resource to determine the inter-compatibility of each, and the necessary conversions that should be applied to each to ensure optimal spectral continuity in the resulting sky model. The SIR was then calculated at 10-minute intervals over a sidereal day, where at each 10-minute interval the brightest apparent source outside the Galactic plane was selected as the calibrator. The results showed that SIR's higher than 20 dB can be achieved for most of the sidereal day, which confirms that SH is perfectly suited to calibrate an MFAA station. A detailed analysis of the results also revealed, counter-intuitively, that the brightest apparent source is not necessarily the optimal calibrator when applying SH. It was determined that the isolation of a calibrator from the galactic plane has a significant impact on its SIR.

Although the analysis in this dissertation mostly focused on SH calibration

applied to radio astronomy instruments, it has lots of potential in telecommunication applications as well. In Chapter 4 it was determined that null placement can be very effective in maximising the SIR in scenarios that resemble the typical operating environment of an array in a commercial application. A very brief case study was done on the Phased Array Antenna for Search and Rescue (PAASAR) system, in which it was determined that SH calibration could be applied successfully if the strongest sources in the sky are nulled.

The work done in this thesis is only a start to an ongoing study on SH calibration. The following points have been identified as potential future work that will contribute to an even better understanding of self-holography calibration and its potential:

1. In the mathematical analysis it was assumed that there is zero crosscorrelation or coupling in the noise signals of the array. This assumption requires further analysis since a non-zero coupling in the noise signals is expected to contribute to a bias in the gain estimates.

2. It may be interesting to explore connection between the SIR analysis and the LEAP algorithm, that is based on a similar assumption (although the signal is isolated with a different technique).

3. Exploration of the utility of SH in other application areas, including those with artificial test sources. For example, could SH also be used by an internal test source that is added to the signal without a switch to remove the regular incoming signal.

4. The SIR analyses in the last chapter was limited to 847 MHz. This analysis should be expanded to more frequency points since the properties of the LFAA and MFAA and the sky are strongly dependent on frequency.

# Bibliography

[1] A. van Ardenne, J. D. Bregman, W. A. van Cappellen, G. W. Kant, and J. G. bij de Vaate, "Extending the field of view with phased array techniques: results of european ska research", *Proceedings of the IEEE*, vol. 97, no. 8, pp. 1531–1542, 2009.

[2] P. E. Dewdney, P. J. Hall, R. T. Schilizzi, and T. J. L. W. Lazio, "The Square Kilometre Array", *Proceedings of the IEEE*, vol. 97, no. 8, pp. 1482–1496, Aug. 2009.

[3] P. Hall, R Schillizzi, P Dewdney, and J Lazio, "The square kilometer array (SKA) radio telescope: progress and technical directions", *Radio Science Bulletin*, vol. 236, pp. 4–19, 2008.

[4] J. L. Jonas, "MeerKAT - the South African array with composite dishes and wide-band single pixel feeds", *Proceedings of the IEEE*, vol. 97, no. 8, pp. 1522–1530, 2009.

[5] D. R. DeBoer, A. R. Parsons, J. E. Aguirre, *et al.*, "Hydrogen epoch of reionization array (HERA)", *Publications of the Astronomical Society of the Pacific*, vol. 129, no. 974, p. 045 001, 2017.

[6] S. J. Tingay, R. Goeke, J. D. Bowman, *et al.*, "The murchison widefield array: the square kilometre array precursor at low radio frequencies", *Publications of the Astronomical Society of Australia*, vol. 30, 2013.

[7] C. J. Lonsdale, R. J. Cappallo, M. F. Morales, *et al.*, "The murchison widefield array: design overview", *Proceedings of the IEEE*, vol. 97, no. 8, pp. 1497–1506, 2009.

[8] D. R. DeBoer, R. G. Gough, J. D. Bunton, *et al.*, "Australian SKA pathfinder: a high-dynamic range wide-field of view survey telescope", *Proceedings of the IEEE*, vol. 97, no. 8, pp. 1507–1521, 2009.

[9] G. W. Kant, P. D. Patel, S. J. Wijnholds, M. Ruiter, and E. van der Wal, "EMBRACE: a multi-beam 20,000-element radio astronomical phased array antenna demonstrator", *IEEE Transactions on Antennas and Propagation*, vol. 59, no. 6, pp. 1990–2003, 2011.

[10] Y. Zhang and A. K. Brown, "Octagonal ring antenna for a compact dual-polarized aperture array", *IEEE Transactions on Antennas and Propagation*, vol. 59, no. 10, pp. 3927–3932, 2011.

[11] J. Gilmore, "Design of a dual-polarized dense dipole array for the SKA mid-frequency aperture array", PhD thesis, Stellenbosch University, 2016.

[12] J Abraham, E Colin-Beltran, E de Lera Acedo, and A. Faulkner, "A 16-element LPDA random sparse prototype array for the SKA AA-mid instrument", in *2016 10th European Conference on Antennas and Propagation (EuCAP)*, IEEE, 2016, pp. 1–4.

[13] S. J. Wijnholds, S. van der Tol, R. Nijboer, and A.-J. van der Veen, "Calibration challenges for future radio telescopes", *IEEE Signal Processing Magazine*, vol. 27, no. 1, pp. 30–42, 2009.

[14] J. D. Bregman, "Design concepts for a sky noise limited low frequency array", in *Perspectives on Radio Astronomy: Technologies for Large Antenna Arrays*, 2000, p. 23.

[15] M. de Vos, A. W. Gunst, and R. Nijboer, "The LOFAR telescope: system architecture and signal processing", *Proceedings of the IEEE*, vol. 97, no. 8, pp. 1431–1437, 2009.

[16] M. P. van Haarlem, M. W. Wise, A. Gunst, *et al.*, "LOFAR: the low-frequency array", *Astronomy & astrophysics*, vol. 556, A2, 2013.

[17] A Van Ardenne, P. N. Wilkinson, P. D. Patel, and J. G. bij de Vaate, "Electronic multi-beam radio astronomy concept: EMBRACE a demonstrator for the European SKA program", *Experimental Astronomy*, vol. 17, no. 1-3, pp. 65–77, 2004.

[18] P. D. Patel, G. W. Kant, E van de Wal, and A. van Ardenne, "Towards completion of aperture array developments–EMBRACE update", *URSI General Assembly, Chicago*, 2008.

[19] J. W. Baars, J. F. van der Brugge, J. L. Casse, J. Hamaker, L. Sondaar, J. Visser, and K. J. Wellington, "The synthesis radio telescope at Westerbork", *Proceedings of the IEEE*, vol. 61, no. 9, pp. 1258–1266, 1973.

[20] A. R. Thompson, B. Clark, C. Wade, and P. J. Napier, "The very large array", *The Astrophysical Journal Supplement Series*, vol. 44, pp. 151–167, 1980.

[21] C Lonsdale, "Calibration approaches", *MIT Haystack, Tech. Rep. LFD memo 015*, 2004.

[22] F. R. Schwab, "Adaptive calibration of radio interferometer data", in *1980 Intl Optical Computing Conf I*, International Society for Optics and Photonics, vol. 231, 1980, pp. 18–25.

[23] T. Cornwell and P. Wilkinson, "A new method for making maps with unstable radio interferometers", *Monthly Notices of the Royal Astronomical Society*,

[24] T. Pearson and A. Readhead, "Image formation by self-calibration in radio astronomy", *Annual Review of Astronomy and Astrophysics*, vol. 22, no. 1, pp. 97–130, 1984.

[25] T. Cornwell, "The applications of closure phase to astronomical imaging", *Science*, vol. 245, no. 4915, pp. 263–269, 1989.

[26] J. Hamaker and J. Bregman, "Understanding radio polarimetry. iii. interpreting the iau/ieee definitions of the stokes parameters", *Astronomy and Astrophysics Supplement Series*, vol. 117, no. 1, pp. 161–165, 1996.

[27] O. M. Smirnov, "Revisiting the radio interferometer measurement equation-i. a full-sky jones formalism", *Astronomy & Astrophysics*, vol. 527, A106, 2011.

[28] ——, "Revisiting the radio interferometer measurement equation-ii. calibration and direction-dependent effects", *Astronomy & Astrophysics*, vol. 527, A107, 2011.

[29] ——, "Revisiting the radio interferometer measurement equation-iii. addressing direction-dependent effects in 21 cm wsrt observations of 3c 147", *Astronomy & Astrophysics*, vol. 527, A108, 2011.

[30] S. Salvini and S. J. Wijnholds, "StEFCal - an alternating direction implicit method for fast full polarization array calibration", in *2014 XXXIth URSI General Assembly and Scientific Symposium (URSI GASS)*, IEEE, 2014, pp. 1–4.

[31] S. Salvini and S. J. Wijnholds, "Fast gain calibration in radio astronomy using alternating direction implicit methods: Analysis and applications", *Astronomy & Astrophysics*, vol. 571, no. A97, pp. 1–14, Nov. 2014.

[32] J. E. Noordam and O. M. Smirnov, "The meqtrees software system and its use for third-generation calibration of radio interferometers", *Astronomy & Astrophysics*, vol. 524, A61, 2010.

[33] M. Pesavento, A. B. Gershman, and K. M. Wong, "Direction finding in partly calibrated sensor arrays composed of multiple subarrays", *IEEE Transactions on Signal Processing*, vol. 50, no. 9, pp. 2103–2115, 2002.

[34] C. M. S. See and A. B. Gershman, "Direction-of-arrival estimation in partly calibrated subarray-based sensor arrays", *IEEE Transactions on Signal Processing*, vol. 52, no. 2, pp. 329–338, 2004.

[35] S. van der Tol, B. D. Jeffs, and A.-J. van der Veen, "Self-calibration for the LOFAR radio astronomical array", *IEEE Transactions on Signal Processing*, vol. 55, no. 9, pp. 4497–4510, 2007.

[36] B. P. Flanagan and K. L. Bell, "Array self-calibration with large sensor position errors", *Signal Processing*, vol. 81, no. 10, pp. 2201–2214, 2001.

[37] C. See, "Method for array calibration in high-resolution sensor array processing", *IEEE Proceedings-Radar, Sonar and Navigation*, vol. 142, no. 3, pp. 90–96, 1995.

[38] A. J. Weiss and B. Friedlander, "Array shape calibration using sources in unknown locations-a maximum likelihood approach", *IEEE Transactions on Acoustics, Speech, and Signal Processing*, vol. 37, no. 12, pp. 1958–1966, 1989.

[39] B. Peeters, "PAASAR: Phased Array Antenna for Search and Rescue - Design and Analysis Document", ESA, Tech. Rep. UMR-ESA-PAASAR-DD-001-v2.3, 2016.

[40] A. P. Beardsley, N. Thyagarajan, J. D. Bowman, and M. F. Morales, "An efficient feedback calibration algorithm for direct imaging radio telescopes", *Monthly Notices of the Royal Astronomical Society*, vol. 470, no. 4, pp. 4720–4731, Oct. 2017.

[41] N. Thyagarajan, A. P. Beardsley, J. D. Bowman, and M. F. Morales, "A generic and efficient e-field parallel imaging correlator for next-generation radio telescopes", *Monthly Notices of the Royal Astronomical Society*, vol. 467, no. 1, pp. 715–730, 2017.

[42] J. A. Kegel, G. W. Kant, and S. J. Wijnholds, "PAASAR: Phased Array Antenna for Search and Rescue - PAASAR Phased Array Calibration", ESA, Tech. Rep. AST-ESA-PAASAR-TN-002_v1.2, 2014.

[43] S. J. Wijnholds, "Calibration of mid-frequency aperture array stations using self-holography", in *2017 International Conference on Electromagnetics in Advanced Applications (ICEAA)*, Sep. 2017, pp. 967–970.

[44] C. R. Wilke, S. J. Wijnholds, and J. Gilmore, "Performance improvement of self-holography based aperture array station calibration", in *2019 13th European Conference on Antennas and Propagation (EuCAP)*, 2019, pp. 1–5.

[45] C. R. Wilke, S. J. Wijnholds, and J. Gilmore, "Self-holography – slimming down calibration of large aperture arrays", in *2020 XXXIIIrd General Assembly and Scientific Symposium of the International Union of Radio Science*, 2020, pp. 1–4.

[46] A. Ludwig, "The definition of cross polarization", *IEEE Transactions on Antennas and Propagation*, vol. 21, no. 1, pp. 116–119, 1973.

[47] M Zatman, "How narrow is narrowband?", *IEEE Proceedings-Radar, Sonar and Navigation*, vol. 145, no. 2, pp. 85–91, 1998.

[48] A. Bennett, "The revised 3C catalogue of radio sources.", *MNRAS*, vol. 68, p. 163, 1962.

[49] A. R. Thompson, J. M. Moran, and G. W. Swenson, *Interferometry and Synthesis in Radio Astronomy*. Springer International Publishing, 2017.

[50] C. A. Balanis, *Antenna Theory*, Second. John Wiley & Sons, 1997.

[51] K. F. Warnick, B. Woestenburg, L. Belostotski, and P. Russer, "Minimizing the noise penalty due to mutual coupling for a receiving array", *IEEE Transactions on Antennas and Propagation*, vol. 57, no. 6, pp. 1634–1644, 2009.

[52] M. Viberg, B. Ottersten, and T. Kailath, "Detection and estimation in sensor arrays using weighted subspace fitting", *IEEE Transactions on Signal Processing*, vol. 39, no. 11, pp. 2436–2449, 1991.

[53] R. Schmidt, "Multiple emitter location and signal parameter estimation", *IEEE Transactions on Antennas and Propagation*, vol. 34, no. 3, pp. 276–280, 1986.

[54] A.-J. Boonstra, "Radio Frequency Interference Mitigation in Radio Astronomy", PhD thesis, 2005.

[55] A. Quinlan, J.-P. Barbot, and P. Larzabal, "Automatic determination of the number of targets present when using the time reversal operator", *The Journal of the Acoustical Society of America*, vol. 119, no. 4, pp. 2220–2225, 2006.

[56] S. J. Wijnholds, "Embedded element patterns in hierarchical calibration of large distributed arrays", in *XXXIV General Assembly and Scientific Symposium (GASS) of the International Union of Radio Science (URSI)*, Aug. 2020.

[57] S. J. Wijnholds, J. D. Bregman, and A. J. Boonstra, "Sky noise limited snapshot imaging in the presence of rfi with lofars initial test station", *Experimental Astronomy*, vol. 17, no. 1-3, pp. 35–42, 2004.

[58] B. A. Munk, *Frequency Selective Surfaces*. Hoboken, NJ, USA: John Wiley & Sons, Inc., 2000.

[59] S. van der Tol and A.-J. van der Veen, "Application of robust capon beamforming to radio astronomical imaging", in *Proceedings.(ICASSP'05). IEEE International Conference on Acoustics, Speech, and Signal Processing, 2005.*, IEEE, vol. 4, 2005, pp. iv–1089.

[60] ——, "Performance analysis of spatial filtering of RF interference in radio astronomy", *IEEE Transactions on Signal Processing*, vol. 53, no. 3, pp. 896–910, 2005.

[61] C. R. Wilke, S. J. Wijnholds, and J. Gilmore, "Calibratability of aperture arrays using self-holography", *IEEE Transactions on Antennas and Propagation*, 2021.

[62] J. D. Bregman, "System design and wide-field imaging aspects of synthesis arrays with phased array stations", PhD thesis, 2012.

[63] R. Jongerius, S. J. Wijnholds, R. Nijboer, and H. Corporaal, "An end-to-end computing model for the square kilometre array", *Computer*, vol. 47, no. 9, pp. 48–54, 2014.

[64] J. P. Weem and Z. Popovic, "A method for determining noise coupling in a phased array antenna", in *2001 IEEE MTT-S International Microwave Sympsoium Digest*, vol. 1, Phoenix, AZ (USA), 2001, pp. 271–274.

[65] M. V. Ivashina, R. Maaskant, and B. Woestenburg, "Equivalent system representation to model the beam sensitivity of receiving antenna arrays", *IEEE Antennas and Wireless Propagation Letters*, vol. 7, pp. 733–737, 2008.

[66] S. J. Wijnholds, M. Arts, P. Bolli, P. Di Ninni, and G. Virone, "Using embedded element patterns to improve aperture array calibration", in *2019 International Conference on Electromagnetics in Advanced Applications (ICEAA)*, Sep. 2019.

[67] S. Kulkarni, "Self-noise in interferometers: radio and infrared", *Astronomical Journal*, vol. 98, no. 3, pp. 1112–1130, Sep. 1989.

[68] M. Waterson *et al.*, "Report on the station calibration task", SKA Organization, Tech. Rep. SKA-TEL-SKO-0001088, 2019.

[69] D. Davidson, personal communication, Jan. 1, 2019.

[70] B. Peeters, "PAASAR: Phased Array Antenna for Search and Rescue - Annex A to Design and Analysis Document", ESA, Tech. Rep. UMR-ESA-PAASAR-DD-001-v1.2, 2016.

[71] J. A. Kegel, "PAASAR Radio Link Budget", ESA, Tech. Rep. AST-ESA-PAASAR-TN-001_v1.2, 2013.

[72] W. A. van Cappellen *et al.*, *MANTIS: The Mid-Frequency Aperture Array Transient and Intensity-Mapping System*, https://arxiv.org/abs/1612.07917, MANTIS white paper, Dec. 2016.

[73] T. Mauch, T. Murphy, H. J. Buttery, J. Curran, R. W. Hunstead, B. Piestrzynski, J. G. Robertson, and E. M Sadler, "SUMSS: a wide-field radio imaging survey of the southern sky", *MNRAS*, vol. 342, p. 1117, 2003.

[74] J. J. Condon, W. D. Cotton, E. W. Greisen, Q. F. Yin, R. A. Perley, T. G. B., and J. J. Broderick, "NRAO VLA Sky Survey (NVSS)", *The Astronomical Journal*, vol. 115, 1998.

[75] R. Windhorst, G. Van Heerde, and P Katgert, "A deep westerbork survey of areas with multicolor mayall 4 m plates. i-the 1412-MHz catalogue, source counts and angular size statistics", *Astronomy and Astrophysics Supplement Series*, vol. 58, pp. 1–37, 1984.

[76] C. Haslam, U Klein, C. Salter, H Stoffel, W. Wilson, M. Cleary, D. Cooke, and P Thomasson, "A 408-MHz all-sky continuum survey. I-Observations at southern declinations and for the North Polar region", *Astronomy and Astrophysics*, vol. 100, pp. 209–219, 1981.

[77] C. Haslam, C. Salter, H Stoffel, and W. Wilson, "A 408-MHz all-sky continuum survey. II-The atlas of contour maps", *Astronomy and Astrophysics Supplement Series*, vol. 47, p. 1, 1982.